

SURFACE SCIENCE STUDIES ON TITANIA FOR SOLAR FUEL APPLICATIONS

Courtney Sara Mathews Hadsell

A dissertation submitted to the faculty of the University of North Carolina at Chapel Hill
in partial fulfillment of the requirements for the degree of Doctor of Philosophy in the
Department of Physics and Astronomy.

Chapel Hill

2013

Approved by:

Dr. Yue Wu

Dr. Christopher Clemens

Dr. Rene Lopez

Dr. Thomas Meyer

Dr. Edward T. Samulski

© 2013

Courtney Sara Mathews Hadsell

ALL RIGHTS RESERVED

ABSTRACT

**COURTNEY SARA MATHEWS HADSELL: Surface Science Studies on Titania for
Solar Fuel Applications
(Under the direction of Prof. Yue Wu)**

Titanium dioxide (titania) is a well-studied material for various applications including but not limited to, paint, sunscreen, pharmaceuticals and solar cell applications (photocatalysis.) It can be found in three main crystal forms; rutile, anatase, and brookite and this work will focus on the anatase form which has been heavily studied for its potential in dye sensitized solar cells (DSSCs.) I propose that aqueous and photo dye stability can be improved by taking special care to the exposed surface of anatase. Additionally, the theoretical maximum open circuit voltage of a DSSC is dependent upon which surface is exposed to the electrolyte. Previous works in this area have not been rigorous with respect to the surface and morphology of titania being used. Standard synthesis techniques of anatase lead to a crystal that generally has 94% of the titania (101) surface exposed, and the other 6% is the higher energy (001) surface. The (101) surface has 5 & 6-fold coordinated titania whereas the (001) surface only has 5-fold (under) coordinated titania. This under-coordination leads to enhanced reactivity of the (001) surface which has been demonstrated by dissociative adsorption of water, and catalysis applications. Much theoretical work has focused on the minority (001) surface because up until recently synthesizing anatase with enhanced exposure of the (001) surface has been difficult. The initial materials for this study will be multilayer titania

nanotubes (TiNTs) and nanosheets (TiNS) which have been previously characterized by my predecessor. The TiNTs and TiNS have 100% exposed (001)-like surface. Both of these materials show enhanced stability of phosphonated dye binding as compared to the current standard of anatase nanoparticles (NPs) however, due to their limited thermal stability the potential of incorporating the TiNTs and TiNSs into devices has been eliminated in this study. To overcome the device limitations I will synthesis a novel titania nanotile (ntile) material which will have enhancement of the (001) surface while an increased thermal stability allowing for incorporation into a device. These ntiles will be created from a hydrothermal hydrolysis reaction between titanium n-butoxide (TiBuOx) and hydrofluoric acid (HF.) I will characterize this novel material and demonstrate the enhanced dye binding as well as the device capabilities.

**TO MY FRIENDS, FAMILY AND EVERYONE THAT HAS HELPED ME
ALONG THE WAY.**

ACKNOWLEDGEMENTS

Since I do not trust my memory to specify everyone that has supported me through this process I would like to start out with a general acknowledge of the support of everyone that helped me throughout my educational career. Their intellectual and emotional support has been invaluable in my ability to accomplish my goals.

The opportunity to have non service based funding throughout graduate school was invaluable in allowing me to complete my project with as few interruptions as possible and thus would like to thank the following funding sources at various points during graduate school; The UNC Board of Governors Fellowship, the GAANN fellowship and the UNC EFRC.

During the scientific process I have had the opportunity to collaborate and work with many spectacular people that have facilitated various aspects of my project and offered valuable insight and discussions throughout the process. I would like to thank my advisor, Yue Wu and the members of the Wu group that I've had the pleasure to work with throughout my project. I will start out with Greg Mogilevsky who was an excellent mentor and colleague to help get me started and through continued support after his graduation. Additionally, I would like to thank Alfred Kleinhammes, Jacob Forstater, and Zhixiang Luo for their help with the NMR studies in my dissertation and the valuable insight and discussions that they offered with my project. I would also like to thank my colleagues and collaborators in the UNC chemistry department who have been a useful

sounding board and experimental consultants. These people are Kyle Brennaman, and Ken Hanson your valuable insight and feedback have served to make me a better researcher.

Much of the data presented in this dissertation would not have been possible without access to CHANL's equipment (TEM, SEM, XPS, & XRD) and people. That being said I would like to thank CHANL for their equipment and the following people who have helped train me and troubleshoot any issues that arose; Carrie Donley, Peter White and Amar Kumbhar.

Throughout graduate school I have been fortunate to meet several people that I now consider some of my closest friends and the support that they have offered has kept me going and made the experience much more pleasurable. I would like to thank Lori Downen and David Eby for providing both sounding board and distractions whenever needed. I would also like to thank Laurel Burk who has been there for me from when we met during prospective weekend through the entirety of graduate school. She has been an endless source of support on the bad days when it seemed like nothing was going to work, and a cohort in celebration on the good days. I have greatly cherished her friendship and understanding. Additionally I would like to thank my husband, Michael Hadsell for everything that he has done to help facilitate my trek through this degree. His endless support and motivation allowed me to keep going and I don't believe I could have picked a better partner to share this with. And though we've known each other for much longer than I've been in graduate school I would like to thank David Do for friendship, support, and thoughtfulness that he has displayed since I've known him and consider him to be a part of my extended family.

Lastly, I would like to thank my family for the support that they have offered me throughout my life that has made it so I was able to complete my education with as little outside worry as possible.

To anyone that I might have forgotten, thank you!

TABLE OF CONTENTS

LIST OF TABLES	xiii
LIST OF FIGURES	xiv
LIST OF ABBREVIATIONS.....	xx
CHAPTER 1 INTRODUCTION	1
1.1 Titania	2
1.1.1 Rutile.....	2
1.1.2 Anatase.....	3
1.1.3 General surface chemistry of anatase	5
1.1.4 Anatase the (101) and (001) surface	6
1.1.4a The (101) surface	6
1.1.4b The (001) surface	7
1.1.5 Dissertation Outline	10
1.1.6 Solar Technologies	11
1.1.7 Dye Sensitized Solar Cells & Dye Sensitized Photoelectrosynthetic Cells.....	12
CHAPTER 2 TITANIA SYNTHESIS AND CHARACTERIZATION	18
2.1 Commercially Available Titania Morphologies	18
2.2 Novel Synthesized Titania Morphologies Synthesis and Characterization	19
2.2.1 Multilayered delaminated anatase nanotubes	20
2.2.2 Shortened nanotubes and nanosheets.....	21

2.2.3 (001) Enhanced Titania Nanotiles	24
2.2.4 Fluorine and the (001) surface	36
2.2.5 Nanotile synthesis anomalies and variations	37
2.2.6 Structural comparison and summation of TiNTs, sTiNTs, TiNS, Ntiles and conventional anatase morphologies	39
CHAPTER 3 BAND STRUCTURE OF TITANIA NANOMATERIALS	42
3.1 Band gap tuning via nitrogen doping	44
3.1.1 Nitrogen doped TiNTs	44
3.2 Spectroelectrochemical Band Edge Determination	49
3.3 Band Gap Measurements of Nanomaterial Titania.....	55
3.4 Trap State Analysis of (001) Enhanced Nanotiles	57
CHAPTER 4 DYE SENSITIZED SOLAR CELL DEVICE DEVELOPMENT AND ELECTRICAL CHARACTERIZATION	60
4.1 Film Preparation of Nanomaterial Anatase.....	60
4.1.1 Nanotube and Nanosheet Film Preparation	61
4.1.2 Nanotile Film Preparation.....	63
4.2 Film and device considerations and constituents.....	67
4.2.1 Dyes	67
4.2.2 Device Design.....	68
4.3 Film Characterization Transient Absorbance and Dye Loading.....	69
4.3.1 Nanosecond Transient Absorbance Experimental and Equipment Specifications	69

4.3.2 Nanosecond Transient Absorbance Measurements: Injection efficiency & Back Electron Transfer Rates.	70
4.4 Device Characterization: I-V, IPCE and Impedance Spectroscopy.....	75
4.4.1 IPCE, I-V and Impedance Spectroscopy Experimental and Equipment Specifications	75
4.4.2 IPCE and I-V Device Characterization.....	76
4.4.3 Electrochemical Impedance Spectroscopy Measurements on Ntile films.	86
CHAPTER 5: DYE LOADING, BINDING MECHANISM, AND STABILITY	89
5.1 Dye Adsorption and Stability Discussion	89
5.2 Dye Surface Coverage of (101) and (001) surface	91
5.2.1 Dye Loading Conditions.....	92
5.2.2 Dye surface coverage comparison	92
5.3 Dye Stability	94
5.3.1 Experimental Methods.....	94
5.3.2 Aqueous Dye Stability Results	95
5.3.3 Photo-Stability of Dye Results	97
5.4 Dye Binding Mechanism	99
5.4.1 Attenuated Total Reflectance-Infrared Spectroscopy.....	101
5.4.2 Attenuated Total Reflectance-Infrared Spectroscopy Results	102
5.4.3 Introduction to Nuclear Magnetic Resonance Theory	105
5.4.4 Experimental Methods.....	106
5.3.5 TGA Analysis of Ntiles	107
5.3.6 ^1H MAS NMR Results.....	108

5.3.7 ^{31}P MAS NMR Results	109
5.4.8 Dye Binding Mechanism Results	111
5.5 Conclusions.....	113
5.6 Future Work and Project Direction.....	114
CHAPTER 6 SCIENTIFIC OUTREACH AND CLEAN ENERGY LABS	116
6.1 Background information	116
6.2 Lab Procedure and Development.....	117
6.2.1 Nanomaterial Synthesis	117
6.2.2 Paste and Film Preparation	120
6.2.3 Dye Choice and Preparation	122
6.2.4 Device Assembly	123
6.2.5 Testing and Results	125
6.2.6 Cautions and Hazards	127
REFERENCES:	128

LIST OF TABLES

Table 1: Relaxed surface formation energies for anatase titania ¹¹	4
Table 2: Synthesis conditions and corresponding nanotile sizes	26
Table 3: Atomic concentrations calculated from XPS spectra for ntile samples after washing and subsequent anneals. Fluorine concentration is highlighted in red.	36
Table 4: Tri-Exponential fit parameters for ns transience absorbance of ntile and standard NP films derivatized with RuP	73
Table 5: Voc, Jsc, and FF from I-V curve analysis of sTiNT and TiNS devices.	77
Table 6: I-V characterization data for doctor-bladed (DB) films and spin coated films ..	86
Table 7: Desorption rates of RuP dye under illumination	99
Table 8: ³¹ P NMR Peak Fitting Results for PPA derivatized NP anatase and NTiles....	111

LIST OF FIGURES

Figure 1: Rutile unit cell with titanium atoms (gray) and oxygen atoms (red).....	3
Figure 2: Anatase unit cell with titanium atoms (gray) and oxygen atoms (red)	3
Figure 3: Wulff Construction truncated bipyramidal.....	4
Figure 4: (101) Surface of Anatase ¹⁴	7
Figure 5: (001) Surface of Anatase ¹⁴	8
Figure 6: Truncated bipyramidal enhances prevalence of the (001) surface	9
Figure 7: NREL current highest reported efficiencies for various solar cell technologies, DSSC technologies can be seen in red in the lower right corner.	14
Figure 8: Cartoon representation of basic dye sensitized solar cell with nanomaterial titania (grey circles), photosensitive dye (maroon circles), and electrolyte (pale purple) the ground “D” and excited “D*” state of the dye is shown on the right	16
Figure 9: Cartoon representation of DSPEC, image courtesy of UNC EFRC, the left side is the electrode where the semiconducting material is deposited and the right side is the counter electrode.....	16
Figure 10: SEM image of Alfa Aesar anatase “32nm” nanoparticle	19
Figure 11: SEM image of as-synthesized multilayered titania nanotubes	20
Figure 12: SEM image of shortened titania nanotubes (left) and nanosheets (right)	22
Figure 13: XRD of nanotube and nanosheets materials a) simulation of standard anatase b) as-synthesized TiNTs c) sTiNTs d) sTiNTs post 300 ° C anneal e)sTiNTs post 350 ° C anneal f) TiNSs	24
Figure 14: TiO ₂ hydrothermal growth without-fluorine (top) and with fluorine (bottom) green arrows represent predominant growth direction.....	25
Figure 15: SEM image of titania nanotiles	26

Figure 16: Low temperature synthesis of ntiles 135 °C for 72 hours SEM (left) and TEM (right) characterization.....	27
Figure 17: TEM image of novel hydrothermally synthesized ntiles.....	28
Figure 18: XRD of Ntiles and anatase	29
Figure 19: SAED pattern for (001) Ntiles.....	30
Figure 20: TEM of various ntile batches: low resolution (top left), edge of nanotile to verify (001) spacing (top right, with magnified inset) and top view of crystallinity (bottom)	31
Figure 21: XRD pre and post 500 °C anneal of ntiles	32
Figure 22: Raman spectra of (001) enhanced ntile sample. A standard anatase nanoparticle film was used for comparison.	33
Figure 23: XPS of ntiles post NaOH wash before and after annealing	35
Figure 24: Titanium nanoparticles from oxygen deficient synthesis.....	38
Figure 25: SEM (top) and EDS (bottom) elemental analysis of oxygen deficient ntile synthesis with titanium nanoparticle resultant	39
Figure 26: SEM images of as-synthesized TiNTs (top left), sTiNTs (top right), TiNSs (bottom left), and Ntiles (bottom right).....	40
Figure 27: Energy diagram of DSSC with the black arrows representing the movement of electrons though the device.....	43
Figure 28: Photograph of nitrogen doped TiNTs, the color ranges from yellow to tan as compared to white undoped TiO ₂ (left), SEM image of nitrogen doped tubes with aggregates.....	45
Figure 29: IR Spectra of Nitrogen Doped TiNT material with bending (B) and stretching (S) modes labeled (left)	46
Figure 30: UV-Vis of N-doped and as-synthesized TiNTs	47
Figure 31: Materials studio model of guanidine carbonate crystal with	

hydrogen (white), nitrogen (blue), oxygen (red) and carbon (grey) atoms	47
Figure 32: XRD Spectra of N-doped TiNTs (red) and theoretical calculation of crystalized Guanidine Carbonate (black)	48
Figure 33: Representation of conduction band filling from applied potential and inter-band transitions (Left) and three electrode set up for applied potential. (Right)	49
Figure 34: Modified cuvette attached to three electrode potentiostat for spectroelectrochemical band edge measurement (left) and zoomed in image of modified cuvette on the right.	50
Figure 35: Band structure calculation of anatase (Left) ⁵⁵ and corresponding density of states (Top Right) ⁵⁵ Using this information a general form of the electron density can be shown (Bottom Right) ⁴⁹	51
Figure 36: Equation for excess surface potential on anatase semiconductor with populated conduction band and general shape of resulting graph.	53
Figure 37: Spectroelectrochemical measurement of band edge in .1M pH1 HClO ₄ for a) standard np film, b)Ntile film c) TiNS film and d) sTiNT film	55
Figure 38: UV-Vis band gap analysis: absorbance curve is blue and inset is band gap transform for sTiNTs (top left) TiNS (top right) and Ntiles (bottom center)	57
Figure 39: CV of Ntile and NP film in 0.1M HClO ₄	58
Figure 40: Zoomed-in CV of Ntile and NP film in 0.1M HClO ₄ from Figure 39	59
Figure 41: Suspension of Shortened Nanotubes	62
Figure 42: SEM Images of drip cast TiNS film (left) and sTiNT film (right)	62
Figure 43: Partially Aligned sTiNTs	63
Figure 44: Unstable Ntile films deposited on glass and FTO specific batch numbers are labeled on the left	64
Figure 45: Tert-Butanol ntile films: binding mechanism (top left) 1:1	

tert-butanol water ntile mixture paste (right) and film deposited from paste (bottom left)	65
Figure 46: Doctor-blade Ntile Film Picture	66
Figure 47: Materials Studio rendering of N719 dye (left) and RuP dye (right)	68
Figure 48: DSSC devices a) active area and b) Pt coated counter electrode	69
Figure 49: Nanosecond transience absorbance of RuP derivatized a) Standard NP Film, b) sTiNT Film, c) TiNT Film.....	71
Figure 50: Nanosecond transience absorbance of TiO ₂ derivatized with RuP a) Standard NP film b) ntile film max signal for both have been normalized to 1 for ease of comparison	72
Figure 51: First 40 μ s of ns TA with lines labeling 50% and 75% decay of signal for RuP derivatized TiO ₂ a) Standard NP film and b) Ntile film.....	74
Figure 52: I-V Curve of sTiNT and TiNS films	77
Figure 53: IPCE measurements of TiNSs and sTiNTs films with standard annealing treatment (300 °C) and TiNSs annealed at 400 °C in an oxygen environment, and sTiNTs annealed at 300 °C in an oxygen environment.....	78
Figure 54: APCE measurements of TiNSs and sTiNTs films with standard annealing treatment (300 °C) and TiNSs annealed at 400 °C in an oxygen environment, and sTiNTs annealed at 300 °C in an oxygen environment.....	80
Figure 55: Photographs of batch 10 spin coated ntile film, batch 11 spin coated ntile film, doctor bladed batch 10 ntile film.	82
Figure 56: Ntile batch synthesis conditions and SEM images of batch 10 (left) and batch 11 (right)	82
Figure 57: I-V Sweeps of N719 derivatized nanotiles batch 10 (left) and batch 11 (right).....	83
Figure 58: IPCE measurement of batch 10 and batch 11 Ntile films	

derivatized with N719 Dye	83
Figure 59: N719 loaded Ntile films deposited on glass (top) and FTO (bottom).....	84
Figure 60: IPCE results of doctor-bladed ntile films with previous spin coated film for comparison.	84
Figure 61: I-V curves of doctor-bladed and spin coated ntile films	85
Figure 62: I-V characterization of standard (101) NP films and (001) nanosheets films from literature, A denotes paste deposition as used in this dissertation and E represents particles deposited from Ethanol suspension ⁷²	86
Figure 63: Circuit approximation of electrode side of DSSC ⁷³	87
Figure 64: Sample Nyquist plot of metal-oxide electrode ⁷³	88
Figure 65: Schematic of Carboxyl and Phosphonate linker groups.....	89
Figure 66: Absorbance of RuP on NP, sTiNT, TiNS, and Ntile films with scattering background removed for direct comparison	93
Figure 67: RuP derivatized films of a) Standard NPs b) TiNSs c) sTiNTs d) Ntile.....	96
Figure 68: Photostability measurements of RuP loaded surfaces in 1 M HClO ₄ of a) Standard NP film b) sTiNT film c) TiNS film d) ntile film.....	98
Figure 69: Phenylphosphonic acid molecule with carbon (grey), hydrogen (white), oxygen (red), and phosphorus (pink)	100
Figure 70: ATR-IR Schematic	101
Figure 71: ATR-IR spectra of bare 32nm anatase, p25, ntiles, and LTiNTs	102
Figure 72: ATR-IR Spectra of TiO ₂ samples without and with being derivatized with PPA.	104
Figure 73: ATR-IR spectra of PPA derivatized TiO ₂ samples with zoomed-in graphs of the O-P-O region (top right) and P=O region (bottom center).	105
Figure 74: TGA analysis of Ntiles with mass changed denoted on blue and the derivative shown in green.	107
Figure 75: ¹ H MAS NMR at low spinning speeds of ntile sample	108

Figure 76: ^1H NMR with longer acquisition time.....	109
Figure 77: ^{31}P NMR of a)PPA crystal b) PPA derivatized Ntiles and c) PPA derivatized 32nm Anatase NPs.....	110
Figure 78: ^{31}P NMR of PPA derivatized a) 32nm Anatase and b) Ntiles with fitting shown in green	110
Figure 79: TiO_2 gel before cooking (left) and particulate caked material with top solution after cooking (right)	118
Figure 80: TiO_2 pellet with top solution removed	119
Figure 81: SEM of nanomaterial students will be producing for solar cell films.....	119
Figure 82: TiO_2 uniform liquid paste suspension	120
Figure 83: Slide with Kapton® Polyimide tape mask and deposition region labeled	121
Figure 84: Annealed TiO_2 film ready for dye uptake	122
Figure 85: Dye sensitization of TiO_2 film, electrode soaking face down in blackberry juice (left) and final film post dye loading and ethanol wash.....	123
Figure 86: FTO with graphite counter electrode sketched on top (grey box).....	124
Figure 87: Counter electrode (top) and Electrode with parafilm and drop of electrolyte (bottom)	124
Figure 88: DSSC device assembly with derivatized TiO_2 film isolated by parafilm (left) and graphite coated counter electrode (center) and a completed cell after electrolyte is introduced (right)	125
Figure 89: DSSC Device testing design.....	126
Figure 90: Blackberry derivatized device	126

LIST OF ABBREVIATIONS

HF	Hydrofluoric Acid
DSPEC	Dye sensitized photoelectrosynthetic cell
DSSC	Dye sensitized solar cell
FTO	Fluorine doped tin oxide transparent conducting electrode
UV	Ultraviolet
SEM	Scanning electron microscopy
TiNTs	As-synthesized multilayered delaminated anatase nanotubes
sTiNTs	Shortened multilayered delaminated anatase nanotubes
TiNS	Titania nanosheets
Ntiles	(001) enhanced anatase nanotiles
NaOH	Sodium hydroxide
HCl	Hydrochloric acid
TEM	Transmission electron microscope
XRD	X-Ray Diffraction
TiBuOx	Titanium(IV) butoxide
SAED	Selective area electron diffraction
EFRC	Energy Frontier Research Center
RuP	$[\text{Ru}^{\text{II}}(\text{bpy})_2(4,4'-(\text{PO}_3\text{H}_2)_2(\text{bpy}))]\text{Cl}_2$ (bpy = 4,4'-bipyridine)
N719	[Di-tetrabutylammonium,cis-bis(isothiocyanato)bis(2,2'-bipyridyl-4,4'-dicarboxylato)ruthenium(II)]
TiO ₂	Titanium Dioxide

HClO ₄	Perchloric Acid
NP	Standard anatase nanoparticles
MLCT	Metal to ligand charge transfer
PPA	Phenyl-phosphonic Acid
ATR-IR	Attenuated total reflectance – infrared
NMR	Nuclear magnetic resonance
LTiNT	As-synthesized long multilayer delaminated anatase nanotubes
TGA	Thermal gravimetric analysis

CHAPTER 1 INTRODUCTION

Titanium dioxide or titania is the most researched single-crystal system in the field of metal oxides. Titania is inexpensive, widely abundant and relatively easy to synthesize. Titania is pervasive throughout human interaction from being used as a coloring additive in food products and medicines, a pigment owing to its brilliant white color, a physical blocker in sunscreen, method for protein splitting, and for photocatalysis to name a few. Due to the ease of synthesis there are many methods to prepare titania in the lab, some of the main ways that titania can be synthesized are, hydrothermally, pulsed laser deposition, atomic layer deposition, sol gel, and anodically. Using the aforementioned synthesis methods titania can be created in various nanostructured morphologies ranging from nanoparticles, nanotubes, nanosheets, nanoribbons, and nanotiles. All of these characteristics have led to a rich field of study surrounding titania and its three main crystal forms; brookite, anatase, and rutile, with the latter being the most stable form. Science has progressed to a level at which it is no longer satisfactory to just know what materials you are working with but to fully understand the surface of the material as well. This dissertation will focus on developing a better understanding of titania's surface and how it can be exploited to develop better materials for solar cells.

1.1 Titania

Titania has three main forms that are found in nature: rutile, anatase, and brookite. Both anatase and brookite are metastable forms which will convert irreversibly to rutile upon extensive heating. Both anatase and rutile are of the tetragonal crystal system whereas brookite is of the orthorhombic crystal system. The titania ore that is found naturally consists of approximately 98% rutile. In the lab synthesis of titania is not limited to this abundance. Extensive work has been done tailoring synthesis of titania to specific morphology and crystal form. Most chemical synthesis methods of nanosized titania produce the anatase phase.

1.1.1 Rutile

Rutile is the most stable and naturally abundant form of titania. The crystal structure of rutile is tetragonal of the point group $4/m\ 2/m\ 2/m$.¹ Rutile is also the most chemically inert form titania. The bright white color of rutile is due to it being the most effective form of TiO_2 for white light scattering. Its inactivity and light scattering ability allows it to be used in sunscreens, paint pigments, and food products.² Rutile is a direct band gap material with a band gap of $\sim 3.0\text{eV}$.^{3 4} The unit cell for rutile is shown in Figure 1.

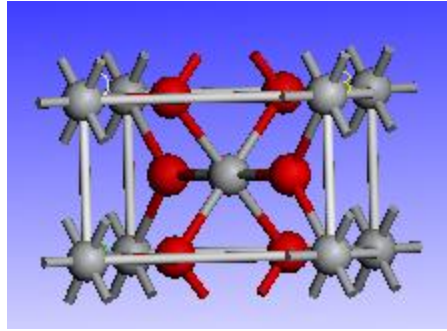


Figure 1: Rutile unit cell with titanium atoms (gray) and oxygen atoms (red)

1.1.2 Anatase

Though anatase is the less naturally abundant form of titania, solution preparation methods typically lend themselves to producing anatase titania.⁵⁻⁹ It is a metastable phase which upon heating at 800 °C or higher it will convert to the more stable rutile form. Anatase is found in a tetragonal crystal structure of the point group $4/m\ 2/m\ 2/m$ and space group $I4_1/amd$ ¹. The most common crystals are acute bipyramidal with perfect cleavage along the [001] and [011] crystal planes. The unit cell for anatase is shown in Figure 2.

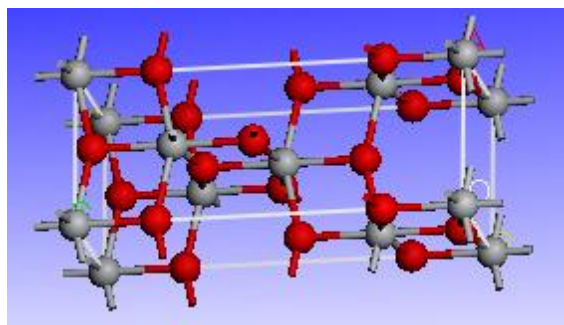


Figure 2: Anatase unit cell with titanium atoms (gray) and oxygen atoms (red)

Anatase has the most reactive surface chemistry of all the forms of titania and is an indirect gap material with a band gap of 3.2eV. This allows for a slightly higher

conduction band energy as compared to rutile.¹⁰ The surface formation energy of anatase crystal planes has been studied and calculated extensively and the results of which are presented in Table 1 as the results of a widely accepted density function theory (DFT) calculation using the Perdew-Burke-Ernzerhof (PBE) two gradient corrected approximation.

Surface	(101)	(100)	(001)	(110)
Surface Energy (J/m ²)	.49	.58	.98	1.15

Table 1: Relaxed surface formation energies for anatase titania¹¹

The (101) surface of anatase both the easiest and most common surface to synthesize owing to its energetic favorability. Using Wulff construction to determine the crystal structure of anatase by minimizing the total surface energy the truncated bipyramidal shape emerges with two main anatase planes; (101), and (001) as seen in Figure 3.

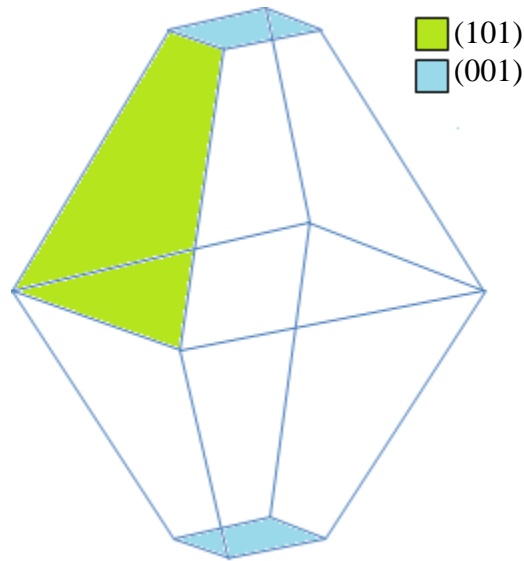


Figure 3: Wulff Construction truncated bipyramidal

The truncated bipyramidal has theoretically and experimentally been verified as the shape of nanoparticulate anatase titania. Based on this Wulff construction it can be estimated that approximately 6% of the surface is the (001) surface whereas the other 94% is the (101) surfaces. This fact is essential and the basis of my dissertation. Extensive work has been dedicated to studying anatase for solar applications owing to its ease of synthesis, cost, and conduction band edge enhancement over rutile.¹⁰

1.1.3 General surface chemistry of anatase

When anatase is synthesized into nanostructures certain properties arise that are different from the underlying bulk material. At the surface where the crystal lattice breaks the manifestation of undercoordinated ions arises. For standard anatase nanoparticles under-coordinated titanium cations result from discontinuities in the lattice this leads to a net positive charge which will attract a lone pairs of electrons. From this it can be seen that the under-coordinated titanium atoms behave as Lewis acid. For reference a Lewis acid is any atom/molecule that can make use of an electron lone pair to create a stable form of its own.¹² For a majority of titania nanomaterial synthesis techniques this unbalanced charge is balanced by the adsorption of hydroxyl groups on the surface. These hydroxyl groups will remain on the surface even after being pumped on at elevated temperatures. The hydroxyl groups on the surface may behave in a manner where they act as acidic sites or basic sites depending on the stoichiometry at the surface. The Lewis acid sites on the titania adsorb molecules in the proximity to neutralize their

charge, it is this reason that they can be sensitized with molecules containing phosphonate or carboxyl linkers.¹³

1.1.4 Anatase the (101) and (001) surface

The two surfaces that will be discussed throughout the duration of this dissertation are the anatase (101) and (001) surface. Non-nanosized titania materials are typically dominated by their bulk properties as the surface contributes minimally to the material. When synthesizing materials on the nano-scale the surface begins to constitute a significant portion of the material and thus surface properties begin to dominate over the bulk. It is for this reason that a thorough understanding of the surface is important to engineer proper materials for the task.

1.1.4a The (101) surface

The (101) surface of titania consists of oxygen atoms that are either 2-fold under coordinated or 3-fold fully coordinated, and titanium atoms that are split between 6-fold fully coordinated or 5-fold under coordinated. The corrugated surface has a sawtooth termination profile due to its non-perfect cleaving. As previously stated the (101) surface of anatase has the lowest formation energy which translates to it being the majority surface in standard anatase synthesis. The surface structure of the (101) surface can be seen in Figure 4.

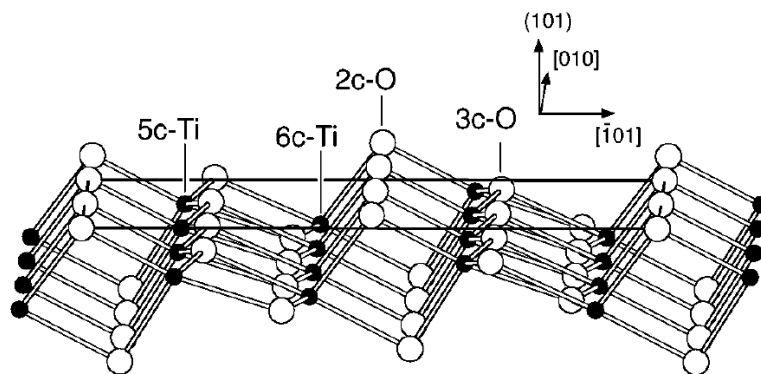


Figure 4: (101) Surface of Anatase¹⁴

1.1.4b The (001) surface

The (001) surface of titania consists of oxygen atoms that are either 2-fold under coordinated or 3-fold fully coordinated and titanium atoms that are all 5-fold under coordinated. The (001) is a perfectly cleaved surface and thus is planar. The under coordinated titanium atoms give rise to some unique properties among which is that it is the most reactive surface of anatase. This reactivity can be seen theoretically and experimentally by the (001) surface dissociatively adsorb water and organic compounds such as methanol whereas the same molecules generally adsorb molecularly on the (101) surface.^{11,15} In turn this translates to the (001) surface being more photocatalytically active than the majority (101) surface. The surface structure of the (001) surface can be seen in Figure 5.

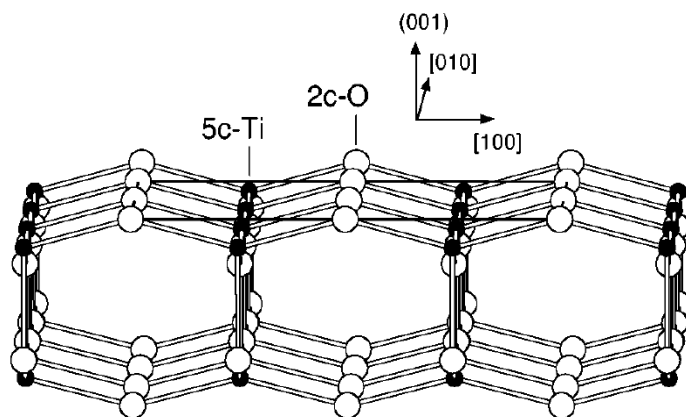


Figure 5: (001) Surface of Anatase¹⁴

Without exposure to other molecules the undercoordinated titania on the (001) surface are stabilized by hydroxyl groups. The hydroxyl groups can be removed with a high temperature $>350\text{ }^{\circ}\text{C}$ anneal of the surface.

Up until recently there has not been much experimental work done on the (001) surface of titania owing to the high energy of formation which makes synthesis tricky. Recently there have been a number of groups that have published results on (001) enhanced TiO_2 most of which involve a chemical inhibitor or capping agent in order to facilitate the growth of the (001) surface.^{9,16-19} This capping agent serves to inhibit the outward growth of the (101) surface and further truncate the bipyramid as seen in Figure 6. This truncation allows for the (001) surface to be a higher percentage of the exposed surface.

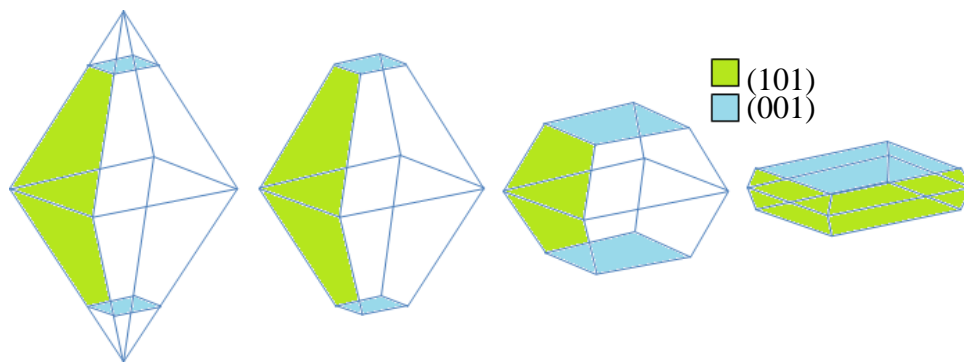


Figure 6: Truncated bipyramidal enhances prevalence of the (001) surface

Truncation can be achieved in a number of ways yielding various morphologies and percentages of the exposed surface that is (001). The (001) surface can also be obtained without the use of a capping agent by being grown via molecular beam epitaxy, chemical vapor deposition, or metalorganic vapor phase epitaxy on single crystal (001) LaAlO_3 or (001) SrTiO_3 ^{20,21}. Since these non-capping agent methods are limited to their substrate in turn they are also limited to their application and thus not useful for solar purposes. The landmark solvothermal/hydrothermal procedure that created microcrystalline anatase with a 47% of the exposed surface being the (001) face was published in *Nature* in 2008 by Yang and colleagues.²² The nanotiles that they synthesized resulted from a titanium tetrafluoride precursor and hydrofluoric acid capping agent and were approximately sized 1.8 micron by 1.8 micron and a little under .5 microns thick. After this initial publication a few more publications came out declaring production of materials via alternative synthesis recipes of varying morphologies that had enhanced expression of the (001) surface over standard anatase nanoparticles.^{16,17,19,23-26} The material with the highest percentage of the exposed surface was created by Wen et. al using Titanium (IV) tetrafluoride as a precursor with 1-butanol as the solvent and HF as the capping agent to

yield nanosheets that were approximately 4 μ m by 4 μ m and 30nm thick with about 99% of the exposed surface being (001)¹⁷. From this literature search I believe that the material that showed the most promise to be used in solar applications was nanosheets that were synthesized from tetrabutyl titanate and hydrofluoric acid yielding particles of size 60nm by 60nm and 7 nm thick with an approximate 89% (001) exposed surface by Han et al.²⁷ And it was with this synthesis that I formed the basis of a novel preparation to produce (001) enhanced ntile materials. Further discussion of the role of the capping agent and how this synthesis is achieved will be found in chapter 2.

1.1.5 Dissertation Outline

In this dissertation I will stress the importance of identifying the surface of the material that is being worked with. I will explore the differences between the (101) and (001) surfaces of anatase and how they relate to the feasibility of dye sensitized photoelectrochemical cells (DSPEC). The current gold standard of stability between a photosensitive dye and the TiO₂ surface is the phosphonate group. Incorporation of the phosphonate group to the photosensitive dye from the previously used carboxyl group has led to enhanced stability over a larger pH range, up to a pH of 4. I will show that further stability can be achieved by taking special care of the TiO₂ surface being used. To do this experimentally I will synthesize several various morphologies of anatase with varying ratios of the (101) and (001) surface. From this I will be able to discern the best surface for increasing stability between the dye and semiconductor. This will additionally lead to a better understanding of what is required to build a proper and effective DSPEC

1.1.6 Solar Technologies

The goal to harness the sun's energy is not new, in 1883 Charles Fritts developed the first solar cell using selenium on a thin layer of gold with a resulting efficiency of less than 1%, not to mention it was exceptionally (prohibitively) expensive. The conversion from sunlight to current appears to be a relatively straight forward task, with many complications. Plants have been able to harness the sun's energy to sustain themselves for eons so why does it appear as though we are so far behind. Even with all this time for plants to develop photosynthesis the overall efficiency of light being converted into useable energy is on the order of 5% for net leaf efficiency, this efficiency is not even as high as the average combustion engine. Where are the losses that contribute to this low efficiency? From *Photosynthesis* by Hall and Rao the initial loss comes from chlorophyll only being able to use photons of energy 400nm-700nm which is only about 47% of the solar spectrum. Of the useable photons another 30% is lost due to incomplete absorption. Furthermore, the process of converting energy to d-glucose is only 68% efficient.²⁸ With these numbers for photosynthesis efficiency how does the efficiency of current scientific technologies compare? The current scope of technologies can generally be divided into four different categories Single and Multi Junction cells, Crystalline Silicon Cells, Thin films and other photovoltaic technologies. Single and multi-junction cells involve 1 or more p-n junctions. The theoretical efficiency for a single junction cell is 34% and the projected theoretical efficiency of an infinite-junction cell could be as high as 87%. The layers of the multi junction cell consist of metal-organic chemical vapor deposition of thin films of materials like gallium arsenide, or indium gallium arsenide. The downside of multi-junction cells is mainly the cost and long term material availability. Currently

the cost is too high to allow widespread technological implementation. Crystalline silicon cells and thin film cells use the same source technology as a single or multi junction cell but with the use of silicon and they suffer from the same disadvantages. As far as the additional photovoltaic technologies they involve use of quantum dots, organic molecules, and dye sensitized solar cells. A compilation of the best reported efficiencies in literature for various solar technologies is reported in Figure 7. In this figure it can be seen that the current record efficiency is approximately 44% for multi-junction cells, with the familiar silicon photovoltaic cell coming in at around 27%. In the lower right portion of the figure it can be seen that the max efficiency for dye sensitized solar cells is currently 12%. Being on the lower end of the current technologies it is worth discussing the reason for pursuing dye sensitized solar cells.

1.1.7 Dye Sensitized Solar Cells & Dye Sensitized Photoelectrosynthetic Cells

Even though the current maximum efficiencies of dye sensitized solar cells is below the other technologies they still have their advantages. The number one reason would be cost, though single crystal silicon is more efficient, it is also prohibitively expensive for wide scale adaption at this point in time. DSSCs lend themselves to be potentially cheaper and allow for larger scale fabrication. With the ability to deposit semiconductors/oxides from sol-gels fabrication then becomes relatively straightforward and simple. Additionally DSSCs lend themselves to being able to be “refreshed” to extend their device lifetime. What this means is that if the electrolyte or dye was no longer performing to standard the whole system could be flooded with new dye and electrolyte without having to physically replace anything allowing it to return to its

original specifications. Additionally, DSSCs can linearly be extended to DSPECs to use sunlight to split water and/or reduce carbon dioxide instead of only producing a current. Water splitting will allow for potentially easier storage of energy to be used when the sun is unavailable.

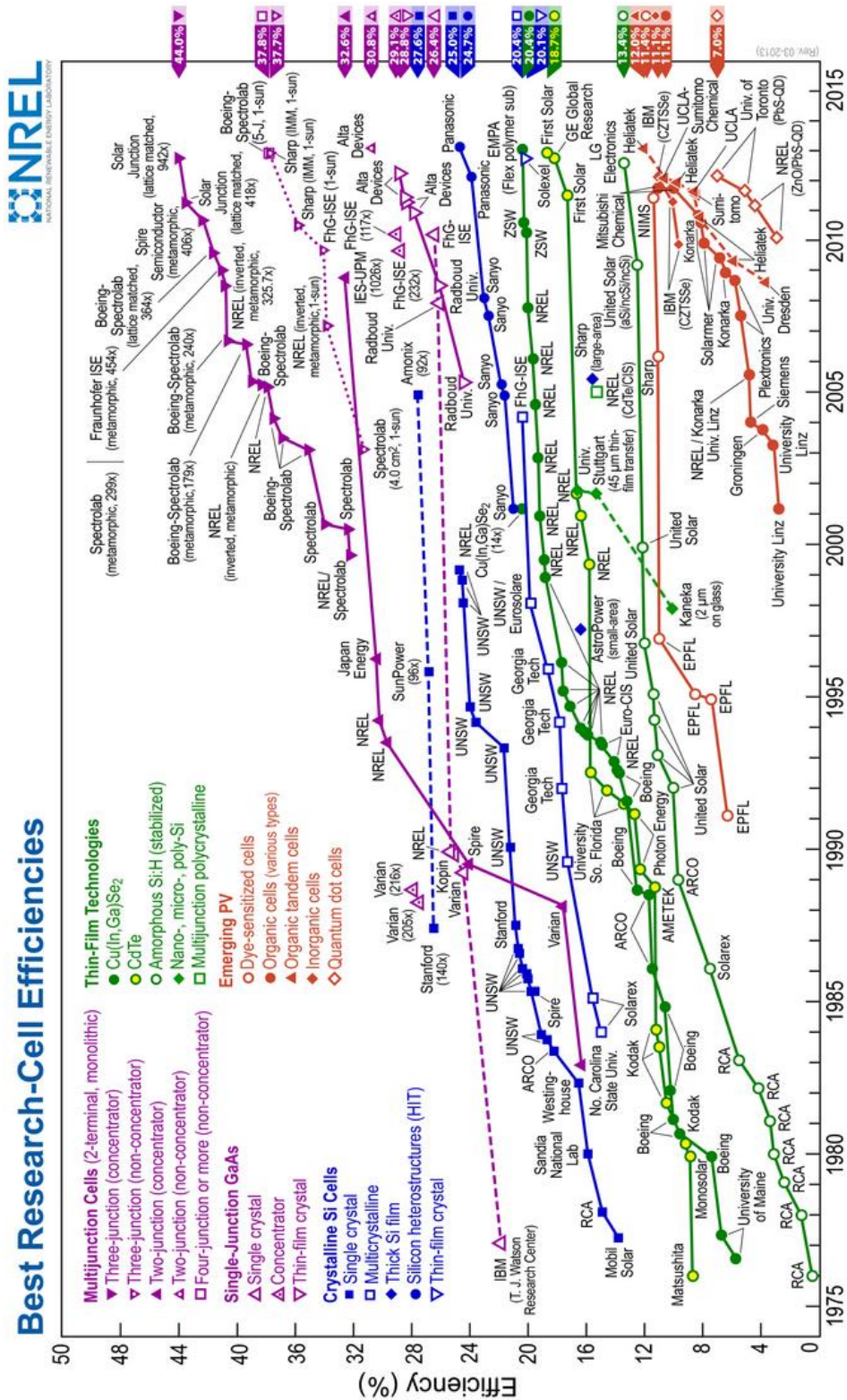


Figure 7: NREL current highest reported efficiencies for various solar cell technologies,

DSSC technologies can be seen in red in the lower right corner.

In 1972 Honda and Fujishima published their group's ground breaking findings in *Nature* showing that titania when exposed to UV light could split water and produce hydrogen gas. This served to renew the interest of the global community to develop technologies that not only converted sunlight to current but to harness sunlight to split water²⁹. Currently, the overwhelming majority of DSSC fabrication is structured around the Gratzel cell. DSSCs are largely credited to being invented by Brian O'Regan and Michael Gratzel in 1988.³⁰ The general constituents of a DSSC are a semiconducting material such as titania, a photosensitive dye, electrolyte, and transparent electrodes. With the band gap of titania residing in the UV region of the spectrum without the use of a coupled photosensitive dye the titania would only be able to make use of ~3% of the solar spectrum. Photosensitive dyes have been designed to attach to the titania surface and enhance the electromagnetic region over which the cell can absorb photons. The setup of the cell is that the photosensitive dye absorbs a photon which promotes an electron to the excited state of the dye; ideally this electron is injected into the semiconductor and shuttled around the circuit to the counter electrode. Less ideally is the outcome that the excited state releases energy and relaxes back to ground state or recombines with the cell electrolyte. In this setup the purpose of the electrolyte is to regenerate/neutralize the dye so that this process can continue without charge build. A cartoon representation of this process can be seen in Figure 8.

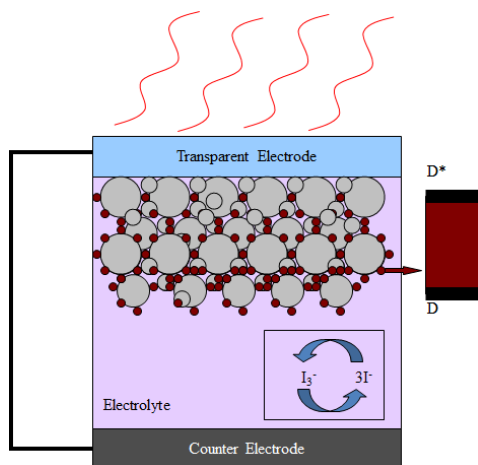


Figure 8: Cartoon representation of basic dye sensitized solar cell with nanomaterial titania (grey circles), photosensitive dye (maroon circles), and electrolyte (pale purple) the ground “D” and excited “D*” state of the dye is shown on the right

With slight modification to this setup the cell can be redesigned to split water into hydrogen and oxygen, and/or reduce carbon dioxide and thus the dye sensitized solar cell can be converted into a dye sensitized photoelectrochemical cell as seen in Figure 9.

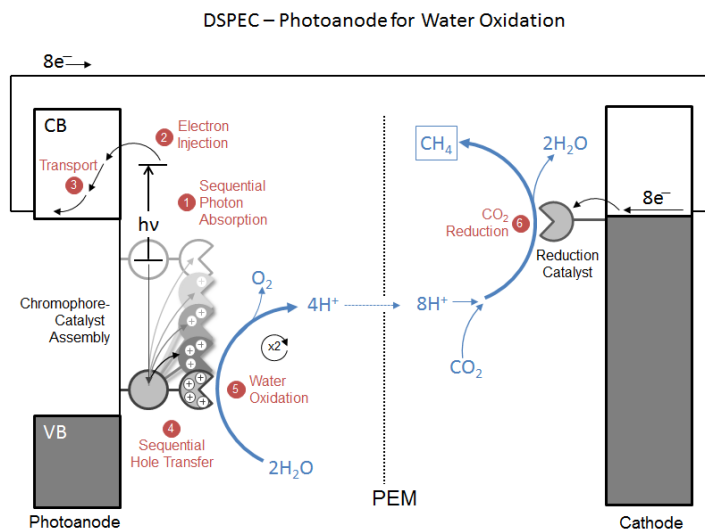


Figure 9: Cartoon representation of DSPEC, image courtesy of UNC EFRC, the left side is the electrode where the semiconducting material is deposited and the right side is the counter electrode.

For a DSPEC the dye is replaced with a chromophore catalyst assembly which absorbs photons to promote electrons to the excited state and uses the electrons to perform water oxidation on the photoanode side and allows electrons injected into the semiconductor to travel the circuit to be used for carbon dioxide reduction. In order for this whole process to work the dye/chromophore catalyst assembly must be stable on the surface of the semiconductor under illumination and in aqueous conditions. This requirement turns out to be no trivial task as water is an excellent solvent and sunlight has an abundance of energy to remove molecules from the surface. Most attempts to increase the dye stability have been centered on modification of the anchor groups that attach the dye to the semiconductor surface. This has been accomplished from swapping out the traditionally used carboxyl groups to phosphonate groups which improved stability over a broader pH range.³¹⁻³⁵ However to my knowledge minimal to no work has focused on the underlying semiconductors surface contribution to stability. Anatase has been the focus of massive amounts of research in the solar cell/fuel community however with all of these studies minimal work has focused on studying the effect that the semi-conductor surface has on the stability of adsorbed molecules. This dissertation will show that the scientific blind spot of the titania surface offers a rich field of study and an improvement on current stability standards and device characteristics.

CHAPTER 2 TITANIA SYNTHESIS AND CHARACTERIZATION

2.1 Commercially Available Titania Morphologies

In this dissertation several morphologies of titania are used to experimentally elucidate an understanding of the molecular binding on anatase titania. Due to the extensive research centered on titania there are several nanomaterial forms that are commercially available. The two commercially available nanomaterial forms that will be dealt with in this dissertation are Degussa p25 and 32nm anatase nanoparticles. Degussa p25 or titanium (IV) aerioxide has been well studied in literature and its structure and morphology is well understood and widely accepted. The crystallographic composition of p25 is ~80% anatase and 20% rutile/amorphous.³⁶ It is widely used for studies involving photocatalysis owing to the majority of the material consisting of the more reactive anatase form of titania. The particulate size of p25 nanoparticles is approximately 21 nm in diameter, and from Brunauer-Emmett-Teller (BET) measurements p25 has a specific surface area (SSA) of approximately 50 m²/g based on measurements supplied by Sigma-Aldrich (the manufacturer) and confirmed in literature³⁶. Additionally 99.9% pure anatase nanoparticles are commercially available from Alfa Aesar. The size of the anatase nanoparticles used in these studies is of a 32nm diameter and 45m²/g SSA as detailed from the manufacturer. We have confirmed that

approximate size of the nanoparticles is larger than the states 32 nm as they range from 30-100 nm via scanning electron microscopy (SEM) as shown in Figure 10.

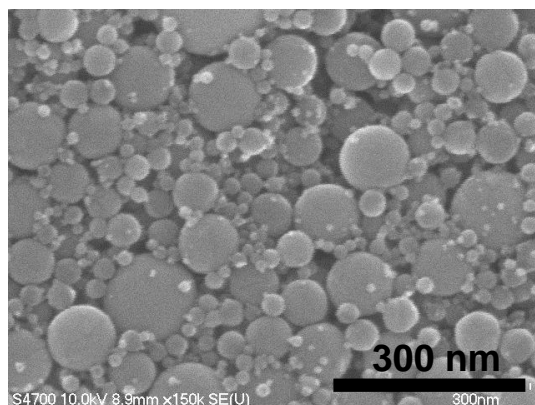


Figure 10: SEM image of Alfa Aesar anatase “32nm” nanoparticle

2.2 Novel Synthesized Titania Morphologies Synthesis and Characterization

The morphologies of titania that are synthesized in this work are multilayered delaminated titania nanotubes which are further processed into shortened nanotubes and nanosheets, as well as (001) enhanced titania ntiles. The reasoning for choosing these specific morphologies is the uniqueness of their high energy (001) type surfaces. As previously mentioned it is difficult to synthesis nanocrystalline materials with the (001) surface exposed due to its high formation energy. The very porous nanotubes exhibit an (001)-like surface that is hydroxyl terminated and the nanosheets are a very thin surface of (001) anatase. The method used to produce the nanotubes and nanosheets does not involve a capping agent which makes the synthesis very unique. To my knowledge it is the only such (001) titania hydrothermal synthesis without a capping agent to have been reported in literature. The (001) enhanced nanotiles (Ntiles) are a bit different owing to being larger crystalline particles and depending on the ratio of the side length to the

thickness the amount of the surface that is (001) can range from 70-90%. Synthesizing these materials requires varying approaches that will be discussed in the next section.

2.2.1 Multilayered delaminated anatase nanotubes

Multilayered delaminated titania anatase nanotubes (TiNTs) are produced from a hydrothermal reaction of sodium hydroxide (NaOH) and the afore mentioned “32nm” anatase nanoparticles. TiNTs were synthesized by hydrothermally treating anatase nanoparticles in alkaline conditions.³⁷ 4 g of anatase nanoparticles (Alfa-Aesar) are suspended in 400 mL of 10 M NaOH solution in a Teflon coated autoclave. After mixing the contents are kept for 72 hours in an oven at 135 °C. After being allowed to cool to room temperature, the slurry was then washed repeatedly with 0.1 M hydrochloric acid (HCl) and deionized water until the resulting pH falls within the 5-7 range. The white powder was then dried at 50 °C and collected. These TiNTs can further be processed into shortened nanotubes and nanosheets. A scanning electron microscopy image of the as-synthesized tubes can be seen in Figure 11. SEM was performed with a Hitachi 4700 SEM with 10 keV accelerating voltage and 10 mA current.

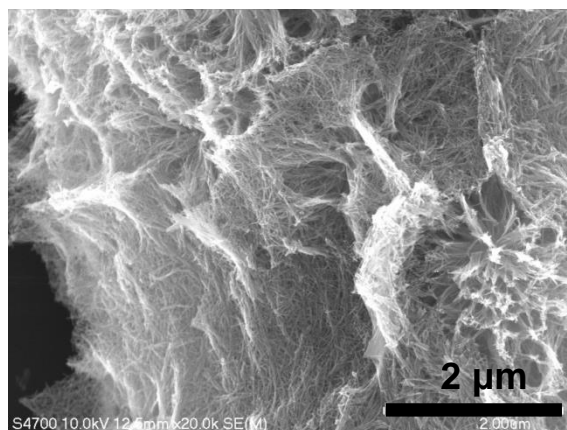


Figure 11: SEM image of as-synthesized multilayered titania nanotubes

The structure of the as-synthesized TiNTs is based on the delaminated anatase model first discovered by my predecessor Greg Mogilevsky.³⁸ The tubes have an inner diameter of approximately 5 nm and an outer diameter of approximately 10 nm. They are constituted of several layers of concentric tubes with inter layer spacing of approximately 8 Å. The as-synthesized tubes are of lengths over a micron and form large tangled aggregates as seen in Figure 11. These aggregates hinder uniform film production and thus need further processing to be viable for solar applications. The tubes exhibit a 100% (001)-like surface, with hydroxyl groups terminating the surface attached to the undercoordinated titanium of the (001) surface.³⁸ The unique structure and surface chemistry of these tubes has been shown to have enhanced reactivity as compared to standard anatase with the (101) surface being predominantly exposed. This is evident in studies that have shown dissociative adsorption of water and enhanced catalytic activity for reactions with molecules such as the nerve agent VX.³⁹ The nanotube surface is shown to chemically break down VX at a much faster rate than the previously studied anatase.

2.2.2 Shortened nanotubes and nanosheets

The collected TiNTs powder from the previous hydrothermal synthesis is further processed into either shortened nanotubes or nanosheets. 100 mg of as-synthesized TiNTs were mixed in 75 mL deionized water along with 25 g grinding media consisting of 100 µm diameter ZrO/Silica (Glenn-Mills) beads in a grinding vessel equipped with a Teflon stirring blade. The grinding vessel was put into an ice water bath and into a Bead Beater

grinder (BioSpec). The sample is then ground for 30 minutes.³⁸ After grinding, the solution was decanted from the grinding media which settled to the bottom of the container immediately. After centrifugation, to remove the remaining uncut long nanotubes, the resulting supernatant solution contained shortened nanotubes (sTiNTs) and remained in a stable colloidal suspension for many weeks. A Millipore Stericup (250 mL capacity) 0.22 μm PVDF disposable sterile vacuum filter was used to filter the suspension, and the resulting filtrate was used for coating substrates. To produce nanosheets (TiNS) the same procedure was employed but without an ice bath. Powder samples were collected for further SEM imaging and XRD by drying the suspension at 80 °C on a cleaned glass slide and collecting the resulting residue. An SEM image of the sTiNTs and TiNS can be seen in Figure 12.

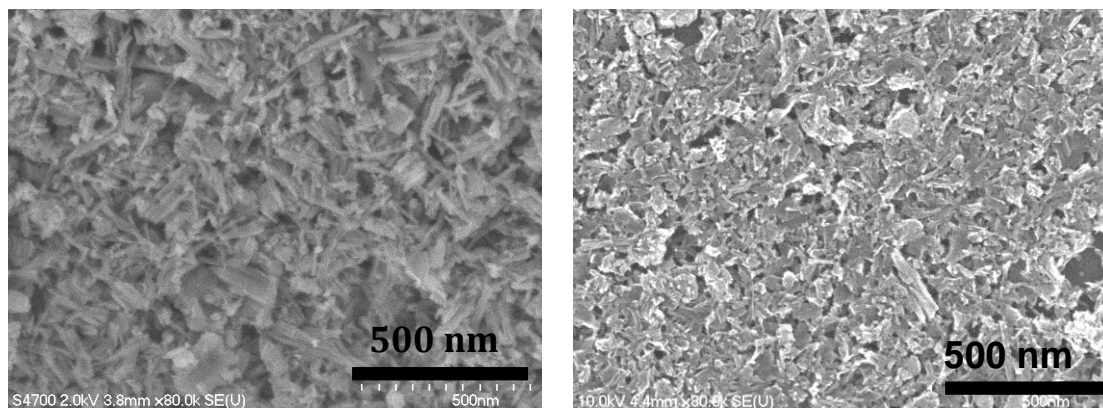


Figure 12: SEM image of shortened titania nanotubes (left) and nanosheets (right)

The resulting sTiNTs are of varying length 50-150 nm and due to the steric repulsion from the surface charge of the nanomaterials in water the sTiNTs and TiNSs are capable of forming stable suspensions indefinitely making them suitable for drip casting into films. From the hot milling process the sheets are single crystalline layer of approximately 1.4 nm thick and range in size much like the sTiNTs. Since the cutting

process is very rough and involves a large amount of kinetic energy the final products tend to have a bit of a mixture between sTiNTs and TiNS. Special care was taken to characterize batches prior to use to ensure a majority of sTiNTs or TiNS for proper comparison.

The unique structure of the delaminated anatase goes away when any of the materials are annealed above 300 ° C, this is confirmed from the resulting XRD pattern which shows all of the features observed in anatase (Figure 13). The 25° peak corresponding to the (101) anatase plane is completely restored while the intensity of the interlayer 10°, (101) plane 24° and (103) 28° DA peaks decrease. The peaks at $2\theta = 13^\circ$ and 28°, have large FWHM values of 4.4° and 5.7°, corresponding to small 3.6nm and 2.8nm clusters respectively, and their intensities are greatly reduced. The interlayer peak at 10°, corresponding to the (002) DA plane, increases to 13° meaning that the d-spacing is decreases to $\sim 6.5 \text{ \AA}$ as the structure collapses closer to anatase. The 49° peak that corresponds to the axial direction of the nanotubes remains unchanged even after heating to 350 °C because the resulting anatase rods maintain high aspect ratio geometries found in the nanotubes.

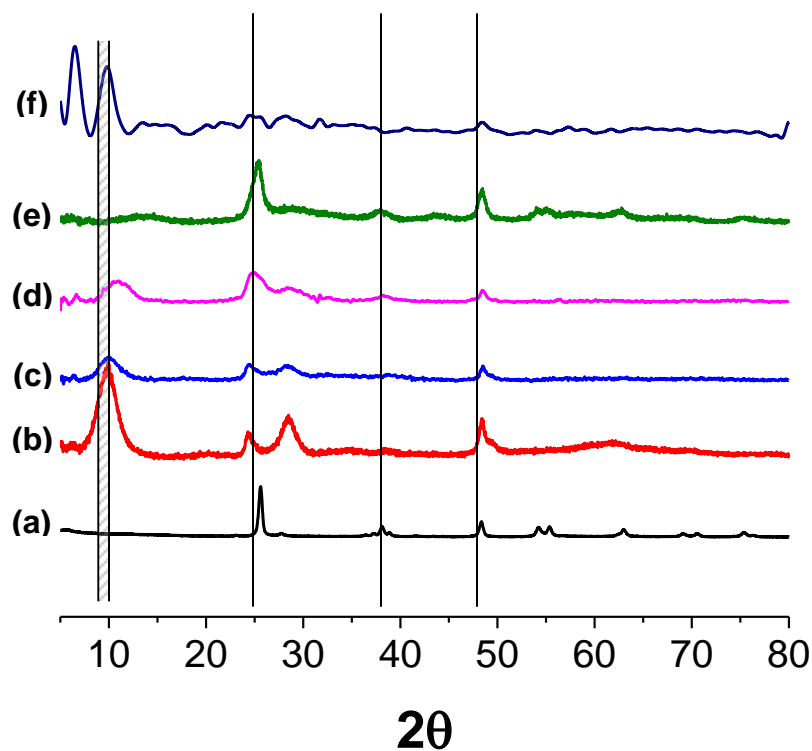


Figure 13: XRD of nanotube and nanosheets materials a) simulation of standard anatase b) as-synthesized TiNTs c) sTiNTs d) sTiNTs post 300 ° C anneal e) sTiNTs post 350 ° C anneal f) TiNSs

2.2.3 (001) Enhanced Titania Nanotiles

The (001) enhanced titania nanotiles (ntiles) are a novel material based on the literature procedure first published by Han and coworkers with changes made to the reactant materials, concentrations, and baking conditions.²⁷ Ntiles were synthesized hydrothermally by a hydrolysis reaction of Titanium(IV) butoxide (Acros) and ~48% HF in the fashion 21 mL of Titanium(IV) butoxide was mixed with slow addition of 2.4 mL of ~48% HF in a Teflon coated autoclave. The contents were kept for 72 hours at 135 °C or 24 hours at 180 °C. The slurry was then washed repeatedly with deionized water and

ethanol. The white powder was then dried and collected for characterization or incorporated into a paste for device measurements.

The general hydrolysis reaction between TiBuOx and water results in titanium dioxide and butanol. The effect of the fluorine incorporation selectively inhibits growth directionally. Since the fluorine attaches to the titanium atoms it inhibits the creation of bridging oxygen groups and hence directionally caps the growth of the crystal. This can be represented schematically as shown in Figure 14.

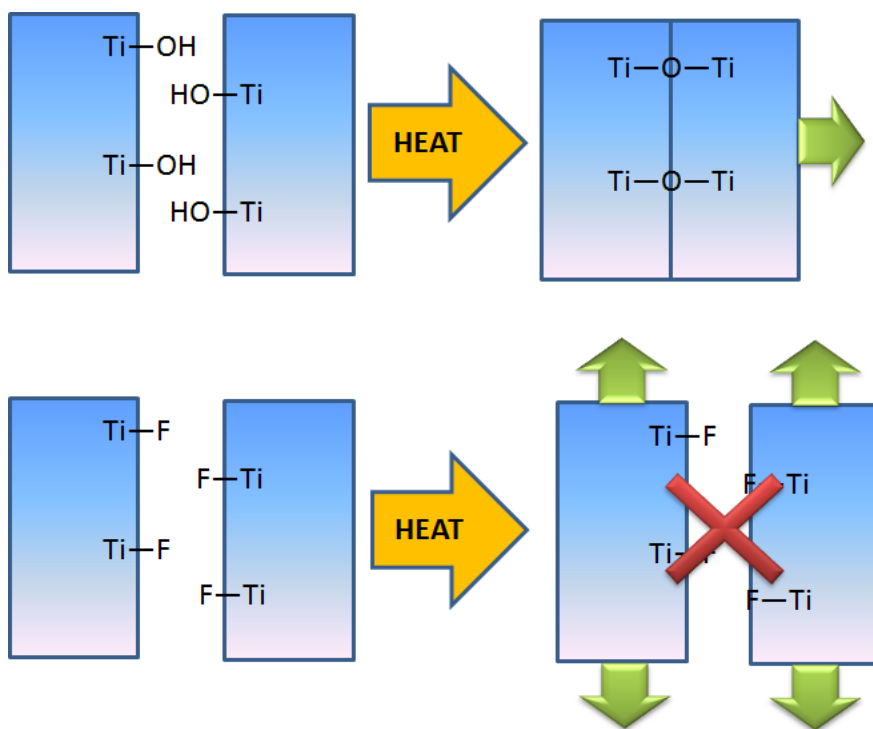


Figure 14: TiO_2 hydrothermal growth without-fluorine (top) and with fluorine (bottom) green arrows represent predominant growth direction

An SEM image of the as-synthesized ntiles resulting from a standard reaction between TiBuOx and 48% aqueous HF can be seen in Figure 15.

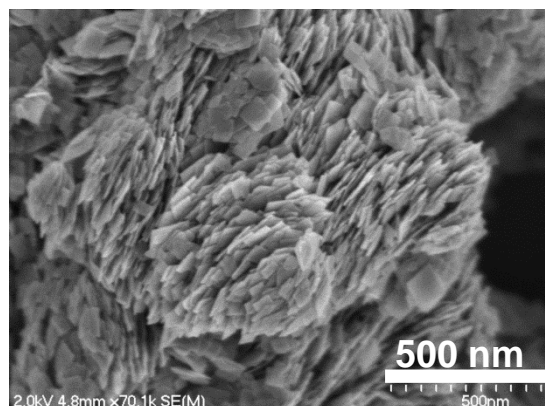


Figure 15: SEM image of titania nanotiles

Varying the conditions used to synthesis the nanotiles yields tiles of differing sizes as can be seen in Table 2. Side lengths were determined using SEM and TEM.

Batch	TiBuO _x (mL)	HF (mL)	Temperature °C	Time (hours)	Side Length (nm)
1	21	2.4	170	24	40
2	21	2.4	200	24	70
3	21	2.4	150	24	40
4	21	1.6	200	24	90
5	21	1.6	180	72	80
6	21	1.6	180	24	80
7	21	1.6	180	24	40
8	21	2.4	135	24	20
9	21	1.6	170	24	60
10	21	2	180	24	60
11	21	2	135	72	10-20

Table 2: Synthesis conditions and corresponding nanotile sizes

Lowering and elongating the synthesis temperature and reducing the amount of HF present serves to reduce the size of the ntiles. The crystalline structure of all batches of the ntiles was confirmed using SEM, TEM, and XRD.

By allowing for alternate synthesis parameters a complete novel material was created. This novel material is much smaller than other synthesized batches and a

slightly different morphology, though it retains its anatase structure. This new material resulted from a synthesis at 135 °C for 72 hours; the resulting ntiles were irregular and porous as seen in Figure 16.

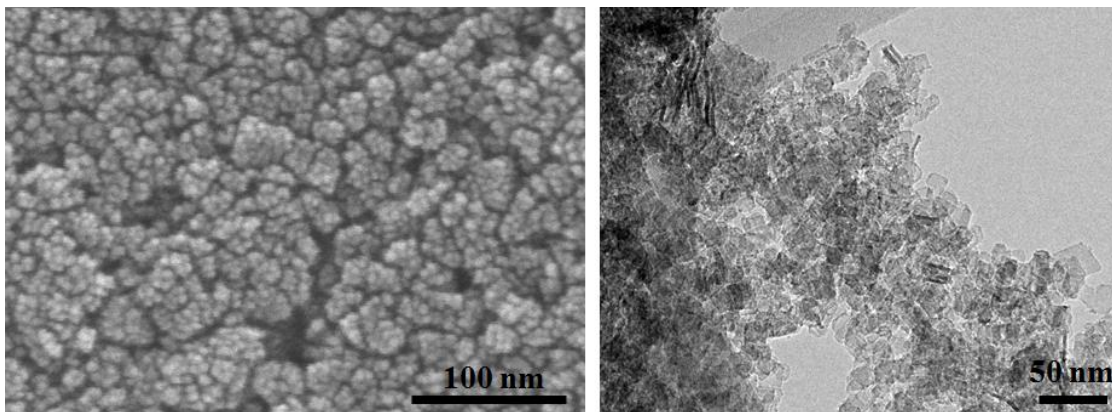


Figure 16: Low temperature synthesis of ntiles 135 °C for 72 hours SEM (left) and TEM (right) characterization

These tiles were predominantly 10-20nm in side length and crystalline. The synthesis also resulted in some (<10% of total material) larger tiles with side length 20-40 nm as can be seen in the high resolution TEM image in Figure 17.

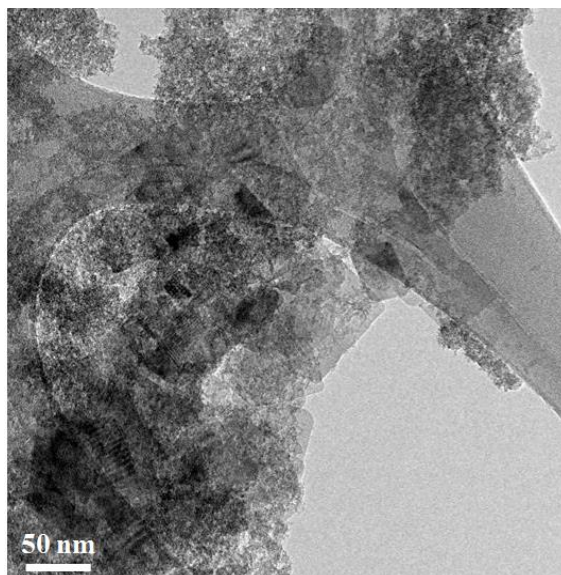


Figure 17: TEM image of novel hydrothermally synthesized ntiles

The x-ray diffraction (XRD) characterization was performed using monochromatic Cu 40 kV/40 mA (0.15405 nm) radiation at 0.25°/min with a resolution of 0.02°. Comparing the XRD spectra of the tiles to standard anatase confirmation can be made that the tiles are indeed anatase (Figure 18.) Characteristic broadening of the peaks can be seen in the ntile sample due to the nano-sizing of the tiles and can be used to calculate the size of the nanoparticles.

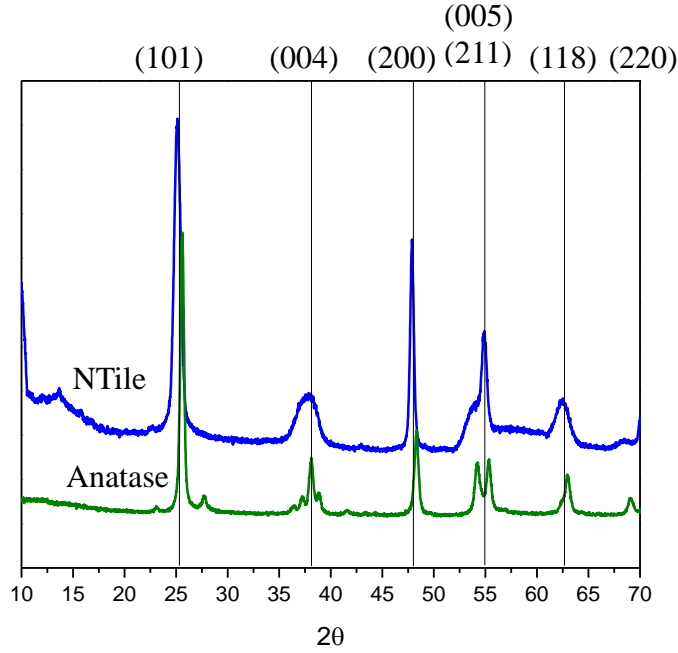


Figure 18: XRD of Ntiles and anatase

This sizing is achieved with the Scherrer formulas shown in Equation 1 $\Delta d = \frac{0.9\lambda}{B(\theta)\cos(\theta)}$.

$$\Delta d = \frac{0.9\lambda}{B(\theta)\cos(\theta)}$$

Equation 1: Scherrer Equation

The thickness is attained for the crystal direction that is perpendicular to the peak being analyzed, with λ being the x-ray wavelength, in this case 1.5418 Å, and $B(\theta)$ the width of the peak at FWHM. Applying this formula to the (004) peak of the nanotiles in Figure 18, the thickness of the tiles can be calculated to be ~4.8 nm which is consistent with the TEM images of the tiles seen in Figure 20. When looking at the tiles with TEM edge on the lattice spacing can be determined. This spacing confirms that the large plane of the

ntiles are indeed the (001) plane. Over a survey of numerous batches the lattice spacing was generally very close to the 0.234 nm that separate consecutive (001) planes. The TEM was also used to perform selective area electron diffraction (SAED) to further characterize the crystallinity of the ntiles and the resulting diffraction pattern can be indexed to pure phase anatase as seen in Figure 19. The SAED pattern was matched up with literature reference to confirm anatase.²⁷

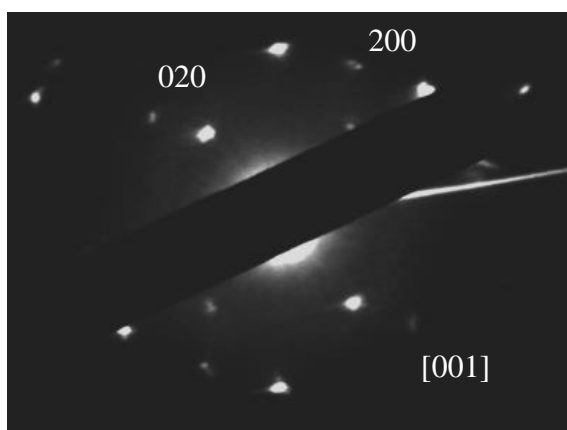


Figure 19: SAED pattern for (001) Ntiles

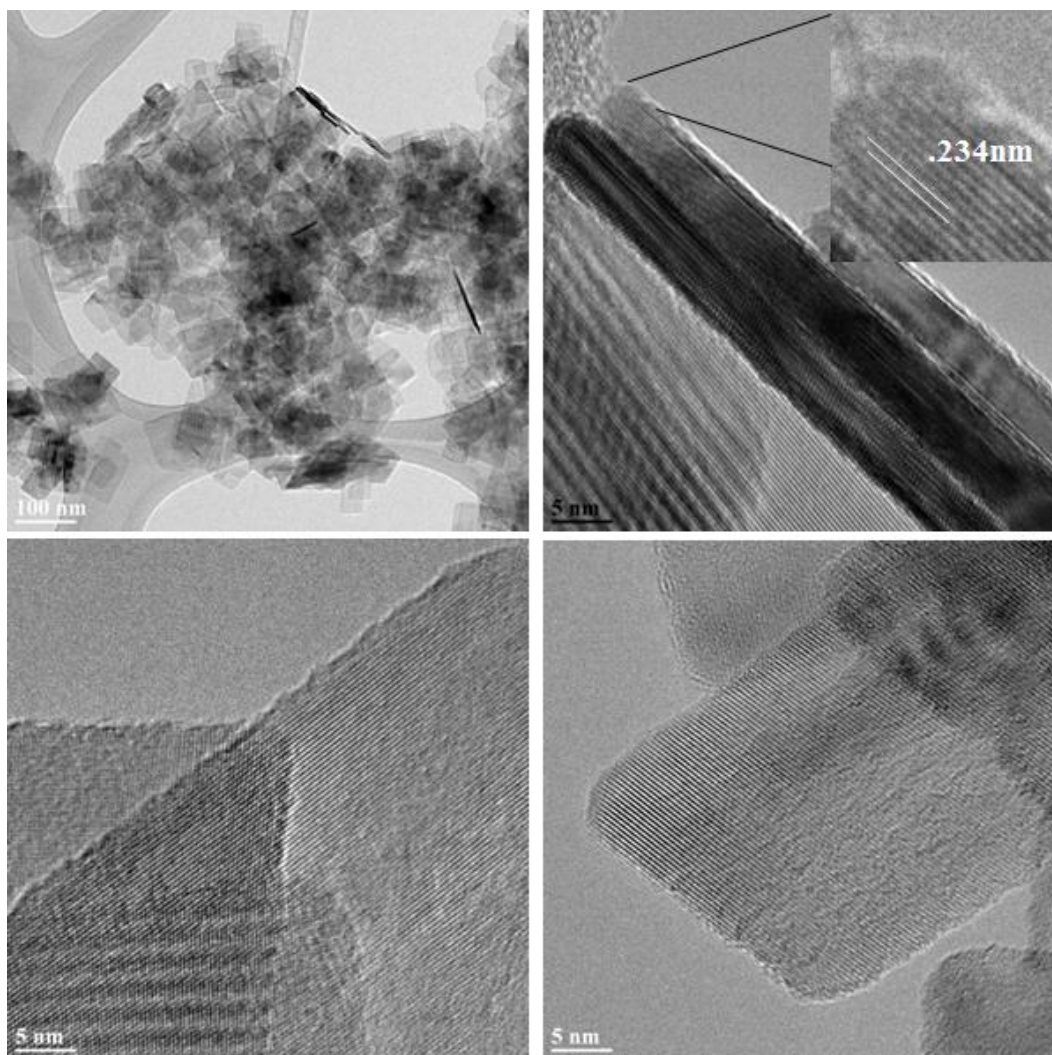


Figure 20: TEM of various ntile batches: low resolution (top left), edge of nanotile to verify (001) spacing (top right, with magnified inset) and top view of crystallinity (bottom)

Both XRD and TEM show that the hydrothermally synthesized ntiles are crystalline. To verify the structural stability of the tiles upon annealing XRD was performed before and after a 500 °C anneal. This temperature is higher than any that would be used in the processing of the ntiles. The peaks of the ntiles narrow consistent with a growth of the crystal size which is indicative of improved connectivity between the individual tiles. The location of the peaks remains the same and the material keeps its anatase structure

after annealing as evident in Figure 21. In addition to improving crystallinity and connectivity between adjacent ntiles annealing the material serves to remove residual fluorine from the surface and allow for any oxygen vacancies or defects to be healed.

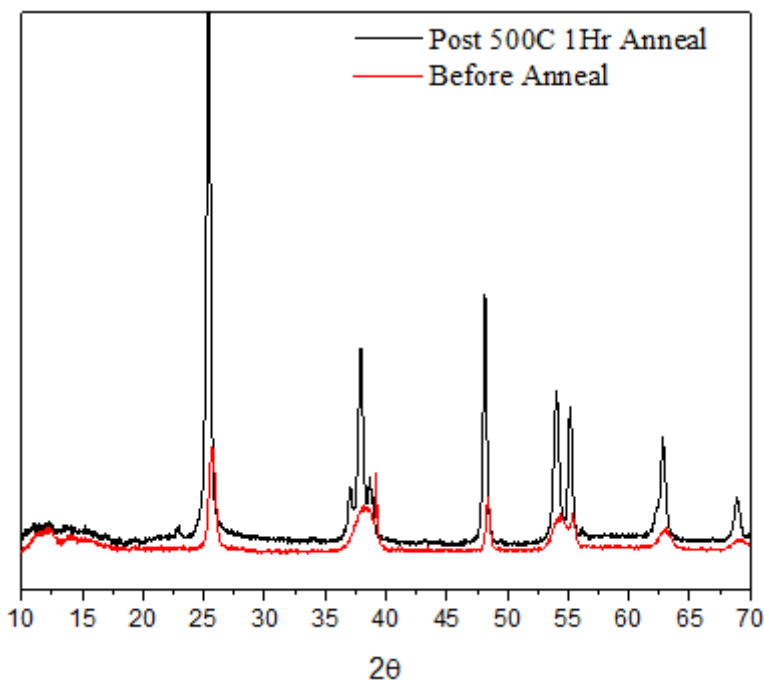


Figure 21: XRD pre and post 500 °C anneal of ntiles

Additionally the ntiles were characterized with Raman spectroscopy to probe the (001) surface as compared to standard nanoparticles. The theory of the Raman measurement is incoming light will interact with the atomic bonding and electrons in the surface of the materials. The incoming light will excite a molecule into a virtual excited state, and when the molecule relaxes it will emit a photon and likely return to a different vibrational and rotational state. The change in the state will be evident in the shift away from the wavelength used to excite the surface. If the frequency shift of the surface is positive it is denoted as a Stokes shift and if the shift is negative it is referred to as an anti-Stokes shift.⁴⁰ This measurement gives valuable insight about the surface bonding in

the material being looked at. For comparison a standard anatase nanoparticle film was used as well as seen in Figure 22.

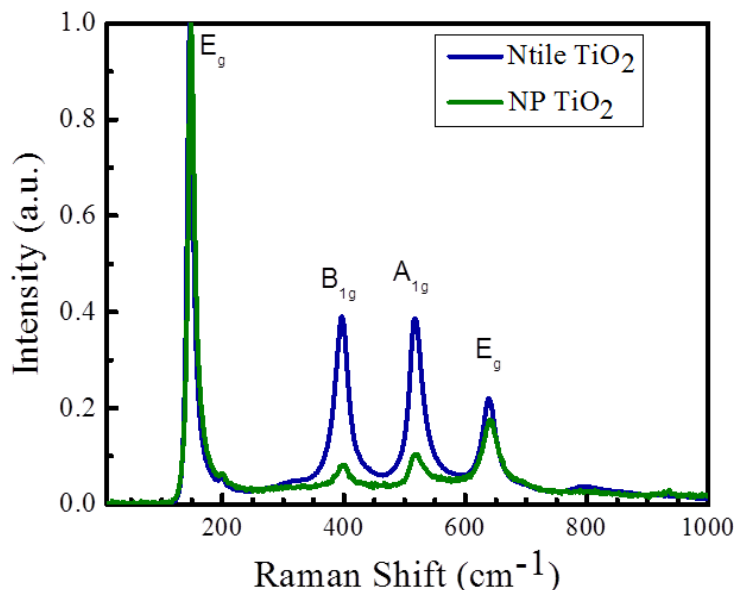


Figure 22: Raman spectra of (001) enhanced ntile sample. A standard anatase nanoparticle film was used for comparison.

Anatase has six Raman active modes listed as: ($A_{1g} + 2B_{1g} + 3E_g$) which can be seen in Figure 22⁴¹. The peaks for both anatase samples can be interpreted as follows: B_{1g} is due to symmetric bending vibration of the O-Ti-O bond, A_{1g} is anti-symmetric bending vibration of the O-Ti-O bond and E_g results from symmetric stretching vibration of the O-Ti-O bond.⁴² The enhancement of the magnitudes of the B_{1g} and A_{1g} signals for the (001) ntiles as compared to the standard nanoparticles is due to the enhanced symmetry of the (001) surface and this could translate to less defects on the ntiles as compared to the standard nanoparticle film which will be discussed in more detail later.

The motivating factor to enable synthesis of the (001) enhanced materials is due to the fluorine acting as a capping agent. It is imperative that the fluorine be removed as to not hinder the potential photocatalytic activity of the titania.⁴³ Additionally, the Ti-F

bond on the (001) surface will act as an electron trap site due to the large electronegativity of fluorine which will translated to a reduction of the likelihood of electron transfer.⁴⁴ Allowing the surface to remain fluorine terminated would facilitate back electron transfer and hence reduce device efficiency. Literature references noted that washing with a 0.1 M NaOH mixture was enough to remove the fluorine from the surface and replace it with a hydroxyl group via a simple ion exchange.²⁷ To verify that the fluorine was removed from the surface XPS was performed on the tiles at various points during the washing procedure. As it can be seen in Figure 23 a NaOH wash alone is not enough to remove the fluorine from the surface. If the NaOH wash is coupled with an hour long 450 °C anneal in atmosphere the remaining fluorine can be removed from the surface. The fluorine 1s signal located at 686 eV is still very evident after the NaOH wash. Using the areas of the observed elements an estimation of the elemental concentration can be calculated. This elemental concentration is only valid for approximately the top 1-10 nm of the material. This is due to the x-rays are not penetrating far enough to eject deeper electrons, and deeper ejected electrons not being able to escape the material and make it to the detector.

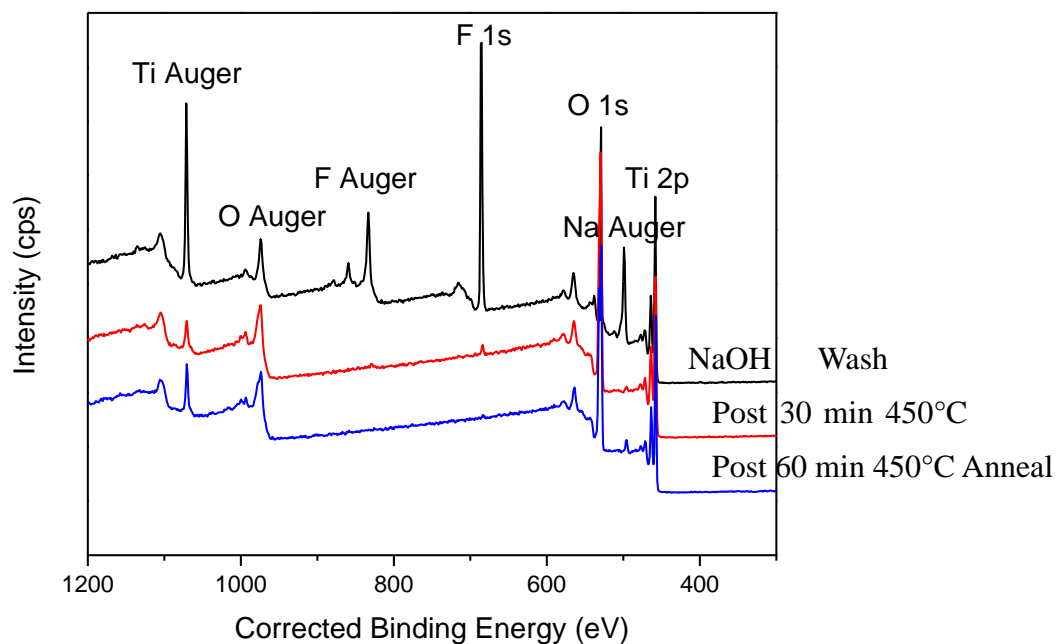


Figure 23: XPS of n-tiles post NaOH wash before and after annealing

Taking high resolution scans of the dominant elements: C, O, Ti, F and Silicon (the substrate) and integrating their area calculation of the atomic concentrations can be attained and from this it becomes clear that the fluorine is not removed from the surface after washing. A 30 minute 450 °C anneal serves to diminish the concentration from 43% to 1.7%, and a 60 minute 450 °C anneal brings the fluorine concentration to much less than 1% as seen in Table 3.

	Atomic Concentration %		
	NaOH Wash Only	Post 450°C 30 min Anneal	Post 450°C 60 min Anneal
C(1s)	5.36	2.18	6.24
O(1s)	31.38	56.98	56.45
Ti (2p)	13.3	26.5	26.28
F (1s)	43.02	1.72	0.29
Si (2p)	6.93	12.61	10.75

Table 3: Atomic concentrations calculated from XPS spectra for ntile samples after washing and subsequent anneals. Fluorine concentration is highlighted in red.

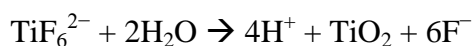
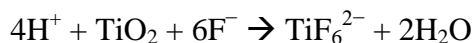
Various literature studies have shown that the fluorine ions replace the hydroxyl groups located on the under-coordinated titanium. The fluorine ions will additionally take the place of some of the additional oxygen atoms on the surface. The presence of fluorine on the surface affects how dye bind to the surface and thus is unfavorable for solar fuel and photocatalytic degradation applications.⁴³ As you can see in the presented XPS data in Table 3 after subsequent anneals the oxygen content increases and the fluorine content goes away. These annealing treatments are vital to prepping the ntile material to properly make use of the (001) surface.

2.2.4 Fluorine and the (001) surface

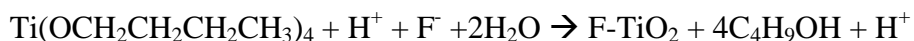
As previously mentioned one of the main methods of facilitating the growth of the (001) surface involve a capping agent. The use of a capping agent in nanomaterial synthesis is to inhibit or stabilize growth. In the synthesis used here the capping agent is Fluorine and its purpose is to lower the formation energy of the (001) surface so that it becomes the more favorable surface during synthesis.

2.2.5 Nanotile synthesis anomalies and variations

Using hydrothermal synthesis methods to create a material leaves room for different materials to be produced by variation in the reactant amounts. The typical reaction for synthesis of ntiles is a hydrolysis reaction of titanium butoxide as previously indicated. For reference, hydrolysis is the breaking of chemical bonds of a molecule by the addition of water. Specifically for the ntiles this is achieved by the water used to dilute the HF to 48%. Incorporation of fluorine ions in the form of an acid allows for the following reaction with TiO_2 involving a dissolution and recrystallization step as can be seen⁴⁵:



The general reaction is as follows:



From this it can be seen by varying the ratio of reactants it is possible to attain different products. The main variation studied here is a under-saturation of oxygen in the reactants. This can be achieved a couple different ways, the first of which is a reduced amount of water in the starting reactions. The minimal ratio by volume found to still yield TiO_2 product was 20 mL of TiBuOx with 1.6 mL 48% HF. Other oxygen-reducing methods discovered were to allow the reaction to progress too quickly allowing for quick escape of oxygen containing gas which also reduces the amount of available oxygen species. Lastly, if the stainless steel pressure vessel is not sealed completely during synthesis oxygen can also escape the vessel. To ensure that this does not occur the vessel should

be sealed carefully with teflon tape to ensure that a majority of the reactants remain in the synthesis vessel. Performing a synthesis which allows for a reduction in oxygen yields a material that is predominantly titanium based and black as shown in Figure 24.



Figure 24: Titanium nanoparticles from oxygen deficient synthesis

A cursory characterization of the material showed that the product was nanoparticulate in nature and dominated by titanium. The ~ 40 nm in diameter titanium nanoparticles created were characterized with SEM and EDS to determine form and chemical composition as seen in Figure 25. Since this material was not of use for the intended purpose of solar fuels it was not pursued further.

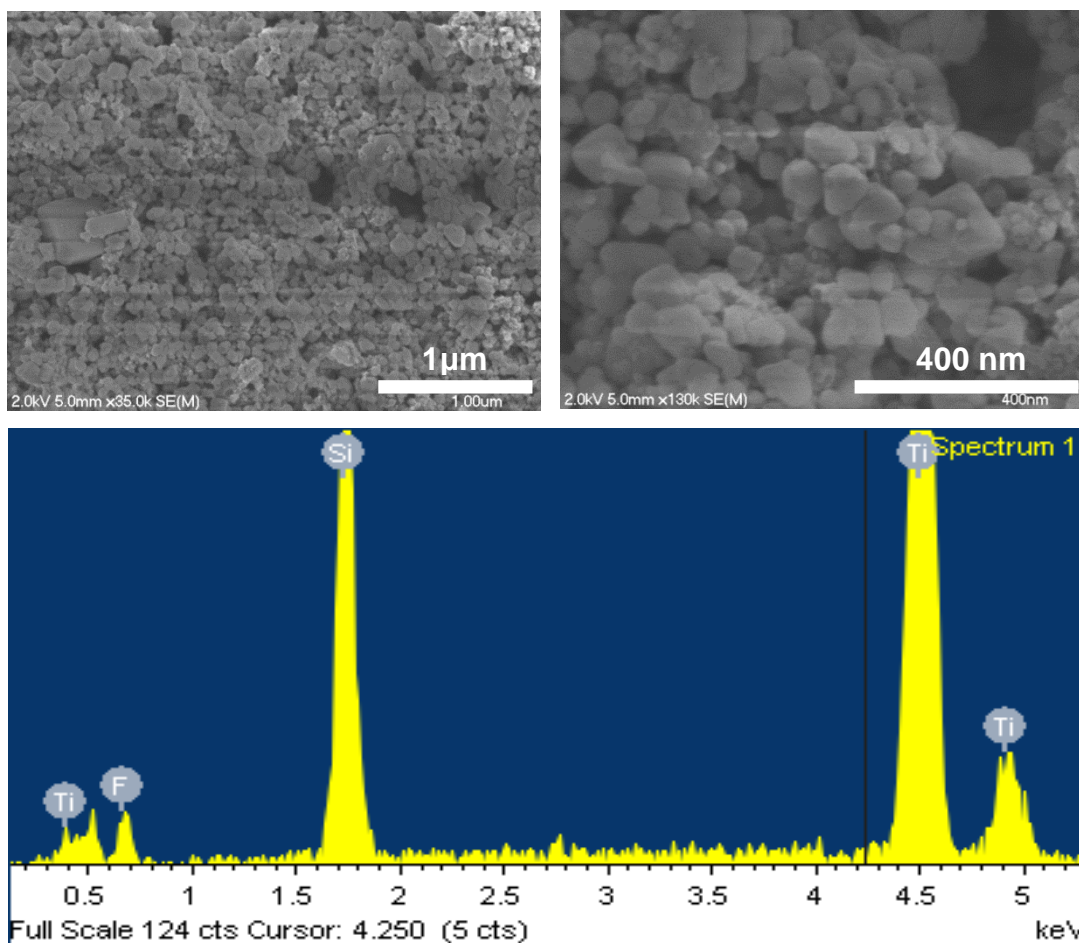


Figure 25: SEM (top) and EDS (bottom) elemental analysis of oxygen deficient ntile synthesis with titanium nanoparticle resultant

2.2.6 Structural comparison and summation of TiNTs, sTiNTs, TiNS, Ntiles and conventional anatase morphologies

In summation there are some key differences between the (001) enhanced morphologies. First being the synthesis method, the Ntiles are solvothermally synthesized by a hydrolysis reaction between titanium butoxide and 48% aqueous HF. This reaction requires the Fluorine addition to serve as a capping agent to facilitate the expression of the (001) surface. For a general synthesis the resultant material is ~83% (001) surface

and 17% (101) surface. The TiNTs are produced from a hydrothermal reaction with no capping agent and result in a material that has 100% (001)-like surface exposed. These are then mechanically processed into sTiNTs and TiNS. Due to the energy required in the physical breaking of the tubes to create the sTiNTs and TiNS there are many defects induced, and a large variety in the morphology of the final product. The morphology comparison of the materials can be seen in Figure 26.

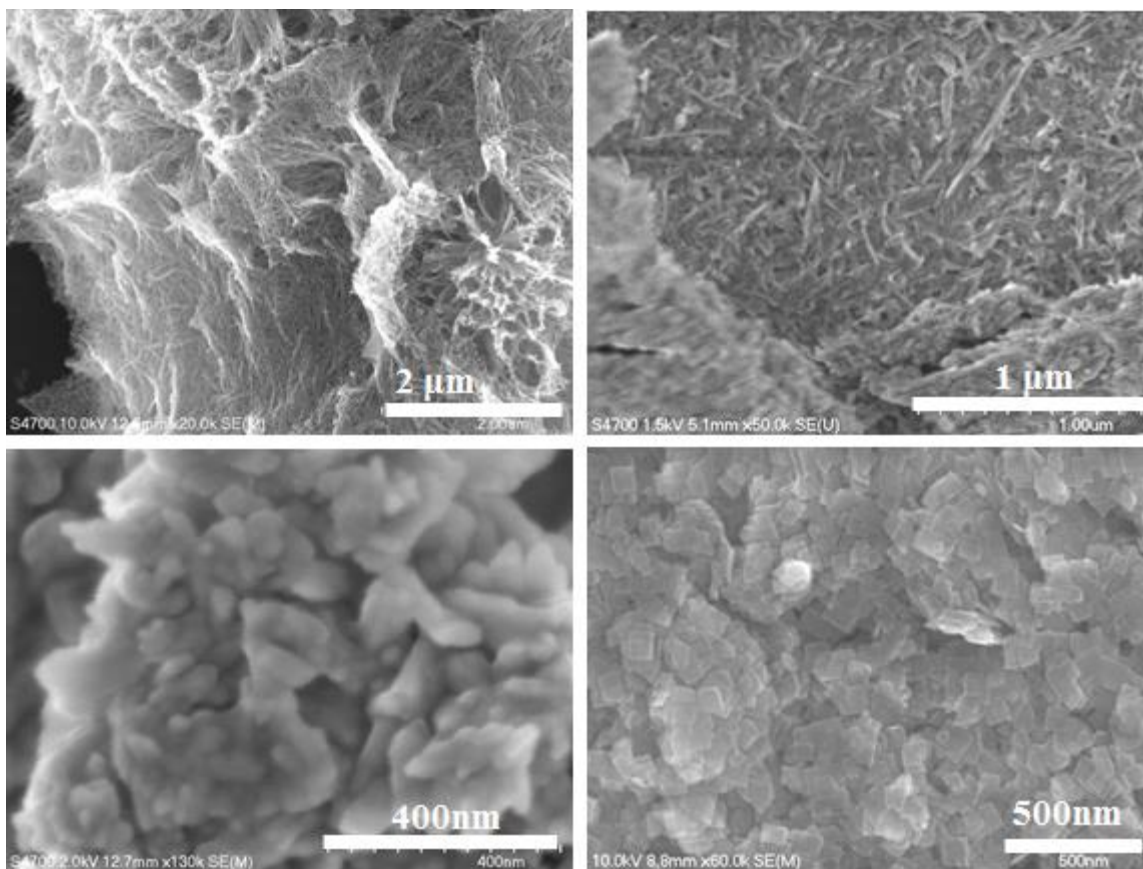


Figure 26: SEM images of as-synthesized TiNTs (top left), sTiNTs (top right), TiNSs (bottom left), and Ntiles (bottom right)

For powders of these nanomaterials the specific surface area considered is $\sim 156 \text{ m}^2/\text{g}$ for the Ntiles, and $200 \text{ m}^2/\text{g}$ for the as-synthesized TiNTs (not considering interlayer spacing as part of the surface area.) The other two morphologies were not evaluated for this

measurement due to the variant nature of the resulting material, additionally, these numbers are not needed for any of the calculations and experimentations done in this research project. Another key difference between these morphologies is that the (001) enhanced Ntiles are pure anatase phase material, whereas the TiNTs, sTiNTs, and TiNSs have an anatase (001)-like surface but an internal structure based on the previously discussed delaminated anatase model. The two commercially available references materials used are Degussa p25 which is 80% anatase with the other 20% being constituted of rutile and amorphous TiO_2 , and 32 nm Anatase. The SSA of p25 is $50 \text{ m}^2/\text{g}$ and the SSA of 32 nm anatase is $45 \text{ m}^2/\text{g}$.³⁶ The (001) materials have a significant increase in the SSA as compared to the more traditional commercially available morphologies. It is also well agreed upon that the majority (94%) of the surface of these anatase nanoparticles is the (101) surface.⁴⁶ All of the properties contribute to the functionality of the materials in solar fuel applications.

CHAPTER 3 BAND STRUCTURE OF TITANIA NANOMATERIALS

There are several properties that need to be considered to determine the viability of a semiconducting material for solar applications. One of which is the band gap of the material that is chosen. Materials that have larger band gaps such as the 3.2 eV band gap for standard bulk anatase titania will need to be derivatized with a photosensitive dye to allow for an adsorption of a larger percentage of available solar photons. The 3.2 eV band gap falls within the UV region of the solar spectrum which only accounts for about 3% of the radiation that makes it to the Earth's surface. The band gap would have to be much smaller (red shifted) to make use of the peak of the solar spectrum and allow for things like photocatalysis to happen under visible irradiation.

The additional consideration to the band gap that needs to be addressed is the energetic location of the conduction band and to a lesser extent the valence band. The open circuit voltage attained translates to the energy available to do work such as splitting water. An important factor that determines the potential value of V_{oc} is the energetic level of the conduction band. The theoretical maximum is the energetic difference between the redox couple of the electrolyte and the conduction band energy as seen in Figure 27.

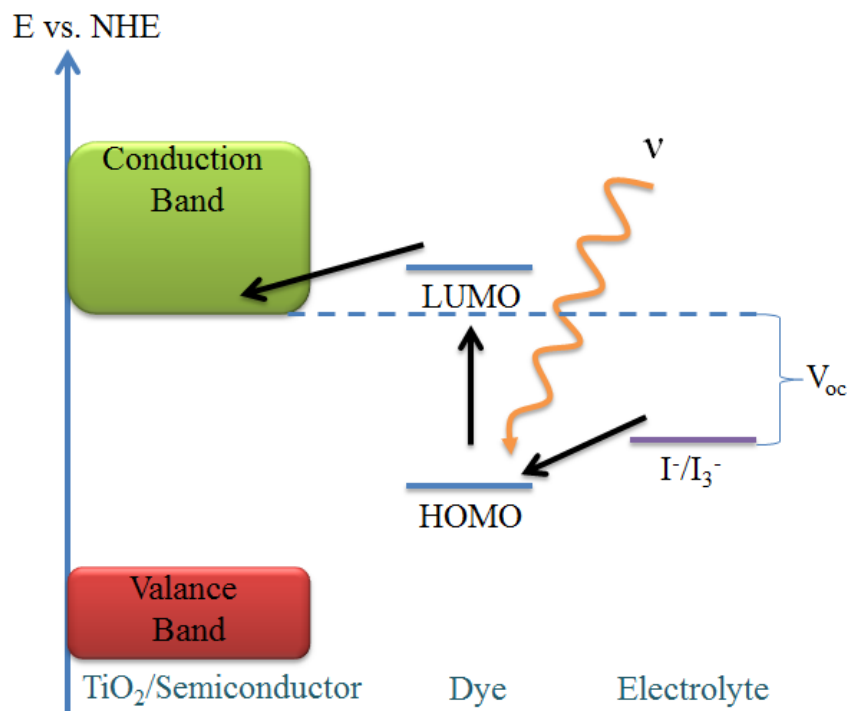


Figure 27: Energy diagram of DSSC with the black arrows representing the movement of electrons through the device.

In actual devices the V_{oc} that is measured will always be lower than the expected maximum due to losses from recombination and back electron transfer. After determining the band gap it is important to evaluate the conduction band energy of the material being explored to determine if it will be possible to attain a gain in the V_{oc} . Determining the conduction band energy for non-porous thin films is relatively straight forward and can be done with ultraviolet photoelectron spectroscopy (UPS.) This technique is powerful to determine the energy level of the conduction band in vacuum, but that number does not exactly translate over to the conduction band energy of the material in an actual DSSC. Additionally, performing UPS on porous films can be tricky due to the potential of reaching the substrate through the film. Additional methods have been developed to

determine the conduction band energy in conditions that more closely related to those employed in DSSCs and will be discussed in this chapter.

3.1 Band gap tuning via nitrogen doping

There have been extensive studies involving doping of materials such as titania to tune the band gap so that it resides more in the visible region and can absorb more sunlight. An example of this tuning for titania is by making use of nitrogen as a dopant.⁴⁷ With this modification titania can perform photocatalysis when being exposed to the visible light, and not just under UV irradiation. Though this approach appears useful at first look ultimately when incorporating doped titania into a device the doping material acts as trap states and inhibits electron transfer rates within the material which in turn translates to lower efficiencies and effectiveness.

3.1.1 Nitrogen doped TiNTs

To tune the absorbance of the TiNTs an effort was made to dope them with nitrogen. Initial attempt at doping the TiNTs with nitrogen resulted in a nitrogen doped titanate material. This doping was accomplished by mixing Guanidine Carbonate into the standard nanotube synthesis. The resulting material has a tubular structure with additional aggregates this can be seen along with the change in color that resulted from nitrogen doping in Figure 28.

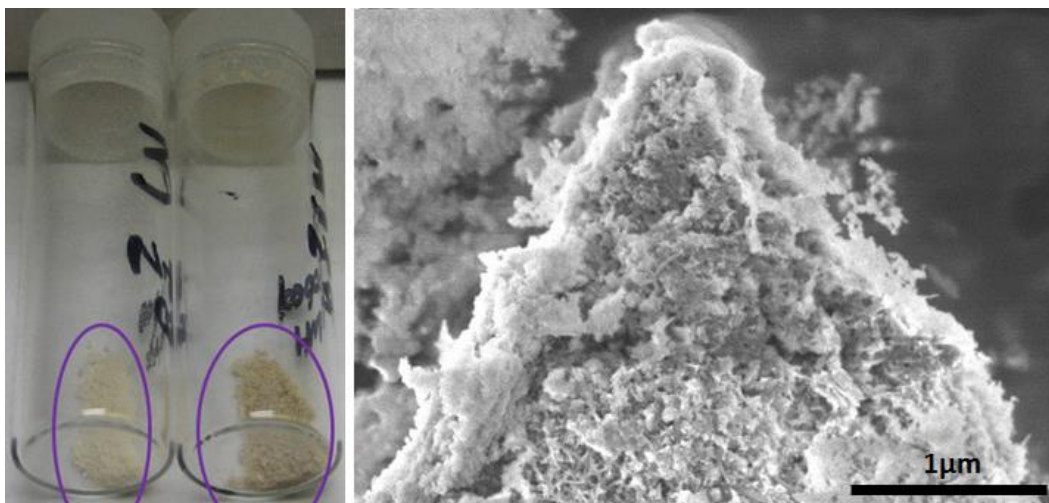


Figure 28: Photograph of nitrogen doped TiNTs, the color ranges from yellow to tan as compared to white undoped TiO_2 (left), SEM image of nitrogen doped tubes with aggregates

The aggregates that can be seen in the SEM image are most likely left over organic material from the synthesis that was unable to be removed during the washing and annealing procedure. To confirm this IR analysis was run on the dried powder post washing and annealing. Significant contributions by amine groups can be seen in the 1750 cm^{-1} to the 750 cm^{-1} region of the spectra in Figure 29 with the bending (B) and stretching (S) signals labeled. The presence of these signals is indicative that large portions of the organic material are still in the powder and not just doping of nitrogen into the structure.

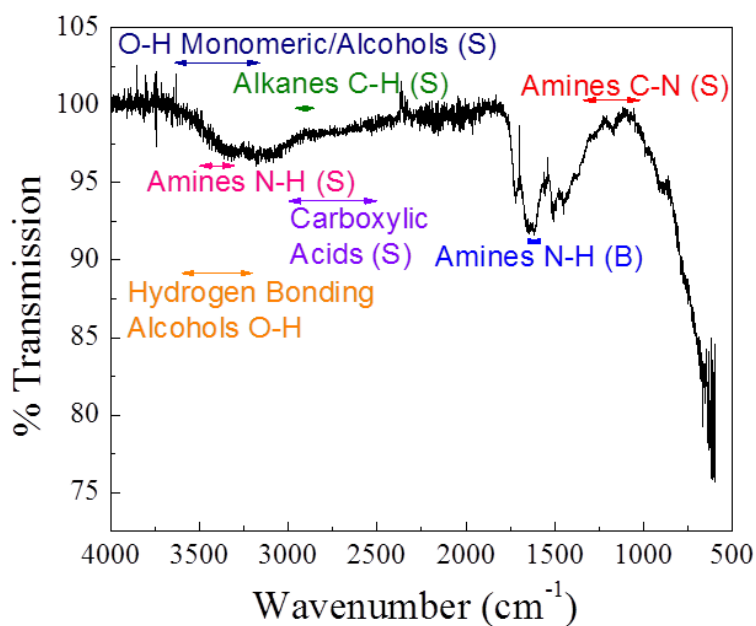


Figure 29: IR Spectra of Nitrogen Doped TiNT material with bending (B) and stretching (S) modes labeled (left)

The incorporation of nitrogen into the TiO₂ structure will decrease the band gap due to the 2p orbital in Nitrogen⁴⁸. The UV-Vis measurements on the doped material show a red-shift of the absorbance onset as compared to un-doped tubes as seen in Figure 30.

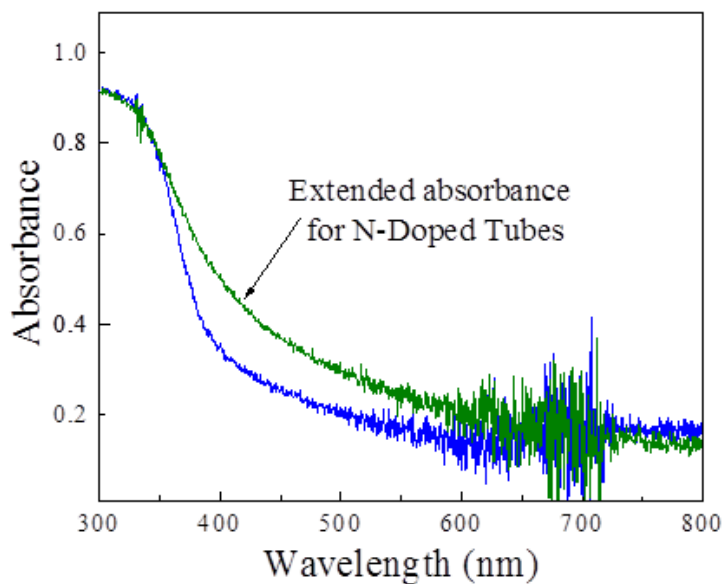


Figure 30: UV-Vis of N-doped and as-synthesized TiNTs

To determine the crystallinity of the synthesized material XRD was performed on the washed and annealed powder. A complicated spectrum resulted from the XRD analysis shown in Figure 30. To ensure that the sample aggregates were not just crystallized guanidine carbonate was modeled in Materials Studio (Figure 31) was used to simulate the XRD pattern of crystallized guanidine carbonate which is plotted in comparison to the powder spectra in Figure 32.

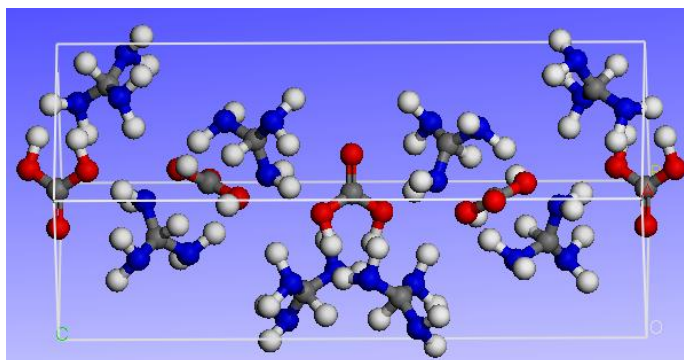


Figure 31: Materials studio model of guanidine carbonate crystal with hydrogen (white), nitrogen (blue), oxygen (red) and carbon (grey) atoms

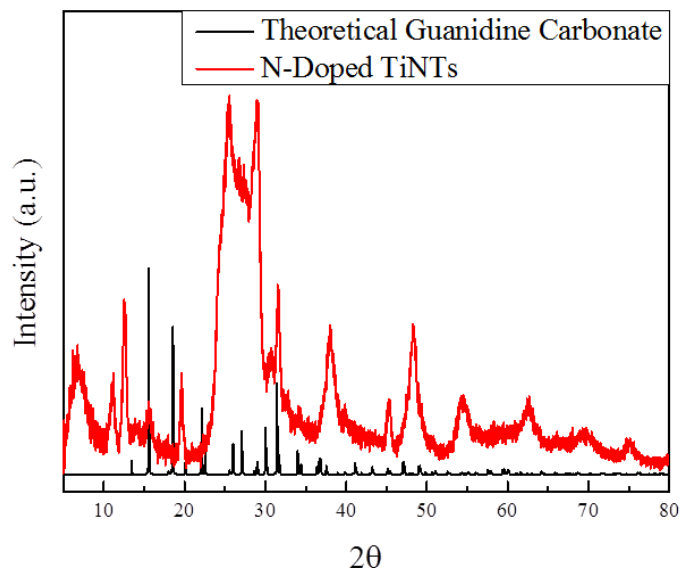


Figure 32: XRD Spectra of N-doped TiNTs (red) and theoretical calculation of crystallized Guanidine Carbonate (black)

From the presented XRD spectra it can be seen that there are peaks that correspond to crystallized guanidine carbonate, however there are additional peaks corresponding to a titanate like material. It is likely that the aggregates are excess crystallized guanidine carbonate with doped tubes underneath. XPS was also performed (not shown) to try and see the binding energy shifts associated with nitrogen being incorporated into the lattice. Because of the large amount of organics on the surface the effect of surface charging was great and even with the neutralizer the signal was not reliable enough to detect the subtle binding energy change. Due to the aggregate nature of the material they were not tested for device capability because they were unable to be incorporated into uniform films. With the knowledge that the dopant frequently acts as a trap state for electrons it is more pertinent to pursue materials with natively smaller band gaps or undoped materials that can be derivatized with a photosensitive dye.

3.2 Spectroelectrochemical Band Edge Determination

Spectroelectrochemical band edge measurements are useful when traditional conduction band energy determination is unreliable or unable to be performed. In a method first pioneered by Gratzel and Fitzmaurice infrared absorbance is monitored as a potential is being applied to a porous, nanomaterial film deposited on transparent conducting glass.⁴⁹⁻⁵³ The premise of this experiment is that once the applied potential is high enough to populate electrons into the conduction band inter-band transitions within the conduction band will be able to be seen spectroscopically as seen in the left half of Figure 33. This is achieved by a three electrode setup in an electrolyte as seen in the right half of Figure 33.

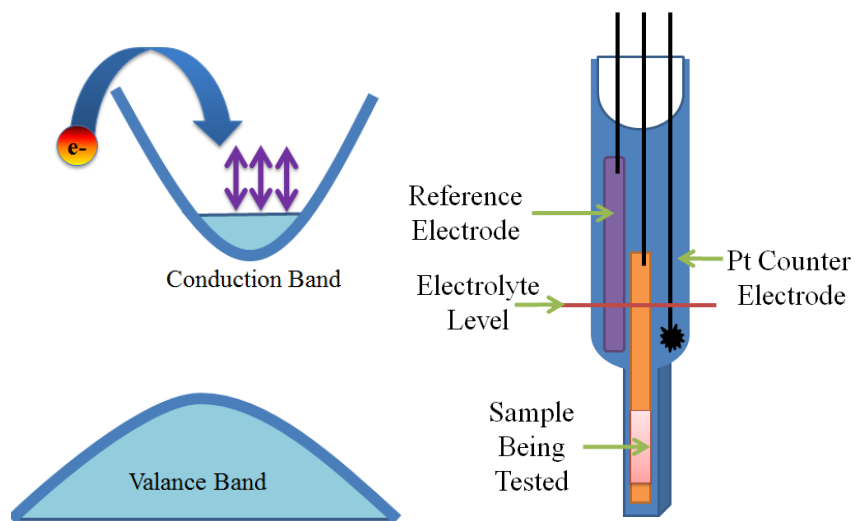


Figure 33: Representation of conduction band filling from applied potential and inter-band transitions (Left) and three electrode set up for applied potential. (Right)

The first generation set up used to achieve this this measurement involved a Pine WaveNow USB Potentiostat and a Cary 5000 UV-Vis. A modified glass cuvette was designed to allow for a larger portion to be added to the top to hold the electrodes, and

electrolyte. The top portion of the modified cuvette was fitted with a rubber stopper with wire feedthroughs to connect the electrodes to the equipment. A 1 mm diameter thin plastic tube was inserted through the rubber stopper so that the sample could be outgassed by bubbling argon. The electrodes used for this measurement were a Pt counter electrode wire, a silver chloride reference electrode, and the sample deposited on conduction transparent glass (FTO.) Special care was taken to electrically isolate the electrodes and ensure that they were not in contact. A C-V sweep was taken prior to each measurement to ensure that the electrodes were connected properly. A photo of the first generation set up can be seen in Figure 34.

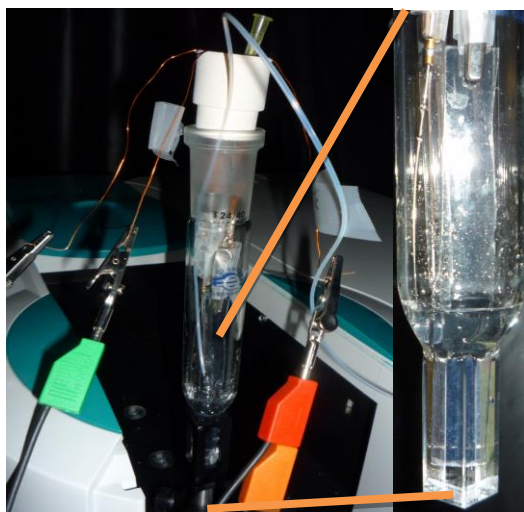


Figure 34: Modified cuvette attached to three electrode potentiostat for spectroelectrochemical band edge measurement (left) and zoomed in image of modified cuvette on the right.

The measurement is achieved by sweeping the voltage slowly from 0V to -1V or further depending on the stability of the electrolyte used. When using an aqueous electrolyte potentials need to remain lower than 1.23V the potential at which water splits. For more insulating materials the same technique can be applied but a non-aqueous

electrolyte such as acetonitrile must be employed due to its higher electrical stability. For the purpose of these studies and the materials measured aqueous electrolytes were suitable. Allowing for various pH values of the electrolyte one can confirm that the flat-band potential obeys standard Nernstian behavior. For standard nanoparticle TiO_2 this has previously been confirmed to follow the relationship $V_{fb} = 0.4 - (0.06 \cdot \text{pH})$ (V/SCE).⁴⁹

The theory behind this measurement is non-trivial and worth discussion. For a given temperature the density of electrons in the conduction band can be calculated using Fermi-Dirac statistics as shown in Equation 2⁵⁴.

$$n_{cb} = \int_{E_{cb}}^{\infty} g_{cb}(E) \frac{1}{e^{(E-E_F)/k_B T} + 1} dE$$

Equation 2: Fermi-Dirac statistic calculation for charged carrier density

Where $g_{cb}(E)$ is the density of states in the conduction band which has already been calculated and published on by Asahi et. al. as shown in Figure 35.

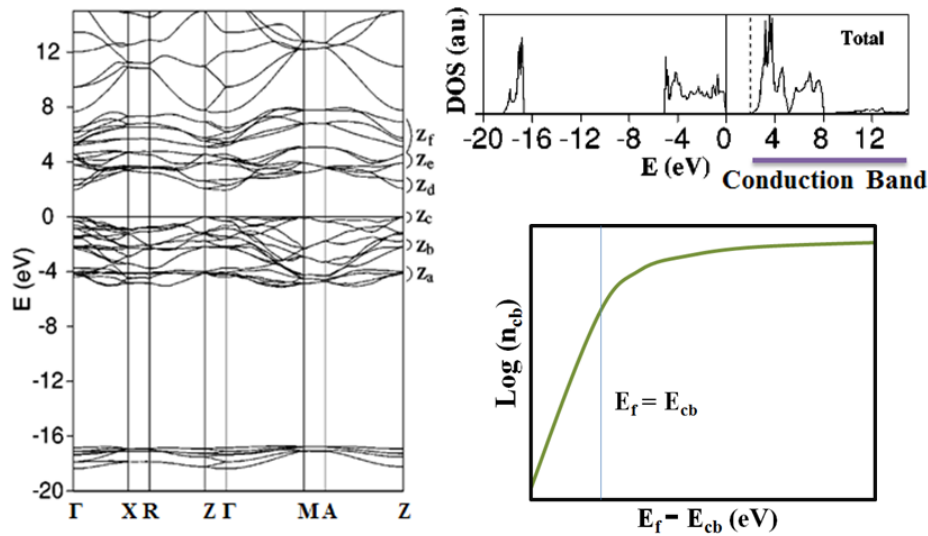


Figure 35: Band structure calculation of anatase (Left)⁵⁵ and corresponding density of states (Top Right)⁵⁵ Using this information a general form of the electron density can be shown (Bottom Right)⁴⁹

From this a number of assumptions need to be made to proceed with the calculations first is that the electrolyte semiconductor interface is relatively flat meaning that any roughness due to the nanoparticulate nature of the film is much larger than the space charge region at the surface. The reasonable assumption that the film is isotropic is also made. The potential at the semiconductor surface will depend on the amount of electrons, holes and ionized donors and acceptors. Since titania is an n-type semiconductor we can assume that the hole concentration is negligible and that any ionized donors or acceptors (material impurities) will be constant throughout the material. We can now use Poisson's equation to calculate the how the potential varies from the surface due to the conduction band electrons. From Jackson's *Classical Electrodynamics* the Poisson equation is shown in Equation 3.

$$\nabla^2 \Phi = \frac{-\rho}{\epsilon_o}$$

Equation 3: Poisson Equation

From the Poisson equation it can easily be shown by using our previously discussed quantities that the potential due to the conduction band charge density as you move away perpendicular to the surface is Equation 4.

$$\frac{d^2 \varphi}{dx^2} = \frac{q}{\epsilon \epsilon_o} [n_{cb}(\varphi(x)) - n_o]$$

Equation 4: Potential due to negative carrier population of the conduction band in TiO₂

This non-linear equation can be solved numerically to yield the change in potential between the surface (ϕ_s) and the bulk (ϕ_b) material. From this we can calculate the absorbance by first defining a function "G" the detail the change in potential between the

bulk and the surface of the material. Figure 36 shows the change in potential or excess potential equation with a rough estimate of the shape of the resulting graph⁴⁹. Depending on initial charge of the semiconductor the start and the slope of the rise will vary but the general shape will be the same.

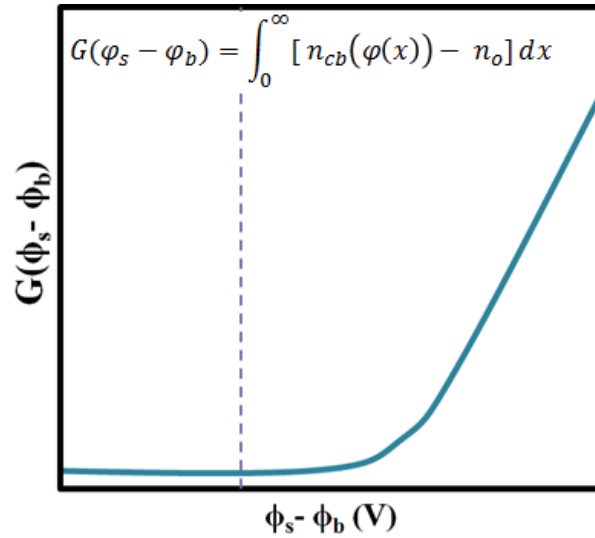


Figure 36: Equation for excess surface potential on anatase semiconductor with populated conduction band and general shape of resulting graph.

From this the shape of the resulting absorbance spectra can be attained from comparison with the Beer-Lambert Law which can loosely be defined as⁵⁶⁻⁵⁸:

$$\text{Absorbance} = (\text{Optical Cross Section}) * (\text{Path Length}) * (\# \text{ of absorbers})$$

Where the number of absorbers in this case is the populating electrons which can directly be gotten from the change in potential equation in Figure 36. So what this simplifies to is that the change in absorbance of the material is directly proportional to the change in the potential. Once the electrons have enough energy to be deposited into the conduction band the absorbance increase should proceed linearly.

This experimental set up allows for a relatively straight forward determination of the conduction band energy for porous semi-conducting films in various electrolytes and at differing pH values. Unless otherwise noted, all of the experiments were performed in pH=1 Perchloric Acid (HClO_4) and all potentials were attained using a Ag/AgCl electrode. This experiment was performed on a number of materials for the Energy Frontier Research Center (EFRC) at UNC such as tantalum doped titania nanowires from the McNeil group which showed to have a conduction band energy of -0.61V, nano-printed niobium oxide from the Samulski Group showed a conduction band value of -0.47V. Additionally, sol-gel zirconium oxide from the Meyer Group was also tested and the band edge was found to be above -0.8V and further non-aqueous tests were required to make sure of electrolytes with a higher break down potential. As they were not part of this project they will not be discussed here.

All the synthesized titania materials were analyzed to determine if there was an enhancement of the conduction band. The (001) surface has been predicted to have a higher conduction band energy due to band bending at the solid liquid interface.⁵⁹ Additionally the band gap of the sTiNTs and TiNS is much higher than the band gap of 3.2 eV of standard anatase as discussed previously. This could translate to either an increase in the conduction band energy, a decrease in the valance band energy, or a combination of the two. From the spectroelectrochemical measurement it can be seen that the band edge in 0.1 M pH 1 HClO_4 for a standard nanoparticle film is -0.61 V (vs. Ag/AgCl) and the tubes offer a 30 mV enhancement of the conduction band energy and tiles offer a 35 mV enhancement of the conduction band energy, and the sheets offer a 50 mV enhancement of the conduction band energy as can be seen in Figure 37.

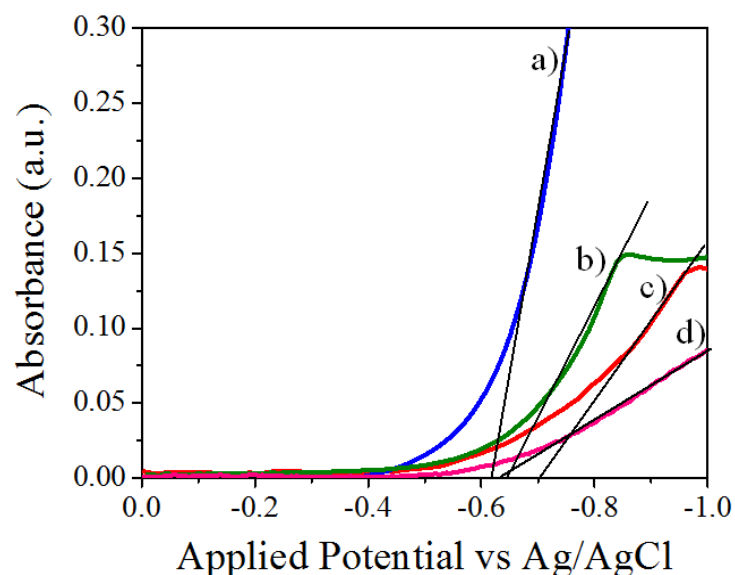


Figure 37: Spectroelectrochemical measurement of band edge in .1M pH1 HClO₄ for a) standard np film, b) Ntile film c) TiNS film and d) sTiNT film

An explanation for the trend that is seen in the spectroelectrochemical measurement is that the band gap of the tubes and sheets is larger than that of standard anatase. Additionally since the tubes and sheets are produced hydrothermally and not able to undergo a healing anneal there are several residual defects on the surface that will lower the maximum band edge that is able to be measured.

3.3 Band Gap Measurements of Nanomaterial Titania

Additionally, UV-Vis can also be employed to determine the band gap of a material. Nanomaterials are deposited on a quartz slide. Glass cannot be used for this purpose since it has an absorbance in the UV range and will obscure the data from the material and a quartz substrate is used instead. For a material that is a semiconductor the band gap can be attained from Equation 5⁶⁰:

$$\alpha = A(h\nu - E_g)^n$$

Equation 5: Optical absorption band gap equation

Where α is the absorption, ν is the frequency of the light, A is an arbitrary constant, h is plank's constant and E_g is the band gap. The value of “n” is “½” for a direct gap semiconductor and “2” for an indirect gap semiconductor. Unlike rutile which has a direct gap, anatase is an indirect band gap material and thus for all of the necessary fittings shown here $n=2$. It can be seen that the (001) enhanced ntiles have a band gap of 3.2 eV which is the same as nanocrystalline anatase. The sTiNts have a larger band gap of ~3.6 eV and the TiNS have the largest band gap of ~3.9 eV. The band gap measurements for the three materials can be seen in Figure 38. The higher absorbance values that can be seen in the ntile sample are due to the larger particle size of the tiles which translates to more scattering within the film. The enhancement of the band gap seen in the nanosheets films can be explained by exciton trapping. This enhancement arises by size quantization due to how thin the nanosheets are (at most a few layers.)

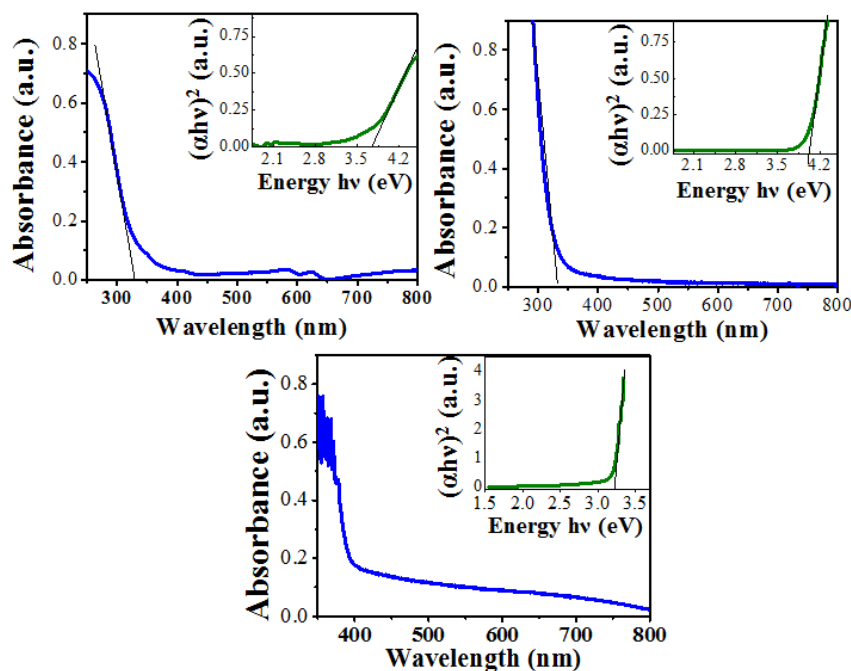


Figure 38: UV-Vis band gap analysis: absorbance curve is blue and inset is band gap transform for sTiNTs (top left) TiNS (top right) and Ntiles (bottom center)

3.4 Trap State Analysis of (001) Enhanced Nanotiles

Trap states within a semiconducting material can greatly affect its behavior. Specific to the applications discussed in this dissertation trap states can greatly affect electron charge transfer which will ultimately reduce the overall efficiency of a device. For analysis of new semiconducting materials it is important to understand the level of trap states that are within the material. This can be qualitatively be done by careful analysis of cyclic voltammetry measurements (CV) on a film. On the CV mono-energetic deep trap states can be seen by the presence of a small reduction wave at a potential below the conduction band energy which was previously measured. Additionally the trap state density is dependent upon the pH of the electrolyte that the film is immersed in. This is indicative that the trap states that are seen on the CV are on

the surface of the material otherwise trap state density would not change with variations in pH.⁶¹

CV measurements presented here were carried out 0.1 M HClO₄ electrolyte solution for films deposited on FTO. A CHI601D potentiostat was used for the measurement and potential was swept from 0 V to -1V and back to 0 V at a scan rate of 0.1 (V/s) with potential sample intervals of 0.001 V. The instrument sensitivity is 0.001 A/V.

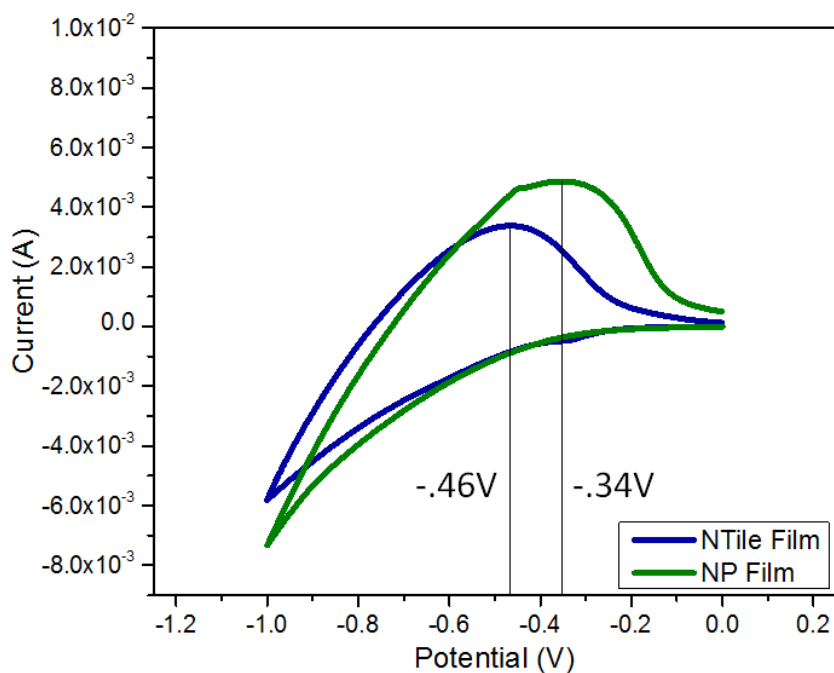


Figure 39: CV of Ntile and NP film in 0.1M HClO₄

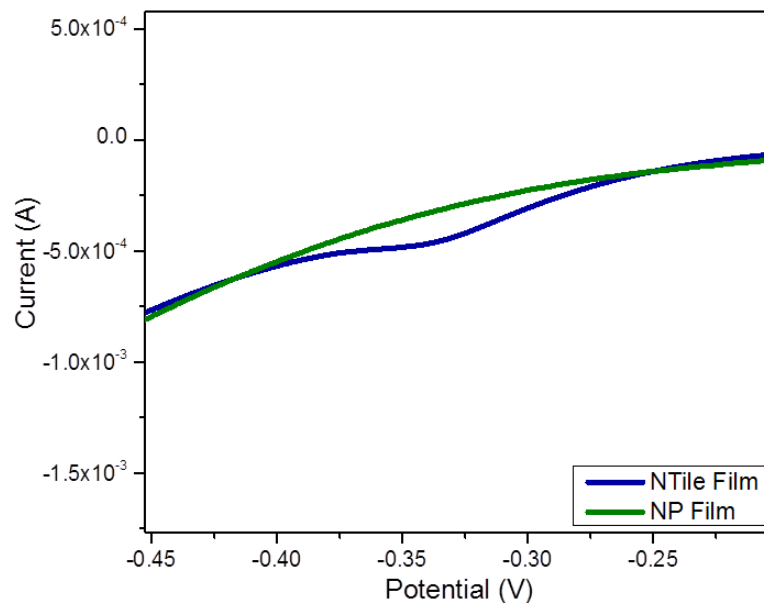


Figure 40: Zoomed-in CV of Ntile and NP film in 0.1M HClO₄ from Figure 39

As can be seen in the zoomed in portion of the C-V in Figure 40 a very small reduction wave is seen on the ntile film. This can qualitatively be discussed as an increase in trap states on the ntile film as compared to a standard NP film. Over C-V measurement on several films this reduction wave will get smaller and disappear indicating that the amount of trap states depend on the quality of the film and are not an inherent problem of the ntile material.

CHAPTER 4 DYE SENSITIZED SOLAR CELL DEVICE DEVELOPMENT AND ELECTRICAL CHARACTERIZATION

After synthesis and characterization the first step to determine viability of any new nanomaterial for solar fuel applications is to test the device potential in a dye sensitized solar cell. A material that performs well in a DSSC and exhibits dye binding stability should then be suitable for DSPEC testing. For a nanomaterial to be incorporated into a DSSC it needs to be able to create a stable film on a transparent conducting electrode. Depending on the material film processing can range from straight forward to troublesome. All of the nanomaterials that have been discussed thus far are able to be incorporated in a stable film and thus a DSSC.

4.1 Film Preparation of Nanomaterial Anatase

Each material studied required an alternate procedure for film deposition ranging from standard drip casting, modified Langmuir–Blodgett, paste formation, doctor-blading, or spin coating. Each materials film preparation will be detailed individually in addition to the reasoning for such deposition techniques. Once a stable deposition technique is developed the substrate that the films are deposited on will vary depending on the intended application of the film. All glass and fluorine doped tin-oxide coated (FTO) glass slides were cleaned in the same manner. Substrates were cut to desired size with a glass cutter then places in a 0.1 M HCl solution and sonicated for 30 minutes,

afterwards the top solution was poured off, replaced with Ethanol, and sonicated for an additional 30 minutes. Lastly the top solution was poured off and replaced with acetone for a final 30 minute sonication. After the sonication cleaned films were either removed from the acetone and dried with a nitrogen gun for immediate use or stored in a fresh 50mL centrifuge tube of acetone. For photophysical experiments, cleaned microscope glass slides were cut into 1 cm x 5 cm slabs and used as substrates. For band gap measurements of sTiNTs and TiNS with UV-vis, a quartz slide was used as a substrate so that absorption from a glass substrate does not interfere with intrinsic absorbance of the nanotubes. Incident photon-to-current conversion efficiency (IPCE) measurements, transient absorbance measurements, and band edge measurements used a substrate of FTO glass cut into 1 cm x 5 cm slabs.

4.1.1 Nanotube and Nanosheet Film Preparation

Due to the hydroxyl termination on the surface of the nanotubes and nanosheets the outside of the particles is negatively charged. This leads to a steric repulsion between the particles when they are in water and thus allows them to create a stable suspension. The ability for a metal-oxide nanomaterial to form a stable suspension in water, as in the case of shortened tubes and sheets, is very unique. A picture of this suspension can be seen in Figure 41.



Figure 41: Suspension of Shortened Nanotubes

Materials that form stable aqueous suspensions lend themselves to film incorporation via drip casting. Deposition areas on clean substrates were masked off with Kapton® Polyimide high temperature tape with an approximate thickness of 30 μm . Suspensions of either shortened nanotubes or nanosheets were dripped on to the desired surface and allowed to dry in a standard box oven in atmosphere at 50 $^{\circ}\text{C}$. Subsequent depositions were implemented after the film was allowed to fully dry until the desired thickness and surface coverage was achieved. This method results in a thin 1-3 μm highly porous film as shown in Figure 42.

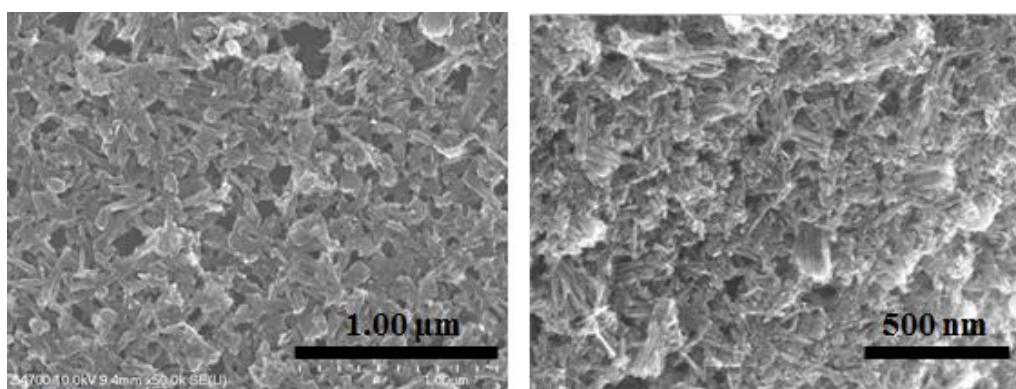


Figure 42: SEM Images of drip cast TiNS film (left) and sTiNT film (right)

In an effort to increase film density and interconnectivity between particles a modified Langmuir–Blodgett type deposition was employed in an attempt to align the nanotubes.

This was attained by placing a clean substrate in a glass beaker with nanotube suspension and allowing it to slowly evaporate at 25 °C over the course of 10-14 days. The slow decline in height of the water air interface serves to partially align the tubes as the water evaporates and the liquid gas interface decreases in height. This method was unable to yield films that had a thick enough film for device testing however it did prove the concept as shown in Figure 43.

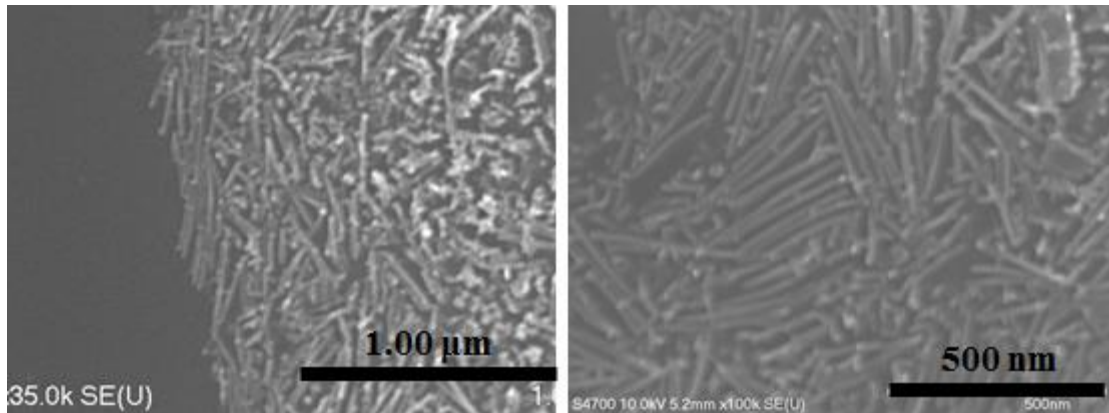


Figure 43: Partially Aligned sTiNTs

After after standard drip-cast deposition both sTiNT films and TiNS films were annealed in a high-temperature box furnace at 300 °C to finish their preparation. As previously mentioned higher temperature anneals (>325 °C) will cause the structure to collapse. Additional films were prepared with higher temperature anneals to evaluate device performance and will be discussed in that context later.

4.1.2 Nanotile Film Preparation

The Ntiles film preparation requires more care than the sTiNTs and TiNS films. On their own the ntiles do not produce a stable suspension so they are not able to be drip

cast into a film. Several methods were used in attempts to create a stable film. There were several complications that were addressed in order to facilitate film stability. Initial attempts to incorporate the ntiles into a film without any binder resulted in unstable films. The reason for this instability stems from the anatase forming aggregates with itself that are more stable than the adhesion to the glass. When the solvent evaporates from the glass the ntiles will stick to themselves and peel off resulting in an unstable film that is not suitable for any device measurements as shown in Figure 44.

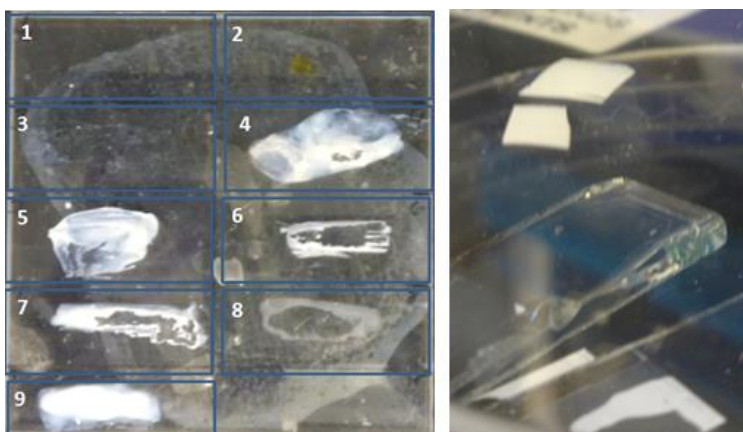


Figure 44: Unstable Ntile films deposited on glass and FTO specific batch numbers are labeled on the left

In order to create a film that will remain stable upon drying the density/porosity of the film needs to be decreased so that there will be more flexibility in the film when it dries. This can be achieved in a number of ways the first of which is using a 1:1 tert-butanol and water mixture to suspend the nanotiles before deposition. The tert-butanol serves two purposes the first being that it has a melting temperature of $\sim 25^{\circ}\text{C}$ which when mixed with deionized water and the nanotubes creates a mixture with a paste consistency, secondly it acts as a glue between the tiles and upon the addition of heat the organic material burns off with water forming an oxygen bond between the tiles⁶². Both of these

characteristics can be seen in Figure 45. The paste was created by adding 90 mg of ntiles to 1 mL of the 1:1 mixture of tert-butanol and water. The film created from this method stably adhered to the glass substrate however it was not uniform enough for device considerations to alternate methods needed to be explored.

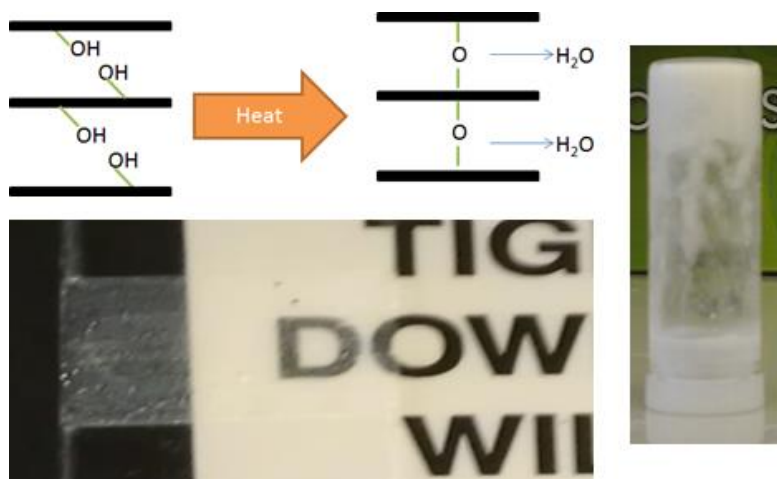


Figure 45: Tert-Butanol ntile films: binding mechanism (top left) 1:1 tert-butanol water ntile mixture paste (right) and film deposited from paste (bottom left)

A stable uniform film was finally achieved by creating a paste with an organic binder. The procedure for developing this paste was to incorporate 600 mg of centrifuged ntile paste (with the top solution poured off) with 1.2 mL of deionized water in a small glass vial. The mixture was then sonicated with an ultrasonic-bull horn for 45 seconds to break up any aggregates of ntiles. After sonication 0.12 mL of acetyl-acetone was added to ensure that the ntile suspension would remain stable to be deposited uniformly in a film. Once a uniform suspension was created 0.3 mL of 4% wt aqueous solution of hydroxypropyl cellulose (MW 100,000), and finally 0.3mL of 10% vol aqueous triton X-100 was added. The vial was closed and shaken vigorously to incorporate all the materials and allowed to sit for 30 minutes before deposition to ensure that all the materials were at equilibrium. The paste remained uniform for several weeks and was

stirred to ensure homogeneity before deposition. The purpose of adding hydroxypropyl cellulose is to increase the porosity of the film and thus reduce its density so that the film will be able to adhere stably to the glass upon drying. Triton X-100 is a detergent that allows for the paste to be smoothly deposited on the substrate. With this paste two methods can be employed to create films. A thin film can be created by spin coating 50 μL of paste onto a 1 cm^2 area of glass or FTO substrate at a speed of 1000 rpms for 60 seconds. The thickness of these films were measured with a profilometer to be 0.6 μm +/- 0.1 μm . These films were used for UV-Vis and nanosecond transient absorbance measurements and any other measurements where optical transparency was paramount. Additional films were made using a doctor-blade technique which resulted in slightly thicker films of 1.1 μm +/- 0.1 μm . Two strips of Kapton® Polyimide high temperature tape were placed parallel 0.5 cm apart towards one end of the glass substrate. With a pipette 50 μL of the paste was deposited in the area between the tape strips and a teflon coated stirring rod was dragged across the area to create a uniform film. The film was allowed to dry in an oven at 50 °C until it was dry and then the tape was removed and the film was annealed in a high temperature box oven at 475 °C for one hour to remove any residual fluorine and burn off the organic binder. The resulting film was milky in color and very uniform. These films were used for I-V and induced current to photon measurements. An example of these films can be seen in Figure 46.



Figure 46: Doctor-blade Ntile Film Picture

4.2 Film and device considerations and constituents

The sTiNTs, TiNS and niles could all be incorporated into films that could be used for DSSC testing and electrical characterization for these measurements two different dyes were used. The two linker groups for dye attachment were the phosphonate group and the carboxyl group.

4.2.1 Dyes

The two dyes that were used are the commercially available N719 [Di-tetrabutylammonium,cis-bis(isothiocyanato)bis(2,2'-bipyridyl-4,4'-dicarboxylato)ruthenium(II)] which has been well studied in literature. N719 attaches to the anatase surface via carboxyl linkers which are better for electron transport in device measurements but not stable in $> 1\text{pH}$ and thus not suitable for water splitting applications. The second dye is one that is created in-house by the Meyer group at UNC $[\text{Ru}^{\text{II}}(\text{bpy})_2(4,4'-(\text{PO}_3\text{H}_2)_2(\text{bpy}))]\text{Cl}_2$ (bpy = 4,4'-bipyridine) and shall be referred to as RuP from this point forward. The steps involved in the synthesis of *cis*- $[\text{Ru}(\text{bpy})_2\text{Cl}_2]$ is by reaction of 2,2'-bipyridine with dichlororuthenium(II) cyclooctadiene polymer in 1,2-dichlorobenzene followed by reaction of *cis*- $[\text{Ru}(\text{bpy})_2\text{Cl}_2]$ with 4,4'-bis(diethyl phosphonate)-2,2'-bipyridine. With this method, *cis*- $[\text{Ru}(\text{bpy})_2\text{Cl}_2]$ is obtained free of $[\text{Ru}(\text{bpy})_3]^{2+}$ and the latter is not carried along to the next step. Hydrolysis of the ester groups was accomplished by refluxing in 4 M HCl for 48 hours. The hydrolyzed complex was purified by column chromatography on Sephadex LH-20 using water as the eluent. Yield: 80%. ^1H NMR (400 MHz, D_2O): δ 8.75 (d, 2H), 8.51 (d, 4H), 8.03 (t, 4H), 7.91 (m, 2H), 7.79 (dd, 4H), 7.55 (dd, 2H), 7.35 (t, 4H). ^{31}P NMR (400 MHz, D_2O): δ 6.78.

RuP attaches to the surface of anatase via phosphonate linkers which have a lower electron transport efficiency but are more stable to the anatase surface over a broader pH range however this is still limited to pH values of <5 .³⁵ Measurements done by my colleagues in the EFRC have shown that the efficiency of the RuP dye for induced photon to current efficiencies is approximately 10% of the efficiency found by the same surface derivatized with N719 instead. The advantage of using the phosphonated dye is to allow for water splitting applications.

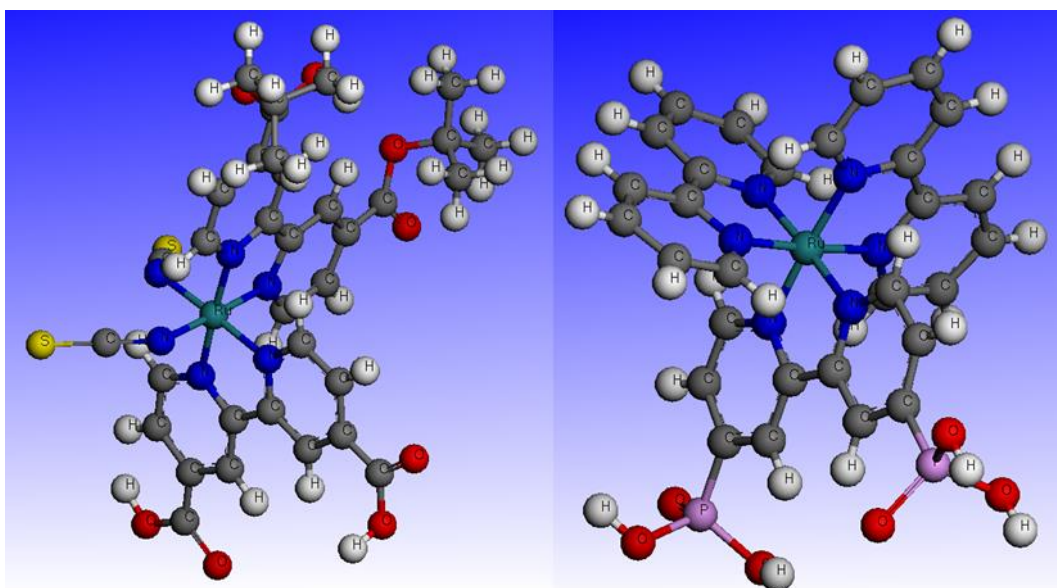


Figure 47: Materials Studio rendering of N719 dye (left) and RuP dye (right)

4.2.2 Device Design

The first “high” efficiency dye sensitized solar cell was developed By Michael Gratzel and Brian O’Regan shortly before being published in *Nature* in 1991. The now relatively simplistic design was revolutionary and changed the course of solar cell development.³⁰ The widely accepted design is a transparent conducting electrode with nano-sized TiO_2 deposited on it. This film is then derivatized with a photosensitive dye

and sandwiched together with platinum coated counter electrode by a surlyn spacer and injected with an I/I^{-3} electrolyte. Unless otherwise noted the electrolyte that was used to characterize the following devices is a solvent of dry acetonitrile with 0.1M LiI, 0.05 M I_2 , 0.5 M 1,2-dimethyl-3-propylimidazolium iodide, 0.5 M tert-butylpyridine, 0.1 M guanidinium thiocyanate. Sample devices are shown in Figure 48.

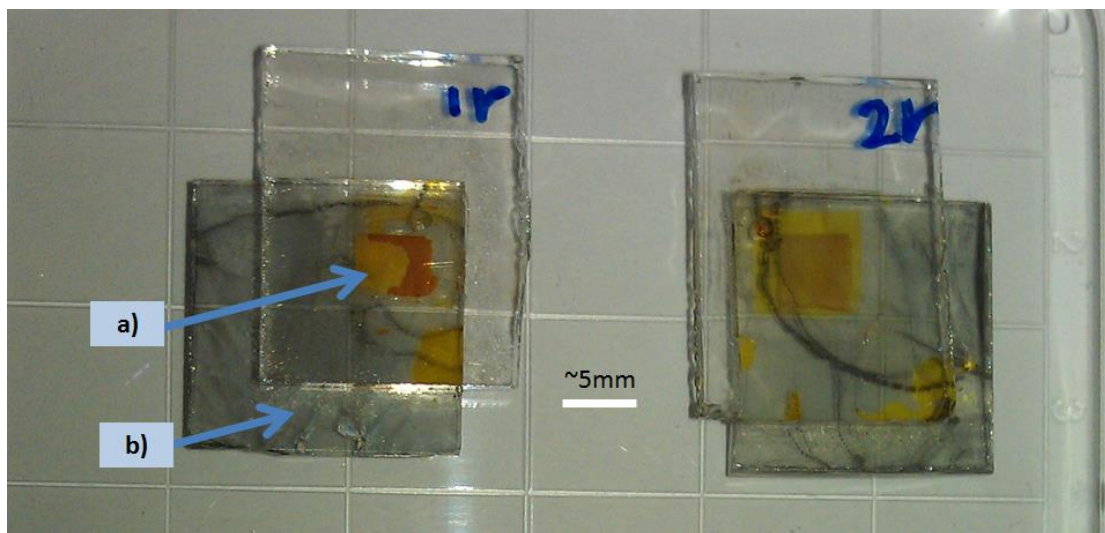


Figure 48: DSSC devices a) active area and b) Pt coated counter electrode

4.3 Film Characterization Transient Absorbance and Dye Loading

Transient absorption measurements are a powerful tool for evaluating injection efficiency, and estimating back electron transfer rates for derivatized films. The measurement monitors the absorbance spectra at a specific wavelength over time of the excited state from a recently excited chromophore.

4.3.1 Nanosecond Transient Absorbance Experimental and Equipment Specifications

Nanosecond laser pulses from a Spectra-Physics Lab 170-10 Nd:YAG laser & VersaScan/240/ULD OPO combination served as an excitation source (532 nm, 5-7 ns, 10 Hz, 4 mJ/pulse) directed into a commercial laser flash photolysis instrument (Edinburgh LP920) equipped with a 450 W pulsed Xe probe source. Operating at 1 Hz, transient absorption kinetics were measured with a sensitivity of 1 mOD probing at 400 nm. Single wavelength absorbance-time traces were the averages of 200 laser shots. Ru-derivatized electrodes were placed diagonally into a 10 mm cuvette filled with solvent or electrolyte solution. Electrolyte solution was 0.1 M HClO₄ unless otherwise noted. The top of the cuvette was modified with an o-ring joint and Kontes valve such that all samples were atmosphere isolated and Argon degassed for at least 45 minutes just prior to TA experiments.

4.3.2 Nanosecond Transient Absorbance Measurements: Injection efficiency & Back Electron Transfer Rates.

Transient absorption (TA) measurements on metal oxide-bound Ru(bpy) complexes have provided invaluable insight into injection and back electron transfer dynamics.⁶³ These measurements have illustrated the importance of both high electron injection efficiencies and slow back electron transfer as prerequisites for efficient device performance.^{64,65} Both measurements were undertaken for RuP on sTiNTs, TiNS and NP TiO₂ in 0.1 M HClO₄. Absorption-time kinetic traces were obtained at a ground/excited state isosbestic point for RuP at 400 nm following 532 nm excitation.

Electron injection yields (Φ_{inj}) were measured by the use of thin film actinometry⁶⁶ with RuP on TiO₂ in 0.1 M HClO₄ ($\Phi_{inj}=1$) as the reference.^{35,67} The derivatized sTiNTs

and TiNS films exhibited significantly decreased injection yields ($\Phi_{\text{inj}} = 0.07(5) \pm 0.05$) compared to the reference as seen in Figure 49.

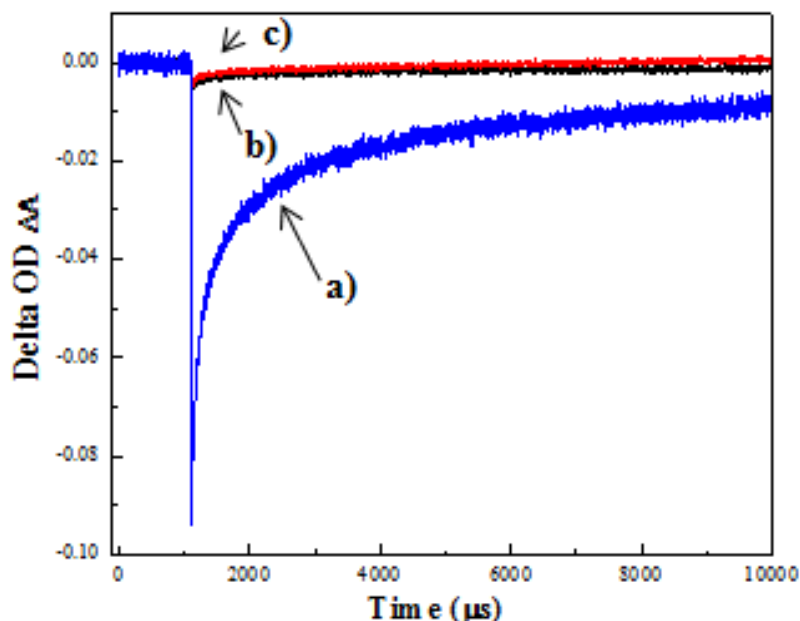


Figure 49: Nanosecond transience absorbance of RuP derivatized a) Standard NP Film, b) sTiNT Film, c) TiNT Film

The reported injection yields are based on transient absorption measurements limited to ~ 10 ns by instrument response. Emission on these surfaces is essentially completely quenched suggesting efficient injection. Most likely this reduction in injection is due to trap states facilitating back electron transfer and the enhanced conduction band energy being elevated. This would translate to electrons being injected into inter-band states and not the conduction band. An alternate interpretation of the data is that injection is efficient but that there is a significant back electron transfer component on the timescale of the instrument response function. Back electron transfer dynamics by analysis of absorption-time traces from the TA measurements data could be fit to the tri-exponential

function, but due to the low injection into sTINTs and TiNS accurate fits for electron lifetime were unreliable.

Ntile films were also evaluated with nanosecond transience absorbance. It can be seen that there is a state that has a slower decay in the ntile film as compared to the standard nanoparticle film.

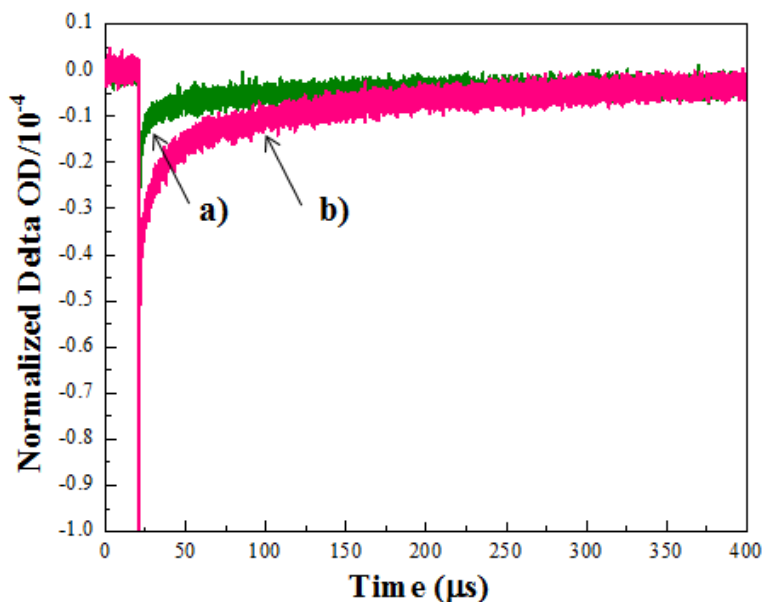


Figure 50: Nanosecond transience absorbance of TiO₂ derivatized with RuP a) Standard NP film b) ntile film max signal for both have been normalized to 1 for ease of comparison

Back electron transfer dynamics by analysis of absorption-time traces from the TA measurements data can be fit to the tri-exponential function in the method previously reported.⁶⁸ From the non-physical tri-exponential fit (Equation 6) the state lifetimes (Equation 7), and average lifetime (Equation 8) can be extrapolated.

$$k_{obs} = A_1e^{-k_1t} + A_2e^{-k_2t} + A_3e^{-k_3t}$$

Equation 6: Observed decay rate tri-exponential fit

$$\tau_i = 1/k_i \text{ (lifetime)}$$

Equation 7: Lifetime of state

$$\langle \tau \rangle = \sum A_i \tau_i^2 / \sum A_i \tau \text{ (average lifetime)}$$

Equation 8: Average lifetime

The results of this fit are shown in Table 4.

Constant	Nanotiles	Nanoparticles
A ₁	0.434	0.675
A ₂	0.217	0.126
A ₃	0.14	0.061
k ₁	1.314	6.067
k ₂	0.062	0.123
k ₃	0.004	0.002
Largest contribution to Lifetime (ns) (τ _i)	761	165
Average Lifetime (ns) (<τ>)	198	376

Table 4: Tri-Exponential fit parameters for ns transience absorbance of ntile and standard NP films derivatized with RuP

The longest state lifetime for the ntiles is 761 ns whereas the longest state lifetime for the NPs is 165 ns, however the average lifetime (<τ>) for the ntiles and NPs is 198 ns and 376 ns respectively. To further elucidate the trend seen the time for the signal to decay 50% and 75% was also evaluated for both samples. For half of the signal to decay takes 20.5 μs for the NP film and 21.5 μs for the ntile film, however this trend is further exacerbated when you look at the time it takes for 75% of the signal to decay which takes 21.5 μs for the NP film but 30 μs for the ntile film. So it becomes clear that there is most likely retardation in the back electron transfer for the ntile film as seen in a zoomed in version of the first 40 μs in Figure 51.

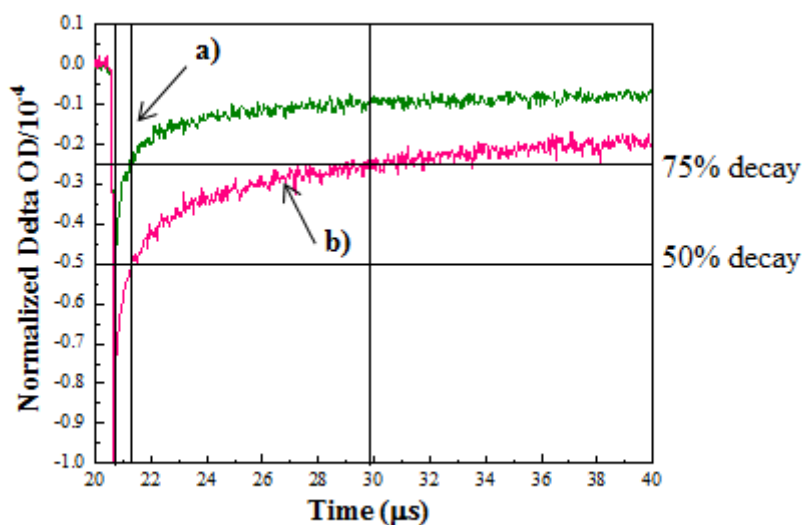


Figure 51: First 40 μs of ns TA with lines labeling 50% and 75% decay of signal for RuP derivatized TiO_2 a) Standard NP film and b) Ntile film

The slower decay that is seen in the absorption-time traces of the ntiles is most likely due to the lower amount of defects on the crystalline (001) surface than the standard TiO_2 NPs. Improvement of film density and surface area of the (001) ntiles would allow for higher dye uptake and allow for injection yield experimentation. Electron injection yields (Φ_{inj}) could not be evaluated due to the large amount of scattering in the film.

Of the three (001) enhanced anatase samples analyzed with nsTA the ntiles by far performed the best even showing a marked retardation of the signal decay supporting that the back electron transfer rates for the ntiles are an improvement over even the standard nanoparticles.

4.4 Device Characterization: I-V, IPCE and Impedance Spectroscopy

All three of the (001) enhanced samples were evaluated for device performance. The important measurements that allude to final DSPEC capabilities are the open circuit voltage and the IPCE. The Voc is important because it is a direct measure of the energy available to split water. To split water without any external bias would require 1.23 V, at this point in time the highest Voc attained with a TiO₂ nanomaterial DSSC is 0.8V. Additionally the induced photon to current measurement is important to determine how well the dye is injecting into the semiconductor and that electron is traveling around the circuit. If both of these numbers are favorable then the devices can proceed for further testing. For these measurements the sTiNT and TiNS films were evaluated with RuP dye and the ntile film was evaluated with N719. The choice of these dyes was due to availability at the time of the measurement.

4.4.1 IPCE, I-V and Impedance Spectroscopy Experimental and Equipment Specifications

Incident Photon to Current Efficiency measurements were conducted by using monochromatic light (Oriel Cornerstone 260 / Oriel Photomax housed 75W Xenon lamp combination) with a bandwidth of 10 nm. A Keithley 6517A electrometer was used to measure the photocurrent while photon flux was monitored with a UDT S370 optometer and UDT 260 detector. IPCE spectra were collected between 360 nm and 600 nm every 10 nm by using RuP-derivatized photoanodes and a platinized FTO counter electrode. IPCE measurements were carried out in dry acetonitrile solutions with 0.1 M LiI, 0.05 M

I₂, 0.5 M 1,2-dimethyl-3-propylimidazolium iodide, 0.5 M tert-butylpyridine, 0.1 M guanidinium thiocyanate.

I-V data were collected by using the 1 sun output from a Newport solar simulator equipped with AM 1.5 Global filter and 1 kW Xenon lamp. A Keithley 2400 sourcemeter was used to apply a potential and measure current. I-V measurements were carried out in dry acetonitrile solutions with 0.1 M LiI, 0.05 M I₂, 0.5 M 1,2-dimethyl-3-propylimidazolium iodide, 0.5 M tert-butylpyridine, 0.1 M guanidinium thiocyanate. A Pt coated FTO electrode was used as the counter electrode, and a Parafilm spacer was employed to ensure no contact between the working and counter electrodes, and allow for electrolyte. I-V scans were conducted in the dark to ensure that there was no incorporated current bias at zero voltage.

4.4.2 IPCE and I-V Device Characterization

RuP derivatized sTiNT, sTiNT₃₀₀ (sTiNT film annealed at 300 °C in Oxygen environment), TiNS, and TiNS₄₀₀ (TiNS film annealed at 400 °C in Oxygen environment), films were incorporated into sandwich cell configurations with a Pt Coated FTO counter electrode. Current-voltage curves are shown in Figure 52.

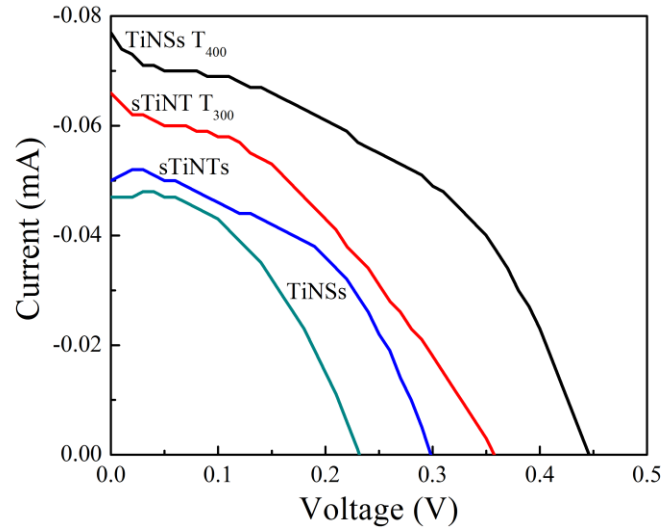


Figure 52: I-V Curve of sTiNT and TiNS films

From these measurements, open circuit voltages (V_{oc}), short circuit currents (J_{sc}), and fill factors (FF) for films thermally annealed in O_2 were higher than for non-annealed films. These quantities were evaluated by the standard equations $FF = I_{mp} * V_{mp} / I_{sc} * V_{oc}$, and $\eta = P_m / E * A_c$ (FF is the fill factor, I_{mp} is the Current at Max Power, and V_{mp} is the voltage at max power, E is the irradiance, and A is the effective surface area.) The calculated values for these are shown in Table 5.

	V_{oc} (V)	J_{sc} (mAcm ⁻²)	P_{max} (mW)	FF	η (%)
sTiNTs	0.30	-.050	.013	.86	.86
sTiNTs₃₀₀	0.36	-.066	.008	.33	.33
TiNS	0.23	-.047	.005	.46	.46
TiNS₄₀₀	0.45	-.076	.013	.38	.38

Table 5: V_{oc} , J_{sc} , and FF from I-V curve analysis of sTiNT and TiNS devices.

Despite the increased performance with annealing, the V_{oc} values reported here are lower than previously reported for RuP on nanoTiO₂ (>0.50 V in a comparable electrolyte).⁶⁹ The reduced value relative to the sintered nanoparticle films is, no doubt, due to a decrease in electron conduction efficiency.

The incident-photon-to-current conversion efficiency (IPCE) for RuP on sTiNT, sTiNT₃₀₀, TiNS and TiNS₄₀₀ are shown in Figure 53. Induced photon to current efficiency is a ratio between the amount of incoming light to the amount of induced current in the cell (Equation 9).

$$IPCE\% = \frac{I_{sc}(A)}{P(W)} \times 1240\lambda(nm) \times 100$$

Equation 9: Induced photon to current efficiency (IPCE)

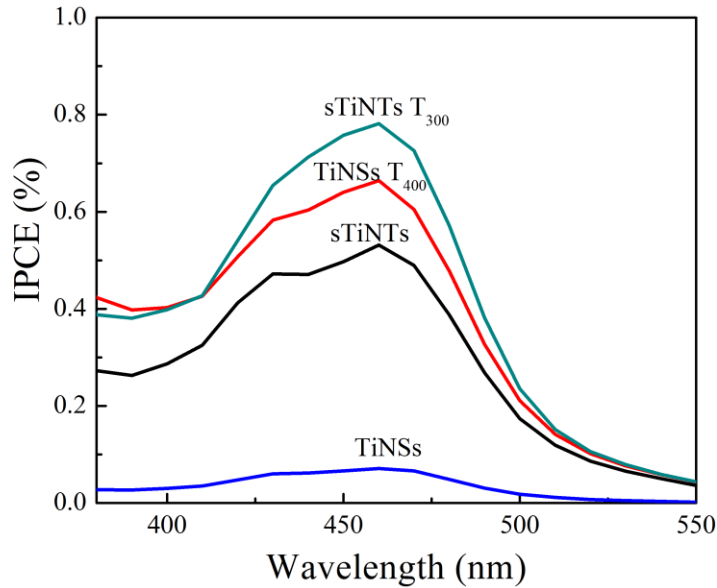


Figure 53: IPCE measurements of TiNSs and sTiNTs films with standard annealing treatment (300 °C) and TiNSs annealed at 400 °C in an oxygen environment, and sTiNTs annealed at 300 °C in an oxygen environment.

Maximum conversion efficiencies (at 450 nm) of 0.5%, 0.7%, 0.1%, and 0.8% were measured for the sTiNT, sTiNT₃₀₀, TiNS, and TiNS₄₀₀ films, respectively. The trend in these data coincide with the trend in V_{oc} values. The maximum IPCE values reported here (<1%) are considerably lower than those previously reported for RuP on nanoTiO₂ (>50%).⁶⁹ The values are low most likely due to the decreased connectivity between sTiNTs/TiNS particles and defects in the tube/sheet structure which decrease rates for conductivity and long range electron transfer.

Absorbed photon-to-current efficiency (Equation 10), plots were also analyzed to account for differences in dye adsorption on the surface of the TiO₂.

$$APCE(\lambda) = \frac{IPCE(\lambda)}{\text{Fraction of light absorbed}}$$

Equation 10: Absorbed photon-to-current efficiency (APCE)

For sTiNT, sTiNT₃₀₀, TiNS, TiNS₄₀₀ the maximum APCE values (at 450 nm) are 1.6%, 2.2%, 0.3%, and 3.5% as shown in Figure 54. Temperature treatment of sTiNT and TiNS films in an oxygen environment before dye loading enhances yields giving the highest IPCE/APCE values.

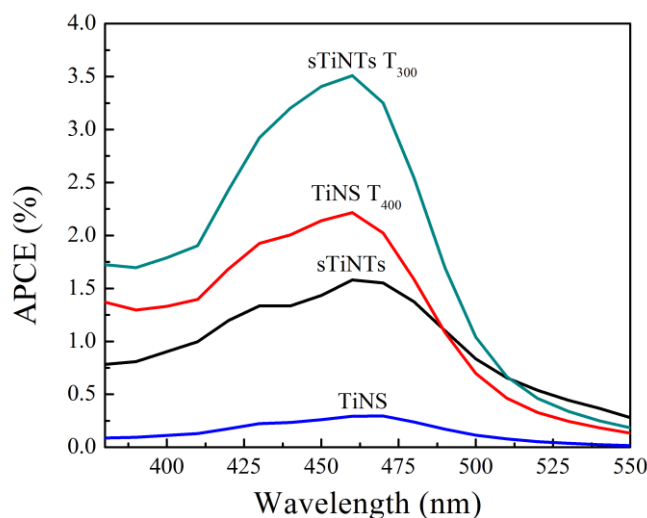


Figure 54: APCE measurements of TiNSs and sTiNTs films with standard annealing treatment (300 °C) and TiNSs annealed at 400 °C in an oxygen environment, and sTiNTs annealed at 300 °C in an oxygen environment.

IPCE values in mesoporous anatase films are enhanced by calcination at high temperatures.⁷⁰ Calcinating nanotube films at 300 °C in an oxygen environment prior to loading the dye from pH 1 HClO₄ enhanced IPCE values at 450 nm from 0.5% to 0.7% for the sTiNT films and from 0.1% to 0.8% for the TiNS films. The enhancements are likely due to enhanced connectivity similar to necking effects that have been observed for calcinated films of TiO₂ nanoparticles.⁷⁰ Annealing at temperatures above 300 °C destroys the nanotube structure. The limitation due to this thermal instability limits connectivity between tubes relative to nanoparticle films calcinated at higher temperatures. The resulting non-optimal local arrangement between tubes does not allow electrons to diffuse to the underlying FTO substrate due to limited connectivity at the boundaries between tubes.

In addition to the thermal instability problem, sTiNTs and TiNS band gaps at ~ 3.7 eV and ~ 4 eV, respectively are higher than the 3.2 eV band gap of standard anatase NPs contributing to a decrease in electron injection yield. A dye with a higher excited state reduction potential may increase both sTiNTs and TiNS photoanode performance. It is also important to consider that the efficiency of the RuP dye in a DSSC is on average a factor of ten lower than N719 on the same surface. Projecting the N719 data from the RuP data the maximum conversion efficiencies (at 450 nm) should increase to 5%, 7%, 1%, and 8% for the sTiNT, sTiNT₃₀₀, TiNS, and TiNS₄₀₀ films, respectively. Even with this optimistic scaling the viability of the sTiNTs into devices is highly questionable and most likely not worth pursuing further.

Ntile films were also tested for device capabilities and performed markedly better than the sTiNTs and the TiNS. Two of the ntile batches were evaluated for the device potential. These two batches were batch #10 and batch #11 which had different synthesis conditions and resulted in differing morphology of the final nanomaterial as seen in Figure 56. There was variation in the performance of the materials most likely due to their film forming ability. The batch synthesized at 180 °C was able to make much more uniform films as compared to the batch that was synthesized at 135 °C. This can be seen in Figure 55.

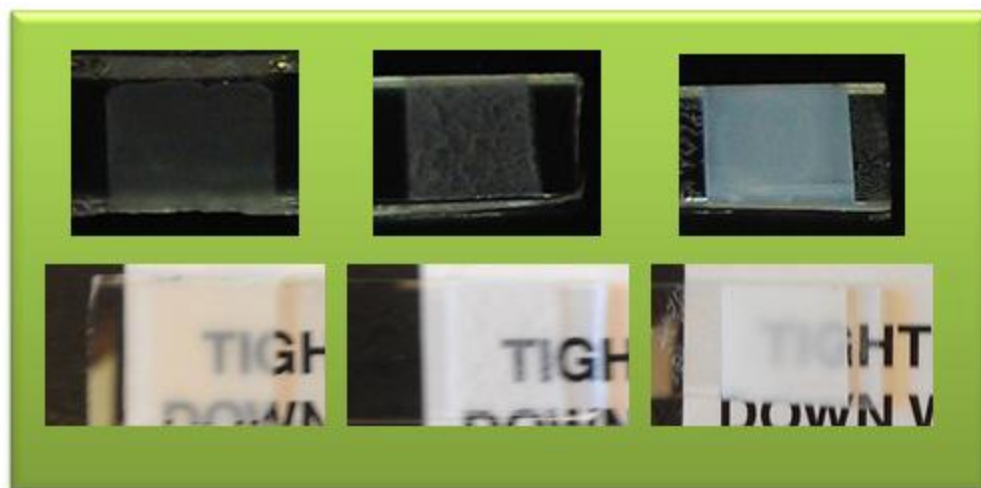


Figure 55: Photographs of batch 10 spin coated ntile film, batch 11 spin coated ntile film, doctor bladed batch 10 ntile film.

Batch	TiBuOx (mL)	HF (mL)	Temperature °C	Time (hours)	Side Length (nm)
10	21	2	180	24	60
11	21	2	135	72	10-20

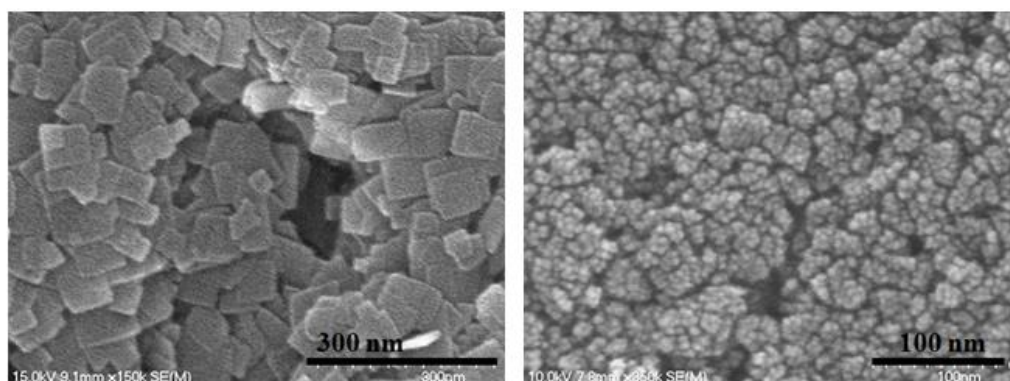


Figure 56: Ntile batch synthesis conditions and SEM images of batch 10 (left) and batch 11 (right)

The Voc for the ntile was -0.75 V and -0.71 V for batch 10 and 11 respectively and the Jcs was 1.4×10^{-3} and 7.8×10^{-4} for batch 10 and 11 spin coated films respectively. Both devices performed significantly better than the original sTiNT and TiNS samples.

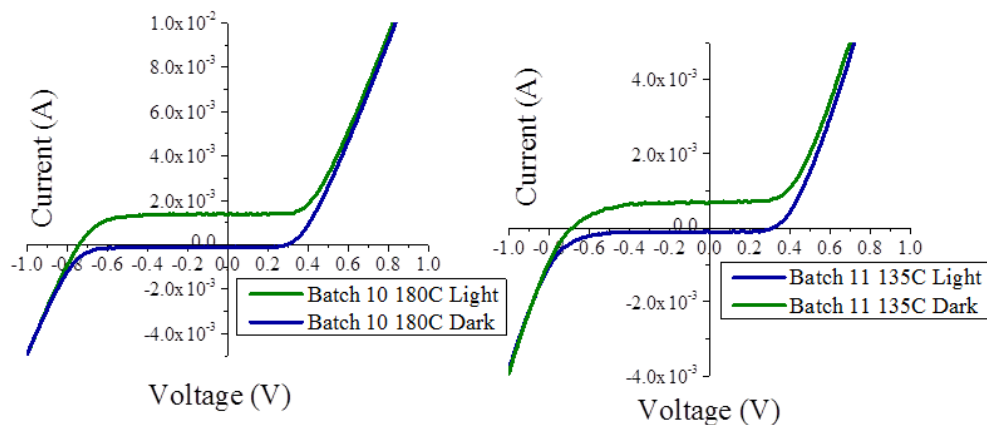


Figure 57: I-V Sweeps of N719 derivatized nanotiles batch 10 (left) and batch 11 (right)

Both batches performed similarly in IPCE analysis with maximum conversion efficiencies of 11.5% and 11% for batch 10 and batch 11 respectively. These values though improved from the sTiNTs and TiNS samples are still lower than desired for effective device measurements. The reason for the lower than expected performance in the IPCE measurement is due to poor dye uptake on the (001) surface which will be addressed and discussed in the next chapter.

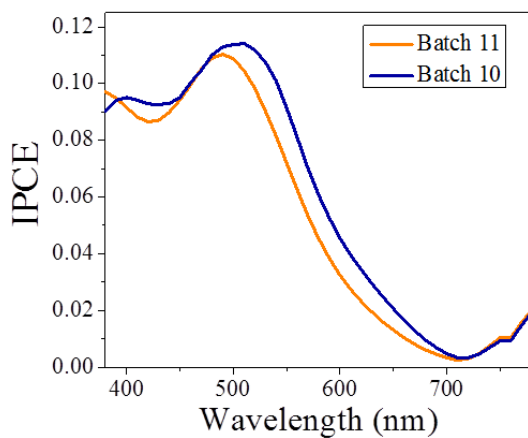


Figure 58: IPCE measurement of batch 10 and batch 11 Ntile films derivatized with N719

Dye

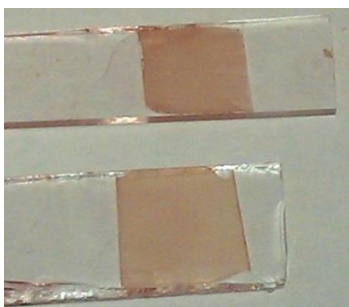


Figure 59: N719 loaded Ntile films deposited on glass (top) and FTO (bottom)

To improve the available surface area of the ntile films a sonication treatment was used to break up any TiO_2 aggregates prior to incorporation into the film paste and allow for a more uniform deposition. Films were doctor-bladed to allow for thicker film. This yielded an increase in device efficiency. For these measurements two new devices were tested and the IPCE results are shown in Figure 60 with the previous spin coated device presented for comparison.

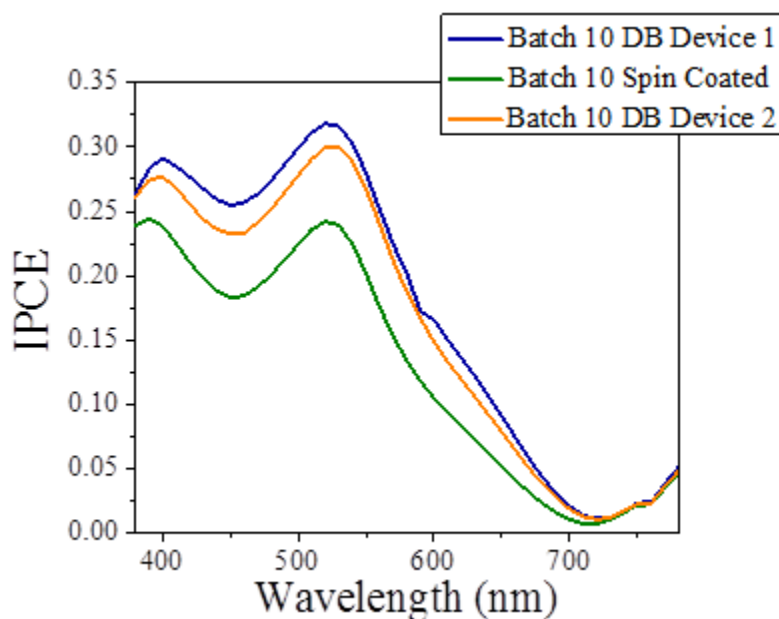


Figure 60: IPCE results of doctor-bladed ntile films with previous spin coated film for comparison.

These devices were also characterized by I-V measurements to determine the overall efficiency as shown in Table 6. Applying thicker films ($1.5\ \mu\text{m}$) by doctor-blading and applying to short sonicating procedure to the paste before deposition allows for an increased open-circuit potential. These results are an enhancement and improvement of similar works by Gratzel. I-V results are shown in Figure 61 and Table 6, published results are shown in Figure 62⁷¹ for comparison.

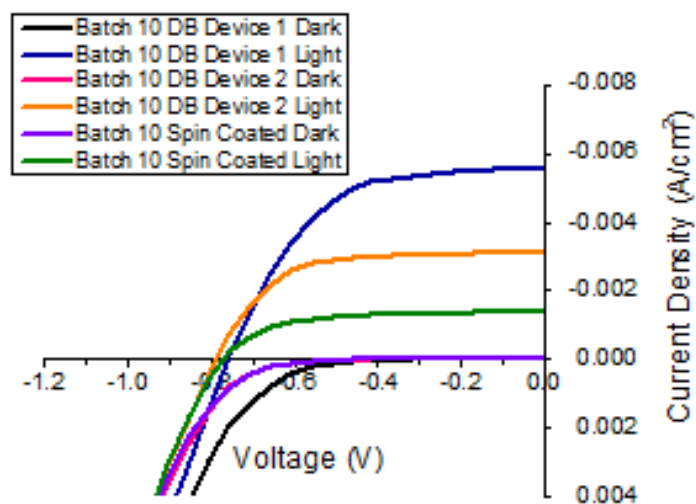


Figure 61: I-V curves of doctor-bladed and spin coated ntile films

	DB Ntiles Device1	DB Ntiles Device2	Spin Coated NTiles
Solar Cell Area (cm ²)	6.40E-01	6.40E-01	6.40E-01
Light Intensity (mW/cm ²)	100	100	100
Isc (mAmps)	-3.565	-2.012	-0.864
Voc (Volts)	-0.758	-0.787	-0.769
Efficiency (%)	2.38	1.557	0.671
Pmax (Watts)	0.002	0.001	0
Imp (mAmps)	-2.974	-1.776	-0.704
Vmp (Volts)	-0.512	-0.561	-0.61
Fill Factor (%)	56.371	62.941	64.589

Table 6: I-V characterization data for doctor-bladed (DB) films and spin coated films

Film type	100 % sun			
	I_{sc} [mA/cm ²]	U_{oc} [mV]	FF	η [%]
A-(001)	8.78	708	0.69	4.3
A-(101)	10.4	660	0.69	4.7
E-(001)	5.34	725	0.72	2.8
E-(101)	6.36	681	0.71	3.1

Figure 62: I-V characterization of standard (101) NP films and (001) nanosheets films from literature, A denotes paste deposition as used in this dissertation and E represents particles deposited from Ethanol suspension⁷².

The important results from this are that there is an enhancement of the Voc due to the (001) surface and assuming dye coverage can be improves the IPCE would also improve. It is very worthwhile to continue pursuing this material.

4.4.3 Electrochemical Impedance Spectroscopy Measurements on Ntile films

Electrochemical impedance spectroscopy is a powerful tool that can be used to elucidate ionic and electronic pathways in DSSCs. A standard DSSC can be approximated as a circuit as represented in Figure 63. With the circuit elements being representative of portions of the electron transfer in the DSSC. The labeled quantities represent the following physical properties of the cell R_1 is the internal resistance of the FTO, R_2 is the resistance between the FTO and the TiO_2 at the point of contact and CPE_1 is the capacitance of the FTO/ TiO_2 interface. Recombination of electrons at the interface between the TiO_2 and the electrolyte is represented by R_3 , and R_4 represents the resistance the electron experiences as it is transported through the TiO_2 . And lastly C_1 and CPE_2 represent the capacitance of the steps encountered in R_3 and R_4 .⁷³

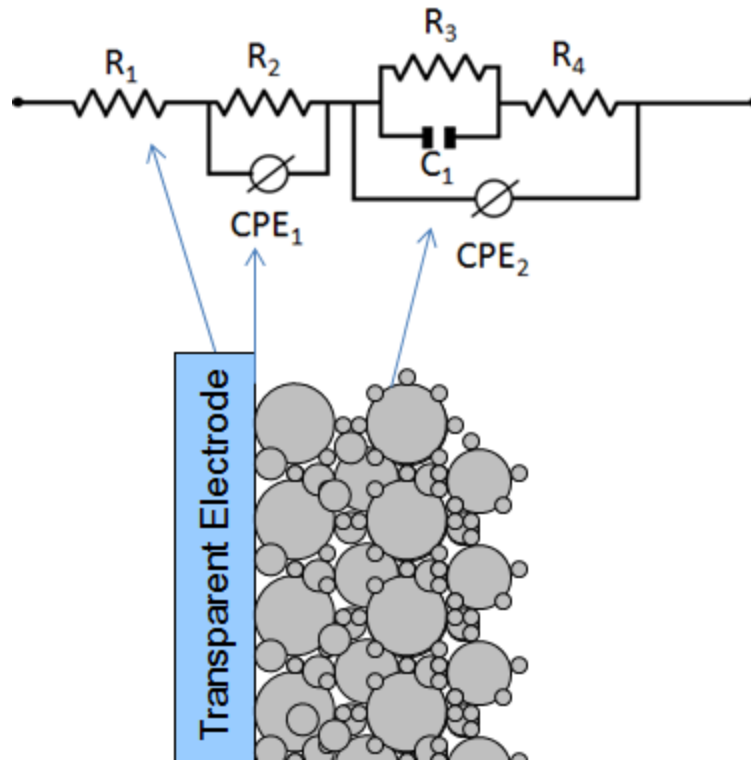


Figure 63: Circuit approximation of electrode side of DSSC⁷³

With this approximation the TiO_2 performance can be evaluated to develop a more complete understanding of the cell. The data can be presented in two methods the first is using a Nyquist plot which for a DSSC will have three apparent semicircles, this is representative of the circuit at low, medium, and high frequencies. In turn translating this data into a Bode plot will result in three frequency peaks. As the performance of the device degrades the middle peak will tend to lose its form as can be seen in Figure 64.

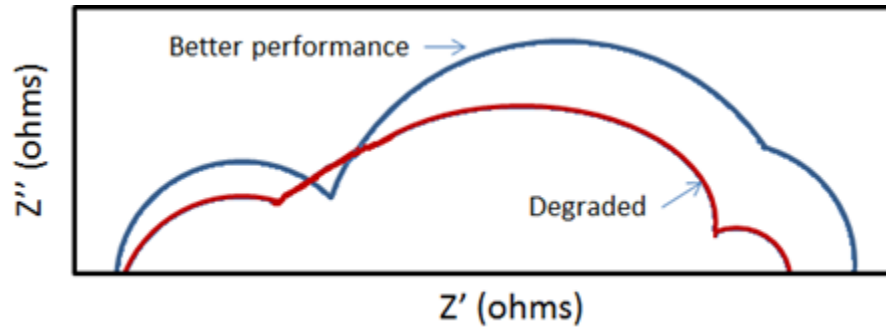


Figure 64: Sample Nyquist plot of metal-oxide electrode⁷³

CHAPTER 5: DYE LOADING, BINDING MECHANISM, AND STABILITY

5.1 Dye Adsorption and Stability Discussion

For dye derivatized devices to be viable for use in solar fuel application all aspects of the devices need to be stable in aqueous conditions and under sunlight irradiation. These requirements are by no means trivial. Water is an excellent polar solvent and thus problematic for stable binding between a molecule and a surface. Thus far the majority of work done on increasing binding and stability of dye sensitized solar cells has centered around modifying the anchor groups that attach the dye to the TiO_2 surface. A majority of this work has focused on carboxyl and phosphonate linkers shown in Figure 65.

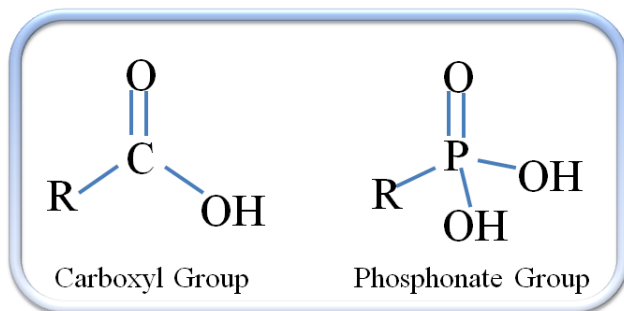


Figure 65: Schematic of Carboxyl and Phosphonate linker groups

Initial synthesis of the Ru based photosensitive dyes involved carboxyl linkers which perform well with induced photon to current efficiencies and open-circuit voltages.

Extensive work has been focused on characterizing the binding parameters of the carboxyl groups to the surface. It is well known that with decreasing pH an increased amount of carboxyl dye can attach to the surface. The reasoning for this being that by decreasing the pH of the solution the surface charge on the TiO_2 is modified to facilitate dye binding. pH modification of the surface is achieved by immersing it in an electrolyte which will change the charge on the surface unless the electrolyte is at a pH which corresponds to the zero-charge point of the surface. In general when a metal oxide is immersed in a solution of sufficiently low pH it will develop a positive surface charge and conversely when immersed in a high pH solution the surface will develop a negative charge as the hydroxyl groups (or molecularly adsorbed water groups) are deprotonated.⁷⁴ Depending on the protonation of the linkers on the carboxyl dye salt a decreased pH of the solution will generally facilitate solubility and surface attachment. For use with dye sensitized solar cells the carboxyl group performs admirably however when switching to hydrogen generation they run into some issues. The carboxyl linkers are very sensitive to any competing adsorbates that would be present in the electrolyte. To facilitate hydrogen generation it is common place to use a sacrificial agent such as methanol or ethanol. In addition to being used as sacrificial agents these alcohols compete for the same binding sites as the carboxyl groups and cause instability of the dye binding and reduced photo activity.³⁴ It is for this reason that alternate binding groups have been explored.

Phosphonate groups have replaced the carboxyl groups as linkers for hydrogen generation applications. They have been shown to not be as sensitive to being affected by competing adsorbates and are stable on the metal-oxide surface over a larger pH range.³⁴

This stability is further demonstrated by the ability to load dye onto the surface at higher pH values than their carboxyl predecessors. The ability to load over a broader pH range is indicative that the phosphonate groups have a higher affinity for the metal-oxide surface than carboxyl groups. When specifically considering hydrogen production the photo-activity of a metal-oxide surface derivatized with phosphonate anchor group dyes is not decreased by exposure to sacrificial agents. The phosphonate anchor group shows enhanced stability over a broader pH (up to 5) range than the original carboxyl linker dyes. Even so, recent studies have shown that upon illumination at low pH values this enhanced stability breaks down.³⁵ With all of these studies little care has been taken to study the metal-oxide surface and its roll in stability. We have already extensively discussed the enhanced reactivity of the (001) surface in great detail. This reactivity can also translate over to increased dye stability in both aqueous conditions and under illumination. To explain this increased stability it is important to understand the binding mechanism and motif. The following studies will evaluate the stability and binding of the phosphonate group to the TiO₂ (101) and (001) surface using a variety of optical and nuclear magnetic resonance techniques.

5.2 Dye Surface Coverage of (101) and (001) surface

Frequently it is taken for granted molecules bind relatively easily to TiO₂. Without much effort carboxyl and phosphonate groups (to name a few) attach to the surface. In the case of phosphonate groups surface attachment is achieved by lowering the pH of the dye solution to protonate the surface and enhance binding. The surface is an important factor in binding and different surfaces of TiO₂ will behave and bind to molecules differently. For this the amount and stability of the molecule is important.

5.2.1 Dye Loading Conditions

RuP was prepared according to the literature procedure.⁷⁵ All films (either on glass or FTO glass) were immersed in shell vials containing 1×10^{-4} M RuP in 0.1 M HClO₄ aqueous solution or 1×10^{-4} M N719 in dry acetonitrile. In order to maintain consistent loading, slides were derivatized by using the same stock dye solution. Samples were left in the dye solutions for 48 hours at 40 °C, and then transferred to a 0.1 M HClO₄ aqueous solution (without dye) for 24 hours to remove any unbound dye or aggregates.⁷⁶ Lastly, the slides were dried under a stream of nitrogen.

5.2.2 Dye surface coverage comparison

For high efficiency DSSCs it is important for metal-oxide semiconductor to have a high surface area available to allow maximum dye coverage. This is achieved by the use of nanomaterials in the DSSC. However, size-structure is not the only parameter that needs to be considered when selecting a material for DSSCs. The amount of available binding sites on the surface of the material is also an important factor that will determine dye coverage. There were initial published reports detailing that the amount of adsorbed dye was increased on the (001) face as compared to the standard (101) face.^{23,77} Careful study of these reports brings light to their faulty nature by translating their reported surface coverage to molecules/nm² non-physical quantities arise. These reports have recently been openly challenged in literature and with my own findings. It is well known that dye coverage on standard (101) NP films far exceeds monolayer coverage which I

show is further evident when discussing dye stability in the next section.⁷⁸ Increased dye coverage due to greater than monolayer coverage is not advantageous because it hinders electron injection. To compare dye coverage on the various TiO₂ surfaces it is helpful to remove the exponential contribution from scattering in the film. This allows for magnitude comparison of amount of dye loaded on the surface of the different morphologies as seen in Figure 66. Using the absorbance of the NP film as reference the relative max loading for the other films are as follows the sTiNT coverage is approximately 44% of the NP coverage and the TiNS and Ntile films have ~33% of the coverage. It has been documented in literature that the dye loading on (001) surfaces does not tend towards greater than monolayer coverage which is represented here. Additionally the enhanced coverage seen on the sTiNT film as compared to the TiNS and Ntile films can be attributed to the higher surface area of the sTiNTs. The explanation for the differences in surface coverage will be further explored in the rest of this chapter.

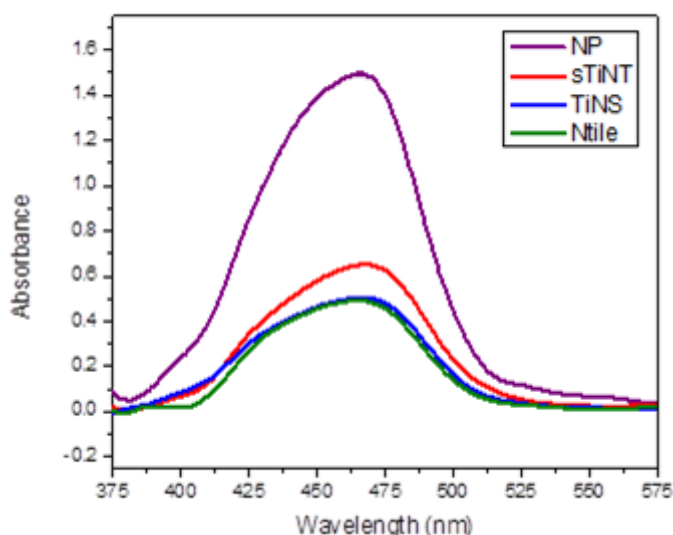


Figure 66: Absorbance of RuP on NP, sTiNT, TiNS, and Ntile films with scattering background removed for direct comparison

5.3 Dye Stability

As previously mentioned, dyes with carboxyl attachment groups are unstable on the standard TiO_2 surface at elevated pH values (>1) and in environments where they are competing with other adsorbates. Dyes with phosphonate attachment groups are more stable than their carboxyl predecessors however they have been shown to not maintain this stability under illumination and at elevated pH values (>5 .) This section will explore the stability of dyes with phosphonate linkers on specific surfaces of anatase titania and attempt to explain a reason for the enhancement seen on the (001) surface over the standard (101) surface.

5.3.1 Experimental Methods

The aqueous stability of RuP on standard nanoparticle, sTiNT, TiNS, and Ntile films was investigated by immersing the RuP loaded NP, sTiNT, TiNS, and NTile coated glass slides into a solution of pH 6.9 MilliQ water for 1, 3, and 10 days. UV-Vis absorption data was measured, for both the slide and the soaking solution, periodically during the three days of soaking. The solution was replaced with fresh water every 24 hours for the first 3 days. When not being measured the vials were stored in aluminum foil.

Photostability measurements were performed via the following specifications. Photoanodes were irradiated with a royal blue LED (Thorlabs Inc. model M455L2, 455 nm, ca. 30 nm FWHM) powered by a T-Cube LED Driver (Thorlabs Inc. model LEDD1B). The LED output was directed into a focusing beam probe (Newport Corp. part # 77646) fitted with a second lens (fused silica, 38 mm focal length, Newport Corp.

part# 41230) to achieve a 2.5 mm diameter beam at the sample. The incident light intensity was measured to be 475 mW/cm^2 using a Coherent power meter (Newport Corp 1918-C) and Coherent detector (Newport Corp 818P-020-12). Derivatized electrodes were placed into a 10 mm path length cuvette at 45° . Liquid solutions (5 mL) were also added to the cuvette. For all experiments here liquid solutions consisted of 1M HClO_4 in water. At the sample, the LED illumination spot was positioned to overlap perpendicularly with the white light of a Varian Cary 50 UV-Vis spectrophotometer. The absorption spectrum (360-800 nm) of the film was collected every 15 minutes during 16 hours of illumination. The solution temperature, $22 \pm 2^\circ\text{C}$, was consistent throughout the duration of the experiment.

5.3.2 Aqueous Dye Stability Results

Absorption spectra of films of NP, sTiNTs, TiNS, and NTiles loaded from a $1 \times 10^{-4} \text{ M}$ RuP stock solution in 0.1 M HClO_4 can be seen in Figure 66. The films display behavior common for ruthenium polypyridyl complexes on metal oxide films featuring a low energy metal-to-ligand charge-transfer (MLCT) absorption feature in UV-visible spectra from 400-500 nm. Lower dye coverage is observed on all of the (001) enhanced morphologies. The reason for this is most likely due to the hydroxyl groups that stabilize the (001) under-coordinated titanium. These hydroxyl groups stem to limit the number of available binding sites. This explanation will be further explored later in the chapter. Spin coated NTile films were determined with profilometry and SEM to have a thickness of $0.8 \mu\text{m} \pm 0.2 \mu\text{m}$ as compared to the $\sim 2 \mu\text{m}$ thickness of the sTiNT and TiNS films. The derivatized films were then immersed in MilliQ H_2O with the solution replaced

every 24 hours with periodically monitored by UV-visible measurements the absorbance change can be seen in Figure 67.

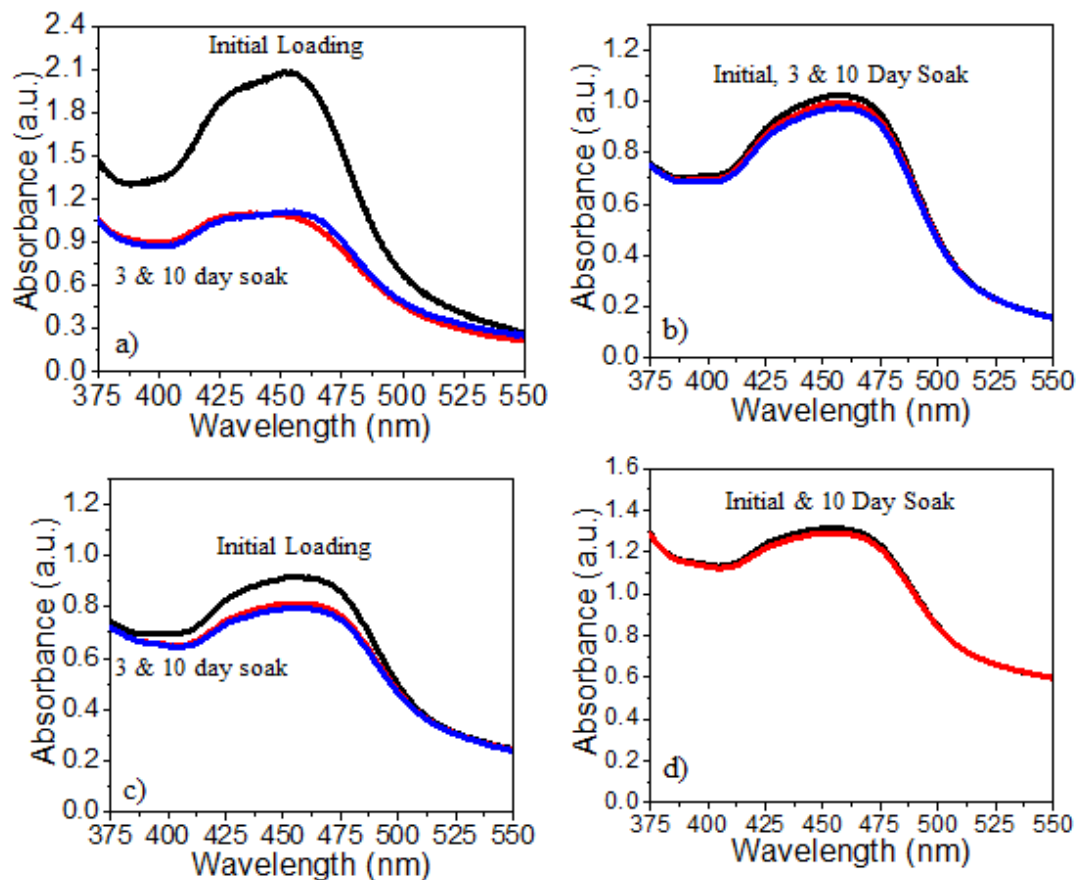


Figure 67: RuP derivatized films of a) Standard NPs b) TiNSs c) sTiNTs d) Ntile

The MLCT feature of RuP on TiNS and Ntiles top solution remained unchanged over the course of 10 days demonstrating minimal dye desorption even in neutral solution the combination of the large amount of scattering in the ntile film and the lower RuP dye coverage their absorption spectra has not been shown here. The sTiNT films had a small amount of dye loss on the first day and this is attributed to dye that was not stably bound to the surface to begin with. For the standard NP slide derivatized with RuP, significant

desorption (>60%) occurred for the first 24 hours with a continued decrease over the first 5 days (>2%). It is worthwhile to make a qualitative argument about remaining dye coverage. By removing the scattering background from all the samples the maximum absorbance of the dye is 0.25 for the NP films, 0.15 for the TiNS film, and 0.35 for the sTiNTs. Since both the dye (RuP) and environmental conditions were constant, the increased stability of sTiNTs, TiNS, and Ntiles over NP TiO₂ is likely due to the more stable bonding of the phosphonate groups to the (001) crystal plane. To further detail this additional NMR studies will be used to elucidate the binding.

5.3.3 Photo-Stability of Dye Results

Photostability under conditions appropriate for water splitting is an important issue for water splitting and solar fuel applications. The surface stability of RuP on TiNS, Ntiles, and NP TiO₂ in 0.1 M HClO₄ under standard photolysis conditions was assessed by utilization of previously published procedures.³⁵ During irradiation with 455 nm light (FWHM ~30 nm, 475 mW/cm²), a gradual decrease in absorbance 400-490 nm was observed for all samples due to desorption and loss of the complex from the surface as shown in Figure 68.

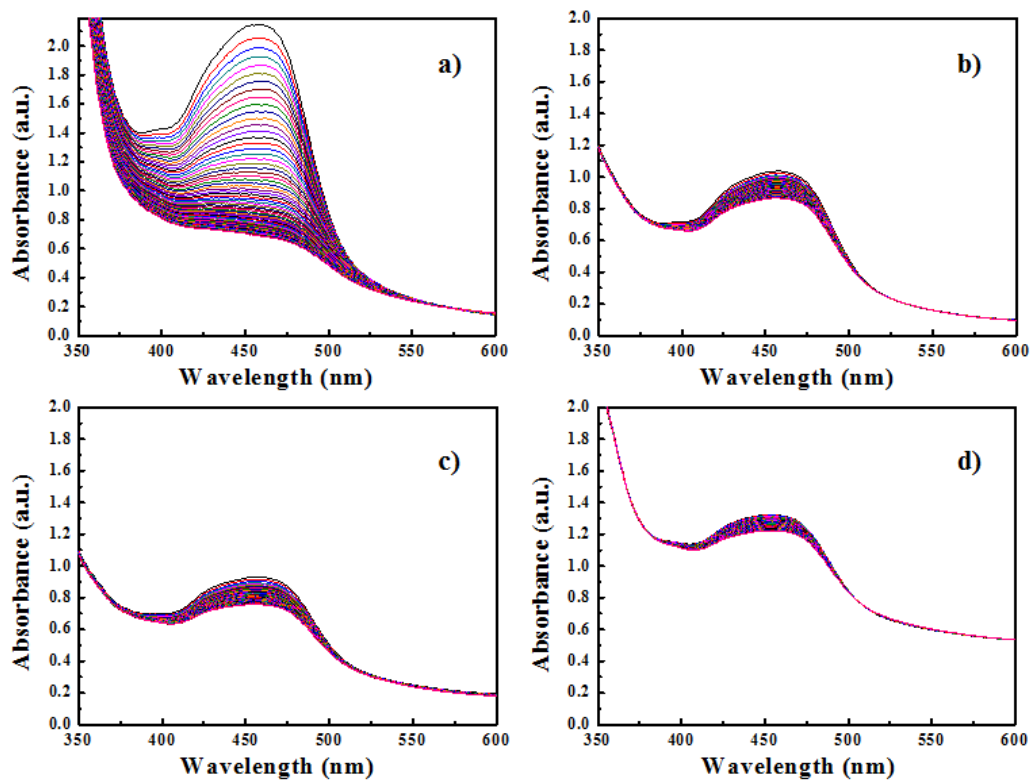


Figure 68: Photostability measurements of RuP loaded surfaces in 1 M HClO₄ of a) Standard NP film b) sTiNT film c) TiNS film d) ntile film

Absorption-time traces at 480 nm could be fit satisfactorily with the biexponential function in Equation 11. Data from the biexponential analysis are presented as an average rate constant, k_{des} , calculated by using the weighted average lifetime ($\langle t \rangle$) in Equation 12.

$$k_{des} = A_1 e^{-k_1 t} + A_2 e^{-k_2 t}$$

Equation 11: Dye desorption rate fit

$$1/k_{des} = \langle t \rangle = \sum A_i t_i^2 / \sum A_i t$$

Equation 12: Average desorption lifetime

For loss of RuP from the TiO₂ films can be seen in Table 7.

	k_{des}	~Factor Slower
NP Film	$5.0 \times 10^{-5} \text{ s}^{-1}$	1
sTiNT Film	$1.3 \times 10^{-5} \text{ s}^{-1}$	4
TiNS Film	$2.5 \times 10^{-5} \text{ s}^{-1}$	2
Ntile Film	$0.5 \times 10^{-5} \text{ s}^{-1}$	10

Table 7: Desorption rates of RuP dye under illumination

These desorption values are slower by a factor ~2 to ~10 for the TiNS, sTiNTs, and Ntiles respectively than loss from NP TiO₂ under the same conditions. The increased stability of RuP on TiNS and NTiles is most likely due to binding of the dye to the (001) surface of the nanosheets, and nanotiles as compared to the majority (101) surface of the nanoparticles.

5.4 Dye Binding Mechanism

A number of techniques were employed to elucidate the reason for the enhanced stability that is seen on the (001) surface as compared to the standard anatase (101) surface. In order to increase the amount of coverage on the surface of the TiO₂ morphologies an alternate smaller molecule was used with the same phosphonate linker group. That molecule is phenyl-phosphonic acid (PPA) as shown in Figure 69. Initial studies were tried with just the ligand of the RuP dye molecule but solubility and contaminants in the ligand synthesis did not allow for consistent loading and results. Additionally the cost and availability of the PPA molecule over the RuP dye gave the final additional reasoning for the switch.

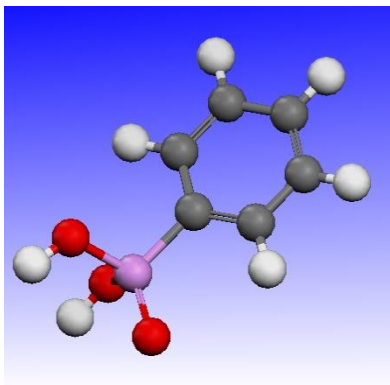


Figure 69: Phenylphosphonic acid molecule with carbon (grey), hydrogen (white), oxygen (red), and phosphorus (pink)

Since the goal of this study is to determine the binding mechanism of the phosphonate groups to the (101) and (001) surface of titania the molecule PPA is a reasonable switch for the RuP dye.

Thus far in literature there have been no studies looking at the phosphonate group binding to specific surfaces of (101) and (001) anatase titania. The only studies that have been done just focused on using p25, or generic anatase as the surface. As previously discussed, p25 is a mixture of anatase and rutile nanoparticles and thus not the best choice for specific surface studies. To develop a better understanding of the phosphonate group binding four morphologies of TiO_2 were used: 32 nm Anatase nanoparticles, LTiNTs, ntiles, and p25 for comparison. To determine the dye binding mechanism and develop a better understanding for the stability differences seen on the (101) and (001) surfaces two techniques were used. The first is attenuated total reflectance infrared spectroscopy (ATR-IR) which is able to elucidate binding of the surface of material. And the second is nuclear magnetic resonance (NMR) which is able to determine binding modes and local electron density of the binding which translates to strength of the bond.

5.4.1 Attenuated Total Reflectance-Infrared Spectroscopy

The principle of ATR-IR stems from measuring any changes that occur in a totally internally reflected beam when it comes into contact with the sample. An optically dense crystal with a very high refractive index is used and an IR beam is directed into the crystal. The total internal reflectance creates an evanescent wave that extends outward into the sample. Depending on the material and specific tool this penetration depth is at most 2-5 μm . It is this reason that the sample is compressed onto the crystal to ensure good contact between the material and the crystal. Changes in the evanescent wave from where the material being tested absorbs the energy are what is monitored.⁷⁹ The energy is absorbed by the molecules in vibration and stretching modes within the bonds of the material, a schematic of the ATR-IR set up can be seen in Figure 70.

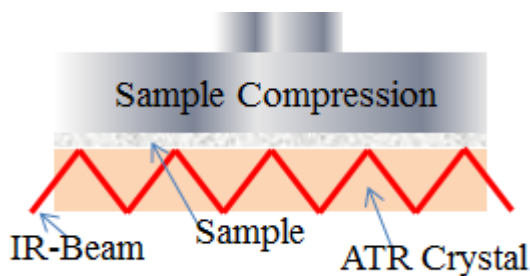


Figure 70: ATR-IR Schematic

The samples were measured in powder form before and after being derivatized with PPA. Powder samples of 2-4 mg were placed directly on the crystal and scanned from 4000 cm^{-1} to 375 cm^{-1} wavenumbers. Three different samples were run to verify consistency using the Alpha (Bruker) spectrometer with Platinum ATR attachment. Signal was averaged over 50 scans to get final result.

5.4.2 Attenuated Total Reflectance-Infrared Spectroscopy Results

Four morphologies of TiO_2 were analyzed to determine the binding mode, 32nm anatase, p25, LTiNTs, and ntiles. All samples were measured before and after being derivatized with PPA. From literature the relevant absorbance regions that are important for dye binding for these measurements are absorbance between $1000\text{--}1100\text{ cm}^{-1}$ wavenumbers which corresponds to free O-P-O or PO_2^- groups and the signal at 1230 cm^{-1} which is indicative of the presence of P=O bonds. Additionally, for the un-derivatized samples there is a broad O-H stretching signal that appears $3200\text{--}3550\text{ cm}^{-1}$ wavenumbers.⁸⁰

The first analysis will be of the un-derivatized TiO_2 samples which can be seen in Figure 71.

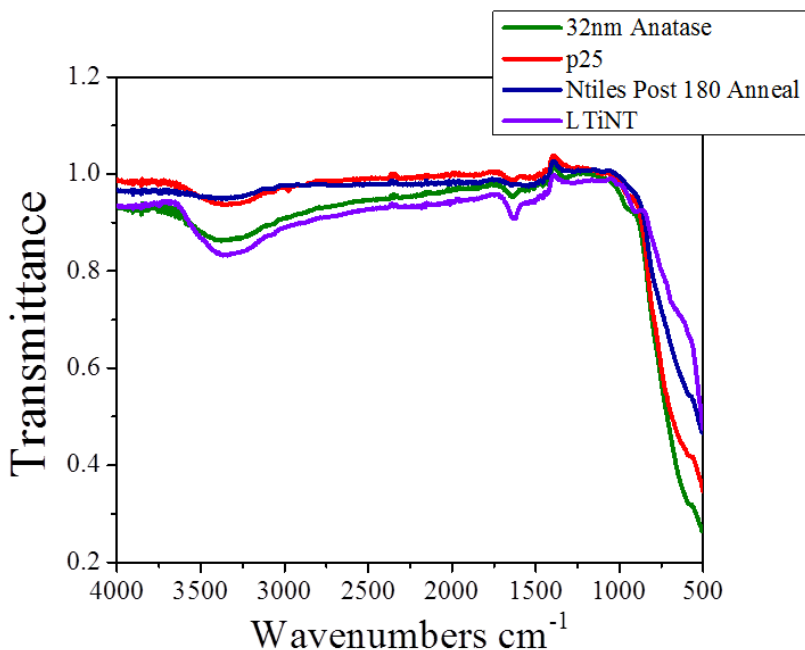


Figure 71: ATR-IR spectra of bare 32nm anatase, p25, ntiles, and LTiNTs

A broad peak can be seen in each of the four samples in the 3200-3550 cm^{-1} wavenumbers range corresponding to O-H stretching. The smaller sharp peak that occurs around 1630 cm^{-1} wavenumbers is likely due to the H-O-H bonds in the samples when coupled with the stretching signal this is characteristic of -OH groups being adsorbed on the TiO_2 surface.⁸¹ It can also be seen that the strongest signal from this results from the LTiNT sample with is in good agreement with previous findings.³⁸

Changes in the samples before and after being derivatized with PPA can be seen in Figure 72. The importance of these spectra is that they make it clear that the amount of PPA on the surface of the materials can be detected with the ATR-IR technique. A reduction in the transmission on the 32 nm anatase samples corresponds to an enhanced absorbance or reflectance after being derivatized with PPA.

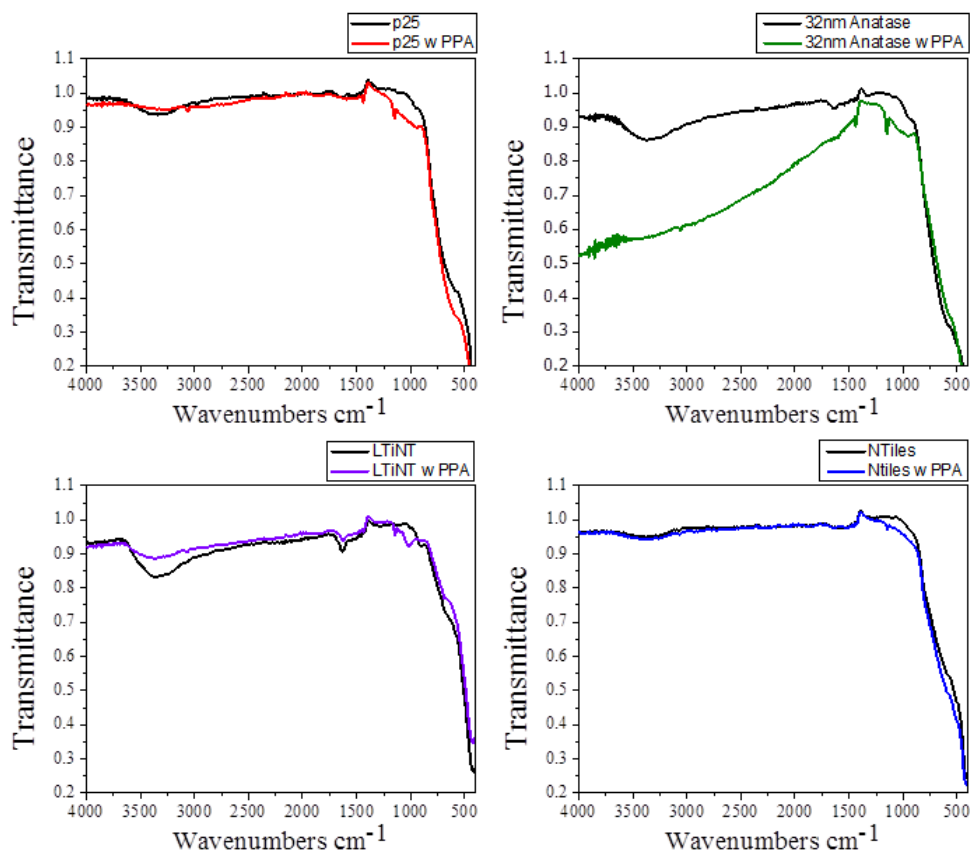


Figure 72: ATR-IR Spectra of TiO_2 samples without and with being derivatized with PPA.

Comparing the derivatized spectra from Figure 72 in more depth a probable binding mechanism can be discerned. Figure 73 shows an in-depth comparison of the various derivatized samples. From these results it is shown that the P=O diminishes for the derivatized samples with the two (001) derivatized samples showing the most reduction. The =O most likely has one of its bonds broken and binds to the under-coordinated titanium atoms on the surface. Additionally it can be seen that the O-P-O stretch for all of the samples goes away which is indicative of either bidentate or tridentate binding. Theoretical calculations have predicted that the tridentate binding is

unfavorable due to bond lengths and geometric constraints so the binding of the phosphonate group to the TiO_2 surface is most likely bidentate.⁸²

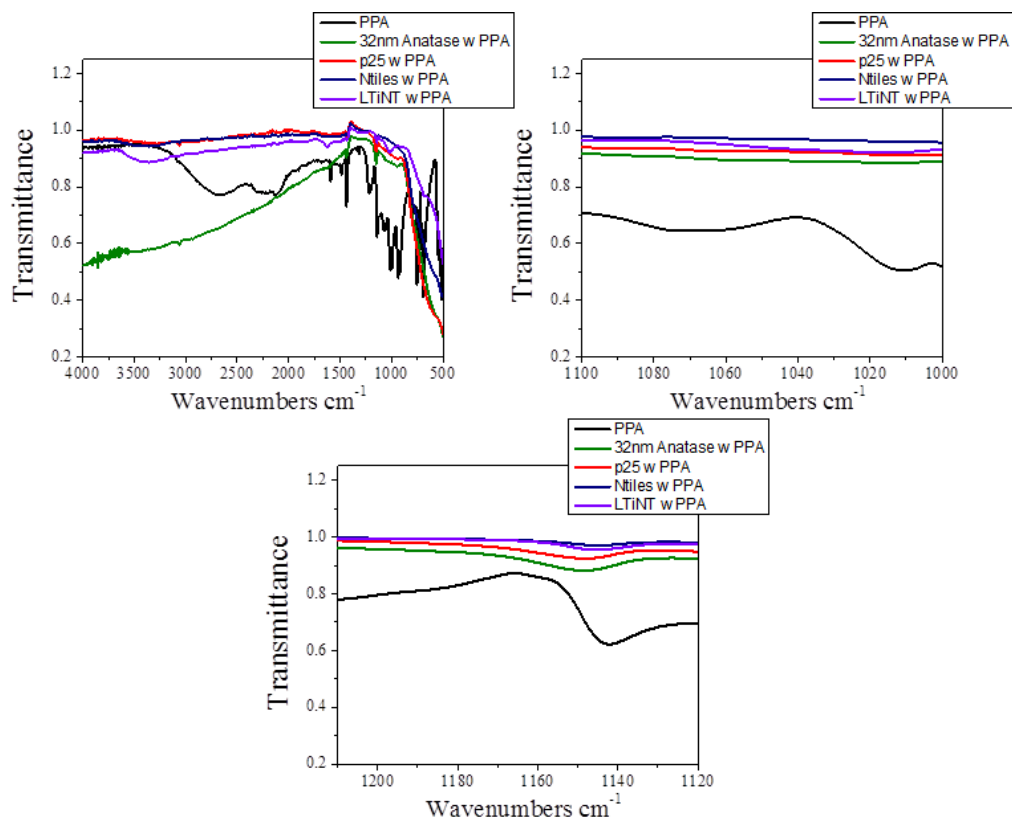


Figure 73: ATR-IR spectra of PPA derivatized TiO_2 samples with zoomed-in graphs of the O-P-O region (top right) and P=O region (bottom center).

5.4.3 Introduction to Nuclear Magnetic Resonance Theory

Nuclear magnetic resonance (NMR) is a powerful tool in understanding the bonding between molecules in a material. This bonding is commonly talked about in reference to a chemical shift in the material. The molecule's electrons cause submolecular local magnetic field variance which translates to nuclei on two different sites of a molecule experiencing a different magnetic field. This effect is what is referred to as the chemical shift which predominantly results from intra-molecular interactions

with secondary contributions resulting from inter-molecular interactions. What this means is that the chemical shift will vary depending on the solvent or any asymmetries in the crystal. The mechanism that creates the chemical shift is a large external magnetic field inducing currents in the electron clouds of the molecules which in turn generate an induced magnetic field. The nuclear spins in the molecule sense the combined magnetic field which results in a change of the spin precession frequency.⁸³ A transient change in the magnetic field that the molecules experience will result in a non-equilibrium state. Additional information about the local environment of the nucleus being studied results from the relaxation time after the transience occurs. The two time parameters that are used to discuss this are T1 and T2 times. Where T1 is also commonly referred to as the spin-lattice relaxation time and T2 is referred to as the spin-spin relaxation time. T1 one is considered the decay constant to recovery of the parallel component of the nuclear spin magnetization whereas T2 is the decay constant that of the magnetization that is perpendicular to the original field. T1 redistributes the nuclear spin states back to thermal equilibrium and T2 is the decoherence of the transverse component of the nuclear spin magnetization.⁸³

5.4.4 Experimental Methods

Magic Angle Spinning (MAS) NMR was performed on the powdered samples at a 9T superconducting magnet analyzing the ^{31}P spectra which have been normalized by mass. An 85% H_3PO_4 aqueous solution was used as an external ^{31}P chemical shift reference. Unless otherwise specified all samples were loaded into a 4mm spinner with teflon based spacers, and all samples mass was acquired before and after data acquisition.

5.3.5 TGA Analysis of Ntiles

As mentioned in the beginning of this chapter the coverage of the dye on the (001) surface is lower than the coverage on the (101) surface and it was initially hypothesized that this was due to the hydroxyl coverage on the surface of the Ntiles. Using thermal gravimetric analysis (TGA) and ^1H NMR the presence of hydroxyl groups can be confirmed. TGA monitors the mass change of a sample in an inert atmosphere as the temperature is increased. The TGA results of the ntile sample are presented in Figure 74.

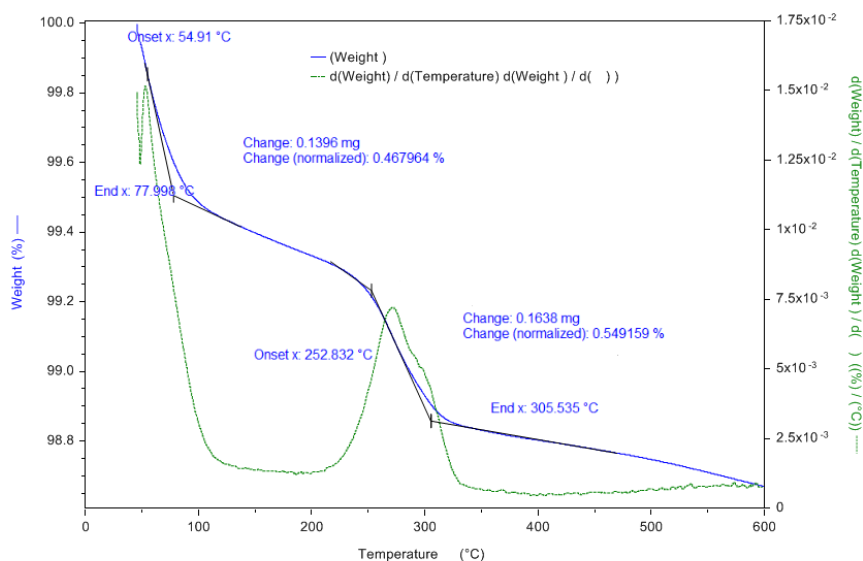


Figure 74: TGA analysis of Ntiles with mass changed denoted on blue and the derivative shown in green.

There are two main mass changed in the TGA of the ntiles, the first is around 100 $^\circ\text{C}$ which can be attributed to water loss in the sample. The second main mass loss occurs slightly below the 300 $^\circ\text{C}$ and can be attributed to hydroxyl groups leaving the surface. This result is an indicator of surface hydroxyls on the ntiles.

5.3.6 ^1H MAS NMR Results

Cursory results of ^1H NMR at lower spinning speeds $\sim 10\text{kHz}$ of the ntile show two main features, a peak at 4.8 ppm which can be attributed to bulk water on the material, and an additional side peak at 0.9 ppm which can be attributed to surface hydroxyl groups as shown in Figure 75.

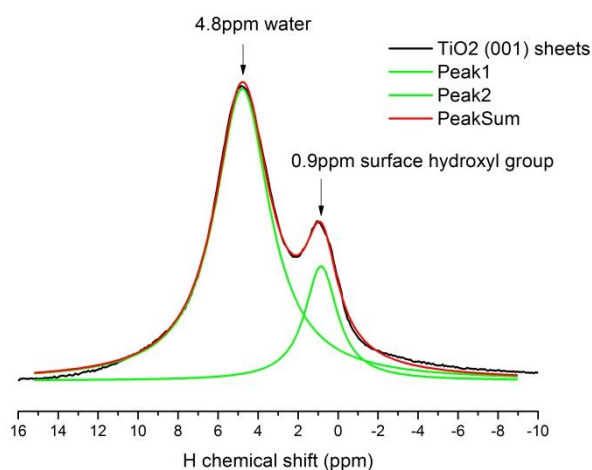


Figure 75: ^1H MAS NMR at low spinning speeds of ntile sample

Generally speaking, the more negative the chemical shift of a material the higher electron density of the particular atom being studied. For the ntiles the side peak that occurs 3.9 ppm lower than bulk water is indicative of hydroxyl groups which are often referred to as basic protons. The types of basic protons on the surface and be further elucidated by loading ntile sample into a smaller spinner to allow for higher spinning speeds and allowing for longer data acquisition time. The resulted of the longer acquisition time are shown in Figure 76.

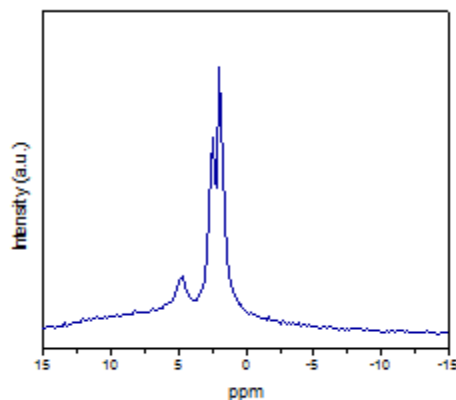


Figure 76: ^1H NMR with longer acquisition time

The left peak can be attributed to water and the right peak contains two type of basic protons, further confirming the presence of hydroxyl groups on the surface.

5.3.7 ^{31}P MAS NMR Results

Magic Angle Spinning (MAS) NMR was performed on the powdered derivatized anatase and Ntile samples at a 9T superconducting magnet the results of which are shown in Figure 77 and ^{31}P spectra intensities have been normalized by mass. 85% H_3PO_4 aqueous solution is used as an external ^{31}P chemical shift reference.

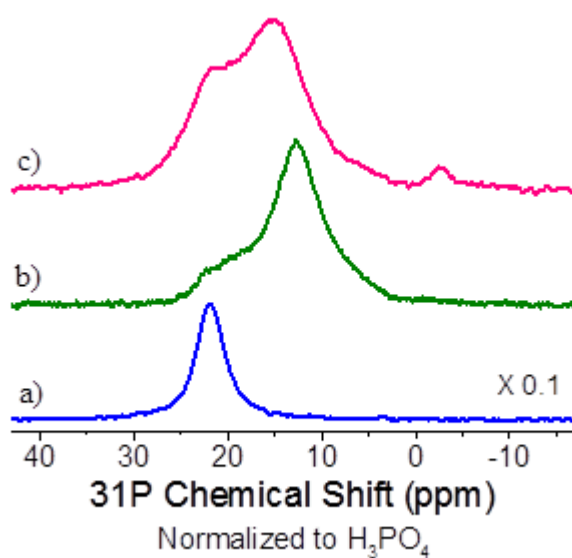


Figure 77: ^{31}P NMR of a) PPA crystal b) PPA derivatized Ntiles and c) PPA derivatized 32nm Anatase NPs

Three Lorentzian peaks are used to fit the raw signal as seen in Figure 78.

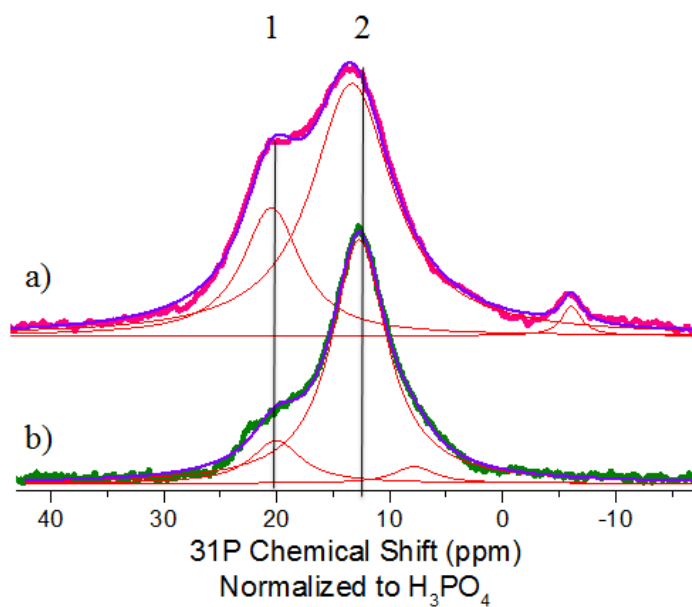


Figure 78: ^{31}P NMR of PPA derivatized a) 32nm Anatase and b) Ntiles with fitting shown in green

From the two main peaks it can be seen that there is an upfield chemical shift for the Ntiles as compared to the 32 nm anatase (Table 8), this is indicative of a higher electron density and hence a stronger bond between the phosphonate group and Ntile surface and the reason for the enhanced stability seen on the (001) surface of anatase.

Material	Peak 1 Center (ppm)	Peak 2 Center (ppm)
32nm Anatase	20.7	14.12
Ntile	20.7	12.69

Table 8: ^{31}P NMR Peak Fitting Results for PPA derivatized NP anatase and NTiles

Most likely the first peak can be attributed to physisorbed PPA since its chemical shift is the same as pure PPA powder and the second peak can be attributed to chemisorbed species. The areas of the two peaks can also be compared to determine the ratio of physisorbed to chemisorbed species for both samples. This ratio for 32 nm anatase is 0.36 and for Ntiles 0.16. It is most likely that there is an enhancement of chemisorbed species on the (001) surface as compared to the standard (101) surface.

5.4.8 Dye Binding Mechanism Results

In an effort to better understand the binding mechanism of the phosphonate group to the various surfaces and morphologies of titania Degussa P25, nanotubes, and nanotiles were derivatized with phenylphosphonic acid. ^{31}P MAS NMR was used to determine the change in supernatant concentration to evaluate surface coverage on p25, LTiNTs, and Ntiles. Using a specific surface areas (SSA) of $50 \text{ m}^2/\text{g}$ for p25, $156 \text{ m}^2/\text{g}$ for Ntiles, and $200 \text{ m}^2/\text{g}$ for the LTiNTs. These values of SSA were calculated from

SEM and TEM data for the Ntiles and previously published literature for the LTiNTs and p25. Using ^{31}P NMR the final concentration of the supernatant changed from the initial 0.1 M aqueous phenyl-phosphonic acid to 0.0895, 0.062, and 0.0916 for the p25, LTiNTs and Ntiles respectively. Using this and the SSA a simple calculation can be made to determine the average number of molecules/ surface area of the materials. Using p25 as the standard with 3.4×10^{18} molecules/ m^2 the LTiNTs have approximately 84% the number of molecules/ m^2 , and the Ntiles have approximately 24% the number of molecules/ m^2 . This trend is in agreement with the UV-Vis data.

5.5 Conclusions

When dealing with nanomaterials it is paramount that extensive consideration be dedicated to the surface of the material being dealt with. This dissertation should serve to further highlight the differences between the anatase (001) and (101) surface. I was able to demonstrate a novel synthesis of nanosized (001) surface enhanced nanotiles for use in DSSCs and ultimately DSPECs. The (001) nanotiles showed slower back electron transfer rates, and higher open circuit voltages than the standard (101) dominant nanomaterials. All of these properties are improvements on current DSSC anatase materials and published literature. The (001) surface is known to have lower dye uptake but even with the reduced amount of dye uptake IPCE values of 33% were attained. The considerations of phosphonated dye stability in aqueous conditions and under illumination were also evaluated and the (001) surface showed great improvement on both aqueous and photo stability of RuP as compared to standard anatase. Though the binding was found to most likely be bidentate for both surfaces there is a higher electron density observed when the phosphonate group binds to the (001) surface. This higher electronic density is indicative of stronger binding between the phosphonate and (001) surface. All of these conclusions put together show that the (001) surface is a topic of great research importance in the DSSC community and for any applications where surface molecular attachment is of importance. Additional work should be done to facilitate development of this surface for further study and implementation.

5.6 Future Work and Project Direction

With the studies presented here a multitude of potential future directions that this project can be taken have come to light. First there is still work that can be done using NMR to get a better understanding of the phosphonate dye binding to specific TiO_2 surfaces. Higher resolution scans, CP/MAS, and alternate pulse sequences can be used to remove the dipole-dipole interaction can further elucidate the binding on the (101) vs (001) surfaces of titania and improve understanding. Additionally, ^1H NMR can be done quantitatively to discern the exact amount of hydroxyl groups on the surface for comparison to under-coordinated titania sites to finish developing the dye coverage model.

It is very much worth pursuing the (001) surface of titania over the current (101) NP standard, however, there is still much work to be done so that they efficiencies of the (101) materials and surpass the current benchmarks. An understanding of the hydroxyl termination and the necessary heating required to remove said hydroxyl groups will allow for the potential for higher surface coverage and increase efficiency. This thesis has already demonstrated that there is an electrical advantage to using the (001) surface due to the enhancement of the Voc. The advantages shown by the retardation of the back electron transfer is also a compelling reason to continue study of the (001) surface.

The materials synthesis that I would propose would be to attempt to create a nanomaterial with higher percentage of (001) surface (ideally 100%) that is smaller <10 nm to improve the surface area to increase dye binding sites per overall area. This could potentially be done by modification of titanium precursor and synthesis conditions.

Additionally, the current material could be used if the removal of hydroxyl groups is achieved and dye loading improved.

CHAPTER 6 SCIENTIFIC OUTREACH AND CLEAN ENERGY LABS

It is common knowledge that there is a shortage of qualified people going into science, technology, engineering and math (STEM) disciplines in the United States. In an effort to combat this trend it is important to get students interested in science early to build their confidence to pursue STEM fields. Alternative energy research is a current topic owing to a necessity to move away from fossil fuels as a source of energy. The scientific background and fabrication of solar cells has been discussed extensively in this journal and other literature sources. Titanium dioxide is the most commonly used semiconductor for this purpose and many laboratory experiments have been developed using commercially available nanomaterials and pastes to incorporate into solar cells. I am unaware of any laboratory experiments that couple a basic hydrothermal synthesis of nanomaterials with solar cell construction. The level of this procedure is for advanced high school students and lower level college students.

6.1 Background information

The North Carolina School of Science and Math (NCSSM) is a magnet high school located in Durham which allows for an expanded curriculum in their trimester system. I created a trimester long laboratory from my research to be implemented for one their elective chemistry courses. The laboratory I created was to allow them to create their own dye sensitized solar cells from scratch. This allowed for the students to start

from the very beginning synthesizing their own nanomaterials, and using them to prepare a device that they could test with different dyes to evaluate the effectiveness of their device. The developed laboratory gives a structured backbone from them to work from and allows for individual inquiry on dye choice and independent research over the history of DSSCs and the materials that are currently being used and explored.

6.2 Lab Procedure and Development

The students will start out synthesizing nanomaterial TiO_2 hydrothermally, and after this synthesis they prepare the nanoparticles to be incorporated in a film. The film will be deposited on a transparent conducting substrate (FTO) and graphite will be used as a counter electrode. All materials and procedures are very similar to what the students would be using in an advanced laboratory and give them exposure for the types of work that someone who works developing DSSCs would partake in.

6.2.1 Nanomaterial Synthesis

Titanium Dioxide (titania) nanomaterials can be synthesized hydrothermally from a simple hydrolysis reaction between n-titanium butoxide (TiBuOx) and water. For this to be achieved 20 mL of chilled (allow TiBuOx to rest in a bucket of ice for 10-15 minutes prior to the synthesis and swirl bottle to ensure uniformity before measuring required amount) TiBuOx is added to a 60 mL teflon lined autoclave pressure vessel under stirring with a magnetic stir bar. Immediately after adding the TiBuOx add 2.1 mL of deionized water is added slowly drop-wise to the TiBuOx and allowed to stir covered for 30 minutes to produce a gel like substance as seen in Figure 79. The vessel is then sealed and allowed to cook in an oven for 24 hours at $180\text{ }^{\circ}\text{C}$ - $200\text{ }^{\circ}\text{C}$. After 24 hours the

mixture is allowed to cool to room temperature before proceeding with the washing procedure.

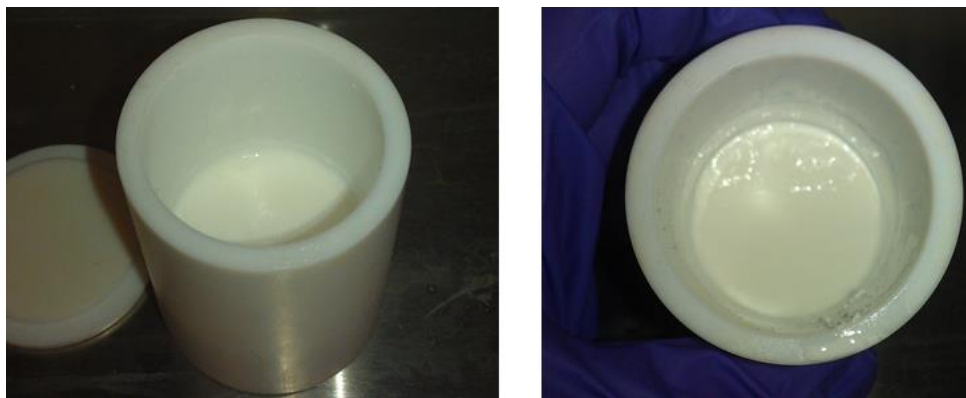


Figure 79: TiO_2 gel before cooking (left) and particulate caked material with top solution after cooking (right)

Once the vessel and materials are fully cooled the container is opened and the top solution is poured off into a waste container as shown in Figure 79. Deionized water is then added to the remaining white cake material in the teflon sleeve and stirred to begin the washing procedure. If the material has a grey or black hue/color to it that means that not enough water (oxygen) was available to get the 1:2 Ti:O ratio to synthesize titania. This is most likely due to incomplete sealing of the chamber which allowed for water to evaporate during the synthesis. A new synthesis should be started with an additional 0.5mL of water added to the previous specified amount. Once a white material is synthesized the mixture is then evenly distributed between 4-6 15 mL centrifuge tubes with the remaining volume of the tubes being filled with fresh deionized water. The tubes are centrifuged until the material forms a pellet at the bottom. The supernatant is poured off the top of the waste container and fresh deionized water is added to the tubes. After the fresh water is added the tubes need to be shaken vigorously to break up the

titania pellet at the bottom. This process is repeated 4 to 6 times until the top solution is clear and free of any residual organic material. Next replace the top solution with Ethanol, shake vigorously and centrifuge again. The ethanol wash will alter the color of the material and top solution to yellow. Next replace the top solution with water and repeat the process until the top solution becomes clear and the material is pale yellow or white. After a final wash the top solution can be poured off leaving a thick paste of titania pellet at the bottom as in Figure 80. A pipette should be used to remove any excess water.



Figure 80: TiO_2 pellet with top solution removed

The resulting material from this synthesis is nanostructured anatase TiO_2 as shown in the SEM image of Figure 81.

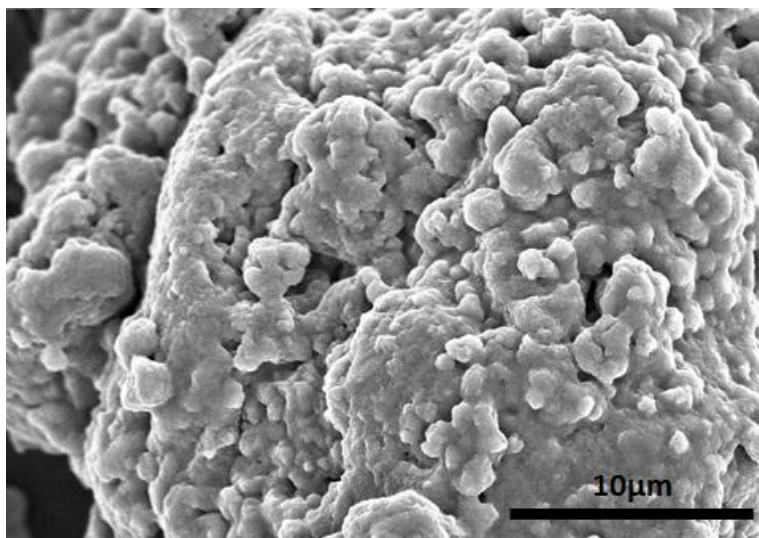


Figure 81: SEM of nanomaterial students will be producing for solar cell films

6.2.2 Paste and Film Preparation

For preparation of the paste that will allow for the titania nanomaterial to be incorporated into a film 400-600 mg of the wet nanomaterial pellet can be added to a fresh centrifuge tube. Once the material is measured out 0.25 mL of 10% vol aqueous acetyl acetone or 0.1M nitric acid is added in 4 separate increments with stirring in between to create a suspension of the nanomaterials. If the nanomaterials are not retaining a stable suspension there are two things that can be done. The first is sonicate the titania and acetyl acetone mix to break up any aggregates and facilitate suspension formation or if there is not access to a sonicator the nanomaterials can first be ground with a small mortar and pestle with 0.9mL of water once a smooth paste is formed it can be transferred back into the centrifuge tube and 0.1mL of undiluted acetyl acetone can be added. Once a stable suspension is created 0.3mL of 4 % aqueous solution of hydroxypropyl cellulose (MW 100,000) is added to the suspension and shaken vigorously to promote film porosity and adhesion. Lastly, 0.3mL of 10% aqueous solution of Triton-X100 is added to allow for smooth application. The paste (Figure 82) should be allowed to equilibrate for 30 minutes before being deposited into a film, and is stable for at least several weeks presuming that it is not allowed to dry out.



Figure 82: TiO₂ uniform liquid paste suspension

Transparent conducting glass, fluorine doped tin oxide (FTO) is used as the substrate after being cut to 2 cm x 4 cm slides. A multimeter is used to determine the conducting side and the glass is cleaned with acetone and a lint free wipe. Scotch tape is used to mask off a square area of 0.5 cm² towards one end of the glass as shown in Figure 83.

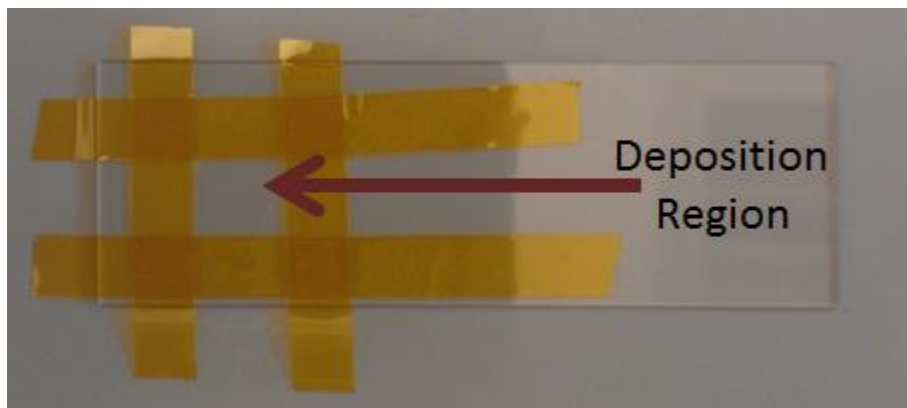


Figure 83: Slide with Kapton® Polyimide tape mask and deposition region labeled

A drop of the film paste is added to the center of the square and a razorblade or teflon stirring rod is used to evenly distribute the drop across the area shown in Figure 83. After depositing the film allow it to dry completely and then remove the scotch tape. The appearance of the film will range from pale yellow to white depending on the batch of paste used to create the film. As previously mentioned the yellow color is due to the ethanol washes and will be burned off in the annealing. The film can now be annealed for 60 minutes at 450 °C to remove all organic material and prepare for dye loading and assembly. Allow the film to completely cool to room temperature before sensitizing with dye. The completely annealed film will be white and relatively stable on the glass surface as shown in Figure 84.

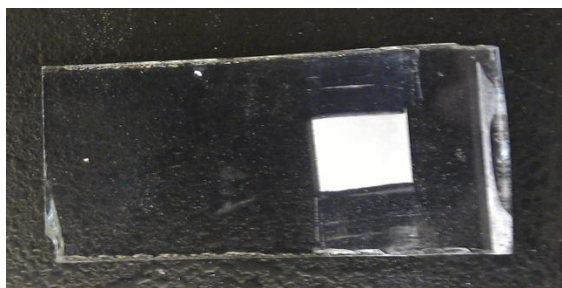


Figure 84: Annealed TiO_2 film ready for dye uptake

The most common roadblock in film preparation results in an unstable film. Once the film is dry it should adhere to the glass substrate a scratch test can be performed on the edge of the film to verify that chunks of the film do not flake off easily. The reason the film would not be stable on the surface is due to the film being too dense since TiO_2 adheres to itself more strongly than glass. To fix this issue add 0.3mL more of the 4 % aqueous solution of hydroxypropyl cellulose until a stable film forms.

6.2.3 Dye Choice and Preparation

This portion of the laboratory is designed for the students to do their own independent research to determine what materials are suitable for use as dyes in solar cells. Depending on the motivation of the course that is involved with this there are a number of dyes that are commercially available for purchase if one wishes to pursue a direction other than organic dyes. Examples of organic dyes that can be used for this purpose are berries such as blackberries or raspberries, teas, and leaves and grass. The students should be encouraged to try a variety of dyes to determine which one works the best and yields the highest potential.

To prepare the dye solution, grind the organic material of choice into a glass petri dish to extract all of the fluid from the material. For this fresh or frozen organic materials can be used. After this is done remove and large solid matter and the rest of the particulates and seeds can be removed by pouring through a strainer or filter paper. Deionized water can be added to the juice to increase the volume and aid in particulate removal. Once the solution is filtered it should be added to the bottom of a clean petri dish with enough solution to just cover the bottom. The slide with the annealed titania film can be placed face down in the dye solution and left to soak for at least 30 minutes as shown in Figure 85. Gently rinse the film with ethanol to remove any excess unbound dye and allow the slide to dry completely before device assembly.

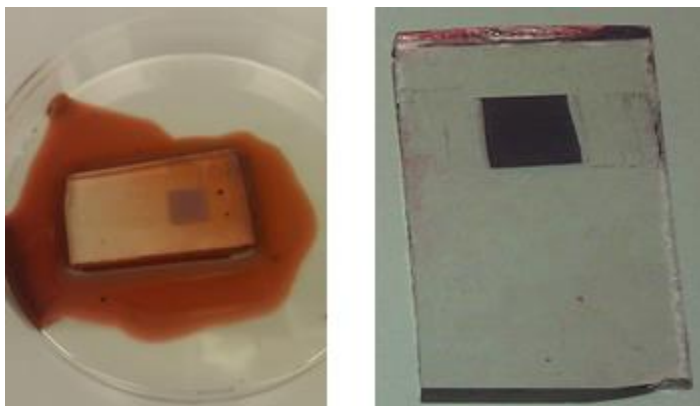


Figure 85: Dye sensitization of TiO_2 film, electrode soaking face down in blackberry juice (left) and final film post dye loading and ethanol wash

6.2.4 Device Assembly

To create the counter electrode gently coat the conducting side of a fresh piece of FTO with graphite in a size and shape to match the dye derivatized TiO_2 film as shown in Figure 86.

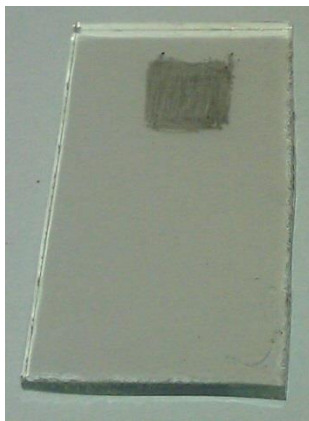


Figure 86: FTO with graphite counter electrode sketched on top (grey box)

On the derivatized slide create a wall around the film using 1-2 layers of parafilm, making sure to make good contact with the glass. A drop of electrolyte (0.5M Potassium Iodide with 0.05M Iodine in acetonitrile or ethylene glycol) is added to the top of the film with enough to cover film but not overflow the parafilm wall as can be seen in Figure 87.

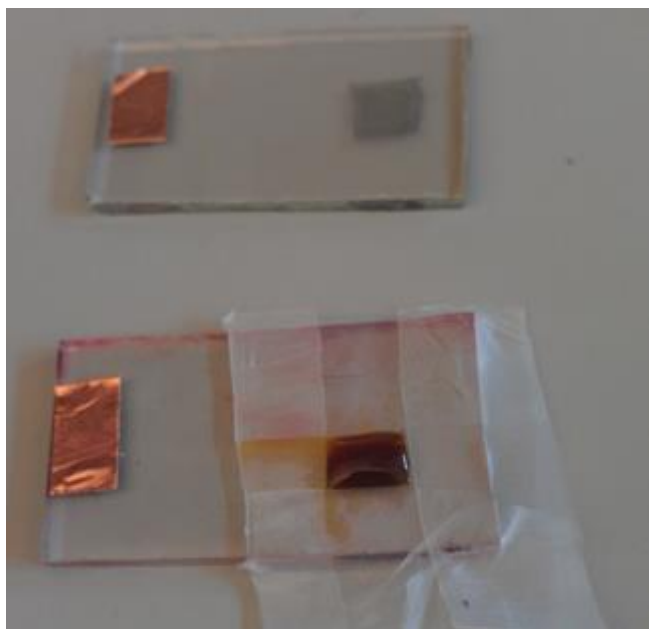


Figure 87: Counter electrode (top) and Electrode with parafilm and drop of electrolyte (bottom)

Slowly place the graphite side of the additional slide perpendicularly on top of the film slide and secure with binder clips as shown in Figure 88.

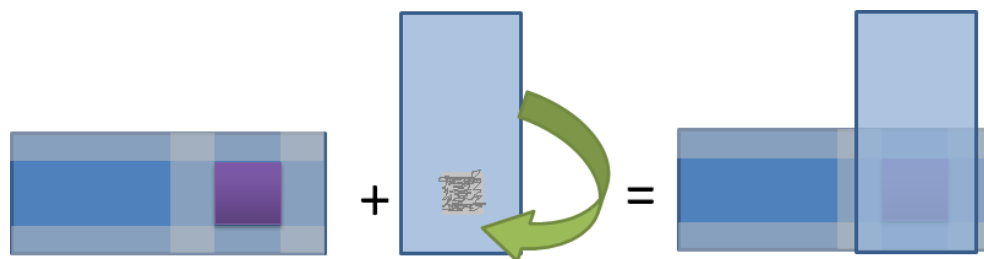


Figure 88: DSSC device assembly with derivatized TiO_2 film isolated by parafilm (left) and graphite coated counter electrode (center) and a completed cell after electrolyte is introduced (right)

6.2.5 Testing and Results

Depending on whether testing is to be done indoors or outside an appropriate electrolyte should be used. For testing that is just going to be done indoors water-free ethylene glycol may be used as the solvent however it is unstable under UV exposure so for devices that will be tested outside water-free acetonitrile should be used. To test a device indoors a bright light source such as an overhead projector should be shined on the device and the two electrodes can be attached to a multimeter to read the potential build up as shown in Figure 89. Care should be taken as to not leave the device under the light source for extended periods of time as this will cause heat build-up that will degrade the device performance. For measurements done outside it is best to perform them at the point in the day in which the sun is brightest on a day where there is a clear sky to get the highest potential results.

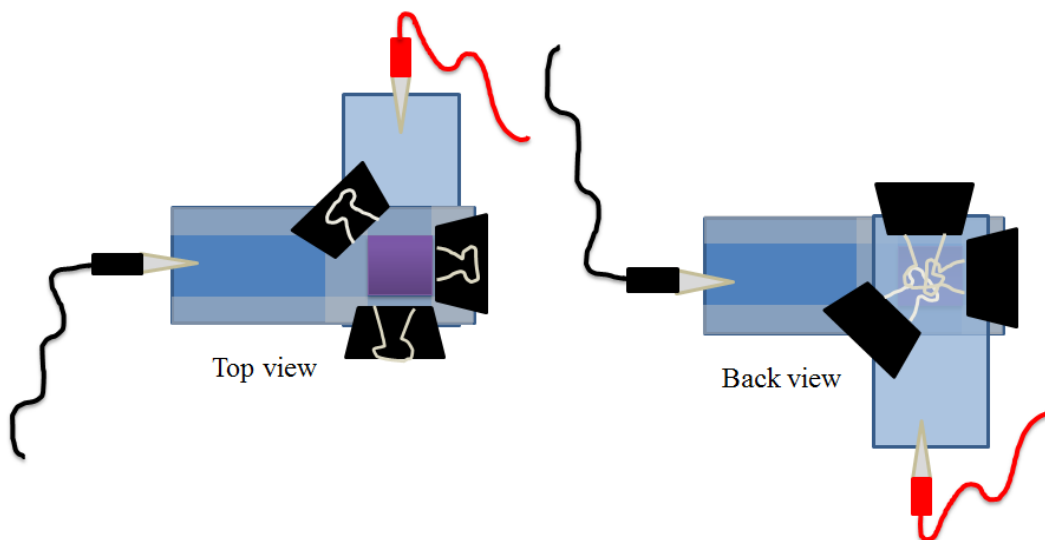


Figure 89: DSSC Device testing design

Preliminary results of this solar cell using the ethylene glycol based I/I- electrolyte with blackberry dye resulted in photovoltages above 0.4V from indoor light source directed at the cell. Without intention overhead lighting and window light produce a photovoltage of 0.1V. The device measured is shown in Figure 90.

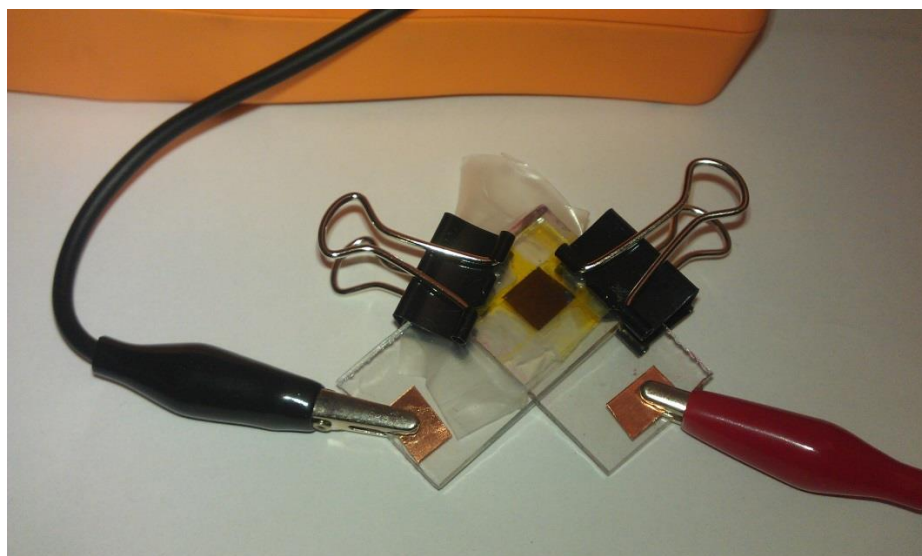


Figure 90: Blackberry derivatized device

6.2.6 Cautions and Hazards

For the synthesis of the materials standard personal protective equipment should be used consisting of gloves, safety glasses and a laboratory coat. It is necessary and highly recommended to have access to a hood to prepare the synthesis of the nanomaterials and for film deposition. Special care should be taken to not inhale any dried titania nanomaterials as there is no conclusive evidence of their safety at this moment and there is a large body of literature references on alternate nanomaterials being toxic or even carcinogens. This was taken into consideration when developing this lab and the entirety of this procedure has been developed so that the nanomaterials are never dried to be handled as a powder. This prevents most inhalation risk associated with nanomaterials as generally speaking there is a much reduced risk of aerosolizing once the nanomaterials are incorporated into a film. Additionally, N-Titanium butoxide and acetonitrile are flammable and toxic, gloves and safety goggles should be used when handling in a well-ventilated area.

REFERENCES:

- (1) Anthony, J. W.; Bideaux, R. A.; Bladh, K. W.; Nichols, M. C.; America, M. S. o., Ed.; Mineral Data Publishing: Chantilly, VA, 1997; Vol. III.
- (2) Weatherspoon, M. R.; Cai, Y.; Crne, M.; Srinivasarao, M.; Sandhage, K. H. *Angewandte Chemie International Edition* **2008**, *47*, 7921.
- (3) Landmann, M.; Rauls, E.; Schmidt, W. G. *Journal of Physics: Condensed Matter* **2012**, *24*, 195503.
- (4) Park, N. G.; van de Lagemaat, J.; Frank, A. J. *The Journal of Physical Chemistry B* **2000**, *104*, 8989.
- (5) Anderson, M. A.; Gieselmann, M. J.; Xu, Q. *Journal of Membrane Science* **1988**, *39*, 243.
- (6) Zaban, A.; Aruna, S. T.; Tirosh, S.; Gregg, B. A.; Mastai, Y. *The Journal of Physical Chemistry B* **2000**, *104*, 4130.
- (7) Zhang, Z.; Wang, C.-C.; Zakaria, R.; Ying, J. Y. *The Journal of Physical Chemistry B* **1998**, *102*, 10871.
- (8) Mo, C.-m.; Zhang, L.; Wang, G. *Nanostructured Materials* **1995**, *6*, 823.
- (9) Penn, R. L.; Banfield, J. F. *Geochimica et Cosmochimica Acta* **1999**, *63*, 1549.
- (10) Ushiroda, S.; Ruzyski, N.; Lu, Y.; Spitler, M. T.; Parkinson, B. A. *Journal of the American Chemical Society* **2005**, *127*, 5158.
- (11) Vittadini, A.; Casarin, M.; Selloni, A. *Theoretical Chemistry Accounts: Theory, Computation, and Modeling (Theoretica Chimica Acta)* **2007**, *117*, 663.
- (12) Lewis, G. N. *Valance and the Structure of Atoms and Molecules*, 1923.
- (13) Hadjiivanov, K. I.; Klissurski, D. G. *Chemical Society Reviews* **1996**, *25*, 61.
- (14) Vittadini, A.; Selloni, A.; Rotzinger, F. P.; Gratzel, M. *Physical Review Letters* **1998**, *81*, 2954.
- (15) Chen, Q.; Mogilevsky, G.; Wagner, G. W.; Forstater, J.; Kleinhammes, A.; Wu, Y. *Chemical Physics Letters* **2009**, *482*, 134.
- (16) Wen, C. Z.; Jiang, H. B.; Qiao, S. Z.; Yang, H. G.; Lu, G. Q. *Journal of Materials Chemistry* **2011**, *21*, 7052.

- (17) Wen, C. Z.; Zhou, J. Z.; Jiang, H. B.; Hu, Q. H.; Qiao, S. Z.; Yang, H. G. *Chemical Communications* **2011**, 47, 4400.
- (18) Yang, H. G.; Liu, G.; Qiao, S. Z.; Sun, C. H.; Jin, Y. G.; Smith, S. C.; Zou, J.; Cheng, H. M.; Lu, G. Q. *Journal of the American Chemical Society* **2009**, 131, 4078.
- (19) Yang, X. H.; Li, Z.; Liu, G.; Xing, J.; Sun, C.; Yang, H. G.; Li, C. *CrystEngComm* **2011**, 13, 1378.
- (20) Jellison, G. E.; Boatner, L. A.; Budai, J. D.; Jeong, B. S.; Norton, D. P. *Journal of Applied Physics* **2003**, 93, 9537.
- (21) Chambers, S. A.; Thevuthasan, S.; Farrow, R. F. C.; Marks, R. F.; Thiele, J. U.; Folks, L.; Samant, M. G.; Kellock, A. J.; Ruzycki, N.; Ederer, D. L.; Diebold, U. *Applied Physics Letters* **2001**, 79, 3467.
- (22) Yang, H. G.; Sun, C. H.; Qiao, S. Z.; Zou, J.; Liu, G.; Smith, S. C.; Cheng, H. M.; Lu, G. Q. *Nature* **2008**, 453, 638.
- (23) Wu, X.; Chen, Z.; Lu, G. Q.; Wang, L. *Advanced Functional Materials* **2011**, 21, 4167.
- (24) Fang, W. Q.; Gong, X.-Q.; Yang, H. G. *The Journal of Physical Chemistry Letters* **2011**, 2, 725.
- (25) Xiang, G.; Li, T.; Wang, X. *Inorganic Chemistry* **2011**, 50, 6237.
- (26) Liu, S.; Yu, J.; Jaroniec, M. *Chemistry of Materials* **2011**, 23, 4085.
- (27) Han, X.; Kuang, Q.; Jin, M.; Xie, Z.; Zheng, L. *Journal of the American Chemical Society* **2009**, 131, 3152.
- (28) Hall, D. O.; Rao, K. K. *Photosynthesis*; University Press, 1999.
- (29) Fujishima, A.; Honda, K. *Nature* **1972**, 238, 37.
- (30) O'Regan, B.; Gratzel, M. *Nature* **1991**, 353, 737.
- (31) Jakubikova, E.; Snoberger Iii, R. C.; Batista, V. S.; Martin, R. L.; Batista, E. R. *The Journal of Physical Chemistry A* **2009**, 113, 12532.
- (32) Guerrero, G.; Mutin, P. H.; Vioux, A. *Chemistry of Materials* **2001**, 13, 4367.
- (33) Chen, Z.; Concepcion, J. J.; Jurss, J. W.; Meyer, T. J. *Journal of the American Chemical Society* **2009**, 131, 15580.

- (34) Bae, E.; Choi, W. *The Journal of Physical Chemistry B* **2006**, *110*, 14792.
- (35) Hanson, K.; Brennaman, M. K.; Luo, H.; Glasson, C. R. K.; Concepcion, J. J.; Song, W.; Meyer, T. J. *ACS Applied Materials & Interfaces* **2012**, *4*, 1462.
- (36) Ohtani, B.; Prieto-Mahaney, O. O.; Li, D.; Abe, R. *Journal of Photochemistry and Photobiology A: Chemistry* **2010**, *216*, 179.
- (37) Kasuga, T.; Hiramatsu, M.; Hoson, A.; Sekino, T.; Niihara, K. *Advanced Materials* **1999**, *11*, 1307.
- (38) Mogilevsky, G.; Chen, Q.; Kulkarni, H.; Kleinhammes, A.; Mullins, W. M.; Wu, Y. *Journal of Physical Chemistry C* **2008**, *112*, 3239
- (39) Wagner, G. W.; Chen, Q.; Wu, Y. *Journal of Physical Chemistry C* **2008**, *112*, 11901.
- (40) Vandenabeele, P. *Practical Raman Spectroscopy: An Introduction*, 2013.
- (41) Bersani, D.; Lottici, P. P.; Ding, X.-z. *Applied Physics Letters* **1998**, *72*, 73.
- (42) Ohsaka, T.; Izumi, F.; Fujiki, Y. *Journal of Raman Spectroscopy* **1978**, *7*, 321.
- (43) Wang, Q.; Chen, C.; Zhao, D.; Ma, W.; Zhao, J. *Langmuir* **2008**, *24*, 7338.
- (44) Lv, K.; Cheng, B.; Yu, J.; Liu, G. *Physical Chemistry Chemical Physics* **2012**, *14*, 5349.
- (45) Lv, K.; Xiang, Q.; Yu, J. *Applied Catalysis B: Environmental* **2011**, *104*, 275.
- (46) Lazzeri, M.; Vittadini, A.; Selloni, A. *Physical Review B* **2001**, *63*.
- (47) Asahi, R.; Morikawa, T.; Ohwaki, T.; Aoki, K.; Taga, Y. *Science* **2001**, *293*, 269.
- (48) Wu, P. G.; Ma, C. H.; Shang, J. K. *Appl. Phys. A* **2005**, *81*, 1411.
- (49) Rothenberger, G.; Fitzmaurice, D.; Graetzel, M. *The Journal of Physical Chemistry* **1992**, *96*, 5983.
- (50) Redmond, G.; Fitzmaurice, D. *The Journal of Physical Chemistry* **1993**, *97*, 1426.
- (51) O'Regan, B.; Grätzel, M.; Fitzmaurice, D. *Chemical Physics Letters* **1991**, *183*, 89.

- (52) O'Regan, B.; Graetzel, M.; Fitzmaurice, D. *The Journal of Physical Chemistry* **1991**, *95*, 10525.
- (53) Flood, R.; Enright, B.; Allen, M.; Barry, S.; Dalton, A.; Doyle, H.; Tynan, D.; Fitzmaurice, D. *Solar Energy Materials and Solar Cells* **1995**, *39*, 83.
- (54) Greiner; Neise; Stoker *Thermodynamics and Statistical Mechanics*, 2004.
- (55) Asahi, R.; Taga, Y.; Mannstadt, W.; Freeman, A. J. *Physical Review B* **2000**, *61*, 7459.
- (56) Skoog, D. A.; West, D. M.; Holler, F. J. *Analytical Chemistry: An Introduction (Saunders Golden Sunburst Series)*; 7th ed., 1990.
- (57) *Practical Pharmaceutical Chemistry*; 4th ed., 1988.
- (58) Skoog, D. A.; West, D. M.; Holler, F. J.; Crouch, S. R. *Fundamentals of Analytical Chemistry*; 8th ed., 2003.
- (59) Martsinovich, N.; Troisi, A. *Physical Chemistry Chemical Physics* **2012**, *14*, 13392.
- (60) Krishnan, R. In *Encyclopedia of Electrochemistry*; Wiley-VCH Verlag GmbH & Co. KGaA: 2007.
- (61) Wang, H.; He, J.; Boschloo, G.; Lindström, H.; Hagfeldt, A.; Lindquist, S.-E. *The Journal of Physical Chemistry B* **2001**, *105*, 2529.
- (62) Chen, W.; Liu, Y.; Luo, J.; Sun, J.; Gao, L. *Materials Letters* **2012**, *67*, 60.
- (63) Willis, R. L.; Olson, C.; O'Regan, B.; Lutz, T.; Nelson, J.; Durrant, J. R. *The Journal of Physical Chemistry B* **2002**, *106*, 7605.
- (64) Koops, S. E.; O'Regan, B. C.; Barnes, P. R. F.; Durrant, J. R. *Journal of the American Chemical Society* **2009**, *131*, 4808.
- (65) Haque, S. A.; Tachibana, Y.; Willis, R. L.; Moser, J. E.; Gratzel, M.; Klug, D. R.; Durrant, J. R. *The Journal of Physical Chemistry B* **1999**, *104*, 538.
- (66) Bergeron, B. V.; Kelly, C. A.; Meyer, G. J. *Langmuir* **2003**, *19*, 8389.
- (67) Gillaizeau-Gauthier, I.; Odobel, F.; Alebbi, M.; Argazzi, R.; Costa, E.; Bignozzi, C. A.; Qu, P.; Meyer, G. J. *Inorganic Chemistry* **2001**, *40*, 6073.

- (68) Brennaman, M. K.; Patrocinio, A. O. T.; Song, W.; Jurss, J. W.; Concepcion, J. J.; Hoertz, P. G.; Traub, M. C.; Murakami Iha, N. Y.; Meyer, T. J. *ChemSusChem* **2011**, *4*, 216.
- (69) Song, W.; Glasson, C. R. K.; Luo, H.; Hanson, K.; Brennaman, M. K.; Concepcion, J. J.; Meyer, T. J. *The Journal of Physical Chemistry Letters* **2011**, *2*, 1808.
- (70) Nazeeruddin, M. K.; Kay, A.; Rodicio, I.; Humphrybaker, R.; Muller, E.; Liska, P.; Vlachopoulos, N.; Gratzel, M. *Journal of the American Chemical Society* **1993**, *115*, 6382.
- (71) Laskova, B.; Zukalova, M.; Kavan, L.; Chou, A.; Liska, P.; Wei, Z.; Bin, L.; Kubat, P.; Ghadiri, E.; Moser, J.; Grätzel, M. *Journal of Solid State Electrochemistry* **2012**, *16*, 2993.
- (72) Ito, S.; Murakami, T. N.; Comte, P.; Liska, P.; Grätzel, C.; Nazeeruddin, M. K.; Grätzel, M. *Thin Solid Films* **2008**, *516*, 4613.
- (73) Wang, Q.; Moser, J.-E.; Grätzel, M. *The Journal of Physical Chemistry B* **2005**, *109*, 14945.
- (74) Cheng, J.; Sprik, M. *Journal of Chemical Theory and Computation* **2010**, *6*, 880.
- (75) Trammell, S. A.; Moss, J. A.; Yang, J. C.; Nakhle, B. M.; Slate, C. A.; Odobel, F.; Sykora, M.; Erickson, B. W.; Meyer, T. J. *Inorganic Chemistry* **1999**, *38*, 3665.
- (76) Song, W.; Brennaman, M. K.; Concepcion, J. J.; Jurss, J. W.; Hoertz, P. G.; Luo, H.; Chen, C.; Hanson, K.; Meyer, T. J. *The Journal of Physical Chemistry C* **2011**, *115*, 7081.
- (77) Yang, W.; Li, J.; Wang, Y.; Zhu, F.; Shi, W.; Wan, F.; Xu, D. *Chemical Communications* **2011**, *47*, 1809.
- (78) Sauvage, F.; Decoppet, J.-D.; Zhang, M.; Zakeeruddin, S. M.; Comte, P.; Nazeeruddin, M.; Wang, P.; Grätzel, M. *Journal of the American Chemical Society* **2011**, *133*, 9304.
- (79) Harrick, N. J. *Internal Reflection Spectroscopy*, 1967.
- (80) Hotchkiss, P. J.; Jones, S. C.; Paniagua, S. A.; Sharma, A.; Kippelen, B.; Armstrong, N. R.; Marder, S. R. *Accounts of Chemical Research* **2011**, *45*, 337.
- (81) Suwanchawalit, C.; Wongnawa, S. *J Nanopart Res* **2010**, *12*, 2895.
- (82) Luschtinetz, R.; Frenzel, J.; Milek, T.; Seifert, G. *The Journal of Physical Chemistry C* **2009**, *113*, 5730.

(83) Levitt, M. H.